

ABSTRACT

Title of Document: MODEL DEVELOPMENT AND
VALIDATION OF PALLADIUM-BASED
MEMBRANES FOR HYDROGEN
SEPARATION IN PEM FUEL CELL
SYSTEMS

Atul Bhargav, Doctor of Philosophy, 2010

Directed By: Dr. Gregory S. Jackson, Associate Professor,
Department of Mechanical Engineering

Selective Pd-based membranes can extract near pure H₂ from hydrocarbon reformat gases in liquid-fueled standalone proton exchange membrane fuel cell (PEMFC) systems. A steady state system-level model of such a PEMFC system is built to understand trade-offs among key system performance metrics. H₂ recovery fraction in the membrane purifier critically affects overall system efficiency and thermal management. Hence, the development of detailed, high-fidelity mathematical models for Pd-based H₂ membranes is critical for optimizing hydrocarbon-fueled PEMFC systems relying on such membrane purification. Although interactions between Pd with reformat gases have been explored experimentally and with density functional theory models in the literature, membrane purifier design is often carried out using high-level approximations in empirical fits to experimental data with inadequate range of applicability for optimizing for system performance. Therefore, to provide a

more comprehensive membrane reactor model that predicts membrane performance over a broader range of conditions, a microkinetic model that captures surface and bulk Pd-H₂ and Pd_{0.77}Ag_{0.23}-H₂ interactions is presented. A systematic procedure to estimate thermokinetic parameters is established such that model results compare favorably with experimental measurements of H solubility and fluxes as a function of H₂ partial pressures and temperature. The Pd-H₂ interaction model is combined with a porous media transport model in a 1-D through-the-membrane composite membrane model that is validated against experiments performed on a composite membrane. Thermokinetic parameters for CO and H₂O competitive adsorption on Pd surface are estimated by fitting experimental observations and thermodynamics from literature DFT studies, and this thermochemistry is added to the pure Pd-H₂ thermochemistry to assess the impact of CO and H₂O poisoning for reformat purification applications.

The 1-D composite membrane model is combined with a channel flow model to form a comprehensive 2-D “down-the-channel” model, which is validated through counter-current gas flow experiments on the same composite membrane. Simulations using the 2-D model show that for a tested composite membrane, the porous support resistance is often a rate-limiting process for H₂ transfer. However, with an improved substrate design and a thinner membrane, other processes, such as competitive surface adsorption, can have a more significant role in limiting hydrogen fluxes as characterized by the effective drop in H chemical potential related to the process. This 2-D model is useful for carrying out parametric studies, and is a basis for further research.

MODEL DEVELOPMENT AND VALIDATION OF PALLADIUM-BASED
MEMBRANES FOR HYDROGEN SEPARATION IN PEM FUEL CELL
SYSTEMS

By

Atul Bhargav

Dissertation submitted to the Faculty of the Graduate School of the
University of Maryland, College Park, in partial fulfillment
of the requirements for the degree of
Doctor of Philosophy
2010

Advisory Committee:

Professor Gregory S. Jackson, Chair

Professor Jungho Kim

Professor Michael R. Zachariah

Professor Bao Yang

Professor Srinivasa R. Raghavan, Dean's representative

© Copyright by
Atul Bhargav
2010

Dedication

To Amma & Anna, and to Chinnu.

Acknowledgements

First of all, I would like to acknowledge my advisor Dr. Gregory Jackson for his constant encouragement and support. He has been both a teacher and mentor for me. He has had patience when I failed, and good things to say when I succeeded.

I would also like to acknowledge my beloved family: mother Smt. Shantha Venkataraman, father Shri. H.S. Venkataraman and wife Smt. Udaya Shree Subalam for all their love, support and sacrifice. This research could not have been possible without their unwavering confidence in me.

I would like to thank former graduate students Eric Shields and Jenny Hu for their friendship and helpful discussions. Josh Pearlman deserves special credit for being a friend throughout. I also thank Will Gibbons and Ian Young of UMD, and Chris Tesluk, Pat Hearn, Tom Willard and Joe Ufnal of Ballard Power Systems for all their help and technical information. Special thanks to Don Mase, Larry Long and Gardell Gefke of Vehicle Systems Inc., College Park for their guidance on building LabView code.

I would also like to acknowledge my close friends Asitav, Bhaskar, Vinod, Sumit, Isaac, Kanika, Ria and Vikram. Finally, I thank the government and the people of USA for extending such a great opportunity to me, and providing an excellent ambience to carry out research.

Table of Contents

| | |
|--|-----|
| Dedication | ii |
| Acknowledgements | iii |
| Table of Contents | iv |
| Nomenclature | vi |
| List of Figures | ix |
| Chapter 1: Significance of H ₂ purification in PEM fuel cell systems..... | 1 |
| 1.1 Introduction..... | 1 |
| 1.2 Impact of Pd Membranes on PEMFC System Performance..... | 4 |
| 1.2.1 System Description..... | 4 |
| 1.2.2 System Modeling Approach | 8 |
| 1.2.3 System Model results..... | 14 |
| 1.3 Additional considerations for H ₂ purifier design | 23 |
| 1.4 Summary | 26 |
| Chapter 2: Literature review of Pd-based membranes and objectives of current study | 28 |
| 2.1 Introduction..... | 28 |
| 2.1.1 Membrane purifier and membrane reactor | 28 |
| 2.2 Pd-H ₂ and Pd-alloy-H ₂ interactions | 30 |
| 2.3 Pd membrane supports..... | 33 |
| 2.4 Mathematical modeling of Pd membranes | 34 |
| 2.5 Summary and need for a new mathematical model | 38 |
| 2.6 Objectives of current study | 40 |
| Chapter 3: Modeling Pd-H ₂ and Pd _{0.77} Ag _{0.23} -Pd interactions | 42 |
| 3.1 Introduction..... | 42 |
| 3.2 Model description | 43 |
| 3.2.1 Surface processes..... | 45 |
| 3.2.2 Bulk diffusion | 49 |
| 3.3 Numerical Implementation | 50 |
| 3.4 Parameter estimation for pure Pd..... | 51 |
| 3.5 Parameter estimation for Pd _{0.77} Ag _{0.23} | 58 |
| 3.6 Model Results for H ₂ -Pd _{0.77} Ag _{0.23} | 65 |
| 3.7 Summary | 74 |
| Chapter 4: Pd-composite membranes | 76 |
| 4. 1 Introduction..... | 76 |
| 4.2 Porous media transport model | 79 |
| 4.2.1 Model equations..... | 79 |
| 4.2.2 Numerical implementation..... | 81 |
| 4.3 Experiment..... | 83 |
| 4.3.1 Bare substrate pressure drop..... | 83 |
| 4.3.2 Pd-ceramic composite membrane testing | 84 |
| 4.4 Model results and discussion | 90 |
| 4.5 Summary | 100 |

| | |
|--|-----|
| Chapter 5: Competitive adsorption on Pd surface | 102 |
| 5.1 Introduction..... | 102 |
| 5.2 Thermo-kinetics of Pd surface chemistry | 103 |
| 5.3 CO & CO ₂ poisoning on Pd surfaces..... | 106 |
| 5.4 H ₂ O poisoning on Pd surfaces | 110 |
| 5.5 Combined effect of CO and H ₂ O | 115 |
| 5.6 Summary | 117 |
| Chapter 6: Quasi 1-D “down-the-channel” membrane purifier model..... | 119 |
| 6.1 Introduction..... | 119 |
| 6.2 Conservation equations..... | 119 |
| 6.3 Numerical solution..... | 126 |
| 6.4 Experiment..... | 130 |
| 6.5 Results and discussion | 133 |
| 6.5.1 H ₂ + N ₂ / Ar gas tests..... | 133 |
| 6.5.2 CO poisoning studies | 139 |
| 6.5.3 H ₂ O poisoning studies..... | 141 |
| 6.6 Summary | 144 |
| Chapter 7: Conclusions | 145 |
| 7.1 Research Summary | 145 |
| 7.2 Contributions to the literature | 146 |
| 7.3 Recommendations for Future Research | 147 |
| Bibliography | 149 |

Nomenclature

| <i>Symbol</i> | <i>Description</i> | <i>Units</i> |
|------------------|--|---|
| A | pre-exponential for surface reaction rate constant | $\text{mol}\cdot\text{m}^{-2}$ |
| A_{flow} | channel flow area | m^2 |
| A_{int} | interfacial/ wetted area | m^2 |
| d_{hyd} | hydraulic diameter | m |
| $D_{H,\infty}$ | pre-exponential for D_H | $\text{m}^2\cdot\text{s}^{-1}$ |
| D_H | bulk-phase diffusion coefficient | $\text{m}^2\cdot\text{s}^{-1}$ |
| D_{kl} | gas-phase binary diffusion coefficients | $\text{m}^2\cdot\text{s}^{-1}$ |
| $D_{mix,k}$ | gas-phase mix diffusion coefficient of component k | $\text{m}^2\cdot\text{s}^{-1}$ |
| D_{kl}^e | effective molecular diffusion coefficients | $\text{m}^2\cdot\text{s}^{-1}$ |
| $D_{k,Kn}^e$ | effective Knudsen diffusion coefficients | $\text{m}^2\cdot\text{s}^{-1}$ |
| E_a | activation energy for surface reaction rates | $\text{J}\cdot\text{mol}^{-1}$ |
| E_{diff} | activation energy for atomic diffusion in bulk Pd | $\text{J}\cdot\text{mol}^{-1}$ |
| g_I | Gibbs interaction potential between dissolved H atoms | $\text{J}\cdot\text{mol}^{-1}$ |
| ΔH_{ads} | enthalpy of adsorption | $\text{J}\cdot\text{mol}^{-1}$ |
| ΔH_{sol} | enthalpy of solution | $\text{J}\cdot\text{mol}^{-1}$ |
| j_k | mass flux of species k through composite membrane | $\text{kg}\cdot\text{m}^{-2}\cdot\text{s}^{-1}$ |
| $J_{H,diff}$ | atomic Hydrogen flux | $\text{mol}\cdot\text{m}^{-2}\cdot\text{s}^{-1}$ |
| j_k | mass flux of species k through composite membrane | $\text{kg}\cdot\text{m}^{-2}\cdot\text{s}^{-1}$ |
| J_k | molar flux of species k through composite membrane | $\text{mol}\cdot\text{m}^{-2}\cdot\text{s}^{-1}$ |
| k_{ads} | rate constant for adsorption reaction | $\text{mol}\cdot\text{m}^{-2}\cdot\text{s}^{-1}$ |
| k_{des} | rate constant for desorption reaction | $\text{mol}\cdot\text{m}^{-2}\cdot\text{s}^{-1}$ |
| k_{bs}^0 | pre-exponential for bulk-surface transition rate calculation | $\text{mol}\cdot\text{m}^{-2}\cdot\text{s}^{-1}$ |
| k_{sb}^0 | pre-exponential for surface-bulk transition rate calculation | $\text{mol}\cdot\text{m}^{-2}\cdot\text{s}^{-1}$ |
| k_{surf} | rate constant for surface reaction | $\text{mol}\cdot\text{m}^{-2}\cdot\text{s}^{-1}$ |
| K_H | permeability of metal for Sievert's law | $\text{mol}\cdot\text{m}^{-1}\cdot\text{s}^{-1}\cdot\text{Pa}^{-0.5}$ |
| \dot{m} | mass flow rate | kg s^{-1} |

| | | |
|-----------------------------|---|---|
| $[M]$ | mass matrix for DAE system | - |
| P | pressure | Pa |
| Pe | Peclet number | |
| r | radial co-ordinate in porous media | m |
| r_p | mean pore radius of porous media | m |
| R | universal gas constant | $\text{J}\cdot\text{mol}^{-1}\cdot\text{K}^{-1}$ |
| Re | Reynolds number | |
| s^0 | sticking probability | - |
| Sh | Sherwood number | |
| T | temperature | K |
| t | time | S |
| T_{ref} | reference temperature for thermodynamic data | K |
| v | mean gas velocity | m s^{-1} |
| W_k | molecular weight of species k | $\text{g}\cdot\text{mol}^{-1}$ |
| $X_{\text{H,bulk}}$ | mole fraction of interstitial sites occupied by H | - |
| X_k | gas-phase mole fraction of species k | - |
| $[X_k]$ | gas or surface concentration of species k | $\text{mol}\cdot\text{m}^{-2} / \text{mol}\cdot\text{m}^{-3}$ |
| Y_k | gas-phase mass fraction of species k | - |
| Δx | length of each segment along purifier | m |
| Δz | Pd-alloy membrane thickness | m |
| β | temperature exponent for surface reaction rate constant | - |
| $\Gamma_{\text{Pd,bulk}}$ | volumetric concentration of interstitial sites | $\text{mol}\cdot\text{m}^{-3}$ |
| $\Gamma_{\text{Pd,surf}}$ | surface site density of adsorption sites on Pd alloy | $\text{mol}\cdot\text{m}^{-2}$ |
| $\varepsilon_{\text{H-H}}$ | interaction potential between adsorbed H-atoms (surface) | |
| $\varepsilon_{\text{surf}}$ | surface roughness parameter | - |
| $\Delta\mu_{\text{sol}}^0$ | change in chemical potential for H dissolution | $\text{J}\cdot\text{mol}^{-1}$ |
| $\mu_{\text{H}}^{\text{E}}$ | excess free energy of H dissolution in Pd alloy | $\text{J}\cdot\text{mol}^{-1}$ |
| η | fraction of bulk interstitial sites favorable for H atom | - |
| ρ | gas-phase density | $\text{kg}\cdot\text{m}^{-3}$ |
| θ_k | surface coverage of species k | - |
| ν_{ki} | stoichiometric coefficient of k^{th} species in i^{th} reaction | - |
| φ_g | average porosity of porous media | - |
| τ_g | average tortuosity of porous media | - |

| | | |
|-------------------|---------------------|------|
| μ_g | gas-phase viscosity | Pa·s |
| δ_{ij} | Kronecker-delta | - |
| Subscripts | | |
| <i>ch</i> | channel | |
| <i>int</i> | interface | |
| <i>perm</i> | permeate | |
| <i>pm</i> | porous media | |
| <i>ref</i> | reference | |

List of Figures

| | |
|---|----|
| Figure 1.1: Schematic diagram showing realization of PEM fuel cell system integrated with liquid fueled ATR reactor, water–gas-shift/Pd-alloy-membrane reactor, and retentate exhaust burner for waste-heat recovery | 5 |
| Figure 1.2: Overall system efficiency and total water balance (in g s^{-1} accumulated) as functions of net electric power for the liquid-fueled PEM fuel cell system at baseline conditions (see Table 1.2) at three different ambient temperatures. Numbers on top of bars indicate T_{amb} | 17 |
| Figure 1.3: Parasitic loads for LP and HP compressors, cooling fans, and liquid pumps for the liquid-fueled PEM fuel cell system at baseline conditions (see Table 1.1) at three different ambient T_{amb} and \dot{W}_{net} | 19 |
| Figure 1.4: System efficiency η_{th} and total water balance as functions of H_2 recovery fraction of the purifier for full-load and half-load conditions: (a) $T_{\text{amb}} = 50^\circ\text{C}$ and (b) $T_{\text{amb}} = 30^\circ\text{C}$ | 21 |
| Figure 1.5: Critical system temperatures as functions of H_2 recovery fraction of the Pd alloy-membrane for $\dot{W}_{\text{net}} = 2.5 \text{ kW}$ at $T_{\text{amb}} = 30^\circ\text{C}$ | 23 |
| Figure 2.1: Schematic illustration of a membrane purifier operated in counterflow mode: reformate gases ($\text{H}_2 + \text{CO} + \text{CO}_2 + \text{H}_2\text{O} + \text{N}_2$) enter the shell side of the purifier from the left. H_2 depleted reformate gases (also called retentate) leave the purifier on the right. Sweep gases (typically H_2O and/ or N_2) enter the inner tube from the right side. The H_2 -rich stream exits on the left side and is fed into the PEMFC anode. | 29 |
| Figure 2.2: Steps involved in H_2 transport across a Pd-alloy membrane..... | 31 |
| Figure 2.3: Schematic illustration of the objective of building a Pd-membrane based purifier model in the context of a PEM fuel cell system | 41 |
| Figure 3.1: Energy levels associated with H in Pd | 44 |
| Figure 3.2: Equilibrium solubility profiles of H in Pd at various T (shown in $^\circ\text{C}$ next to each profile) | 54 |
| Figure 3.3: γ_{H} values at various temperatures (shown in $^\circ\text{C}$ next to each line) | 55 |
| Figure 3.4: Variation of Sievert’s permeability constant K_{H} with feed side H_2 pressure for Pd membranes at various temperatures. $\Delta z_{\text{memb}} = 60 \mu\text{m}$. $(PX_{\text{H}_2})_{\text{perm}} = 0.116 \text{ MPa}$. $(PX_{\text{H}_2})_{\text{feed}}$ is varied as shown..... | 57 |

| | |
|--|----|
| Figure 3.5: Comparison of model results with experiments by Gielens et al [110] on free standing membranes. $\Delta z_{\text{memb}} = 1 \mu\text{m}$ $(PX_{\text{H}_2})_{\text{feed}} = 20 \text{ kPa}$. $(PX_{\text{H}_2})_{\text{perm}} = 5 \text{ kPa}$ | 58 |
| Figure 3.6: Solubility of H in $\text{Pd}_{0.77}\text{Ag}_{0.23}$: model results match with experimental values from literature | 62 |
| Figure 3.7: High temperature H_2 permeance model predictions for thick $\text{Pd}_{0.77}\text{Ag}_{0.23}$ membranes compare well with experiments ([87]). | 64 |
| Figure 3.8: Comparison of model results with experimental data by Mejdell et al [45]. $T = 300 \text{ }^\circ\text{C}$. Feed side is pure H_2 at 120 kPa, and sweep side is pure H_2 at 100 kPa.. | 66 |
| Figure 3.9: H_2 flux through a $1 \mu\text{m}$ thick $\text{Pd}_{0.77}\text{Ag}_{0.23}$ membrane at $250 < T < 550 \text{ }^\circ\text{C}$, when the feed side is maintained at 120 kPa. | 68 |
| Figure 3.10: H_2 flux through a $5 \mu\text{m}$ thick $\text{Pd}_{0.77}\text{Ag}_{0.23}$ membrane at $250 < T < 550 \text{ }^\circ\text{C}$, when the feed side is maintained at 120 kPa | 69 |
| Figure 3.11: H_2 flux through a $10 \mu\text{m}$ thick $\text{Pd}_{0.77}\text{Ag}_{0.23}$ membrane at $250 < T < 550 \text{ }^\circ\text{C}$, when the feed side is maintained at 120 kPa | 70 |
| Figure 3.12: Model results: variation of linear-fit Sievert's law coefficient K_{H} with temperature and membrane thickness. Feed side is at 120 kPa, and sweep side is varied between 10 and 100 kPa (both sides are pure H_2). | 72 |
| Figure 3.13: Model results: sensitivity of H_2 flux at typical conditions to key parameters. | 73 |
| Figure 4.1: A typical cross-sectional electron-micrograph of the Pd-ceramic composite membrane. The porous macroporous & mesoporous layers can be distinguished from the brighter Pd metal..... | 85 |
| Figure 4.2: Experimental setup for pure H_2 composite membrane tests..... | 86 |
| Figure 4.3: Comparison of experimental data (symbols) with model results for Pd-ceramic composite membranes at $200 < T < 450 \text{ }^\circ\text{C}$ | 89 |
| Figure 4.4: Model predicted drops of H chemical potential due to the Pd surfaces, the Pd bulk and porous substrate; $\Delta z_{\text{memb}} = 6\mu\text{m}$, $110 \leq (PX_{\text{H}_2})_{\text{feed}} \leq 220 \text{ kPa}$, $(PX_{\text{H}_2})_{\text{perm}} = 110 \text{ kPa}$, $T = 200 \text{ }^\circ\text{C}$ | 93 |
| Figure 4.5: Model predicted drops of H chemical potential due to the Pd surfaces, the Pd bulk and porous substrate; $\Delta z_{\text{memb}} = 6\mu\text{m}$, $110 \leq (PX_{\text{H}_2})_{\text{feed}} \leq 220 \text{ kPa}$, $(PX_{\text{H}_2})_{\text{perm}} = 110 \text{ kPa}$, $T = 250 \text{ }^\circ\text{C}$ | 94 |
| Figure 4.6: Model predicted drops of H chemical potential due to the Pd surfaces, the Pd bulk and porous substrate; $\Delta z_{\text{memb}} = 6\mu\text{m}$, $110 \leq (PX_{\text{H}_2})_{\text{feed}} \leq 220 \text{ kPa}$, $(PX_{\text{H}_2})_{\text{perm}} = 110 \text{ kPa}$, $T = 350 \text{ }^\circ\text{C}$ | 95 |

| | |
|--|-----|
| Figure 4.7: Model predicted drops of H chemical potential due to the Pd surfaces, the Pd bulk and porous substrate; $\Delta z_{\text{memb}} = 6\mu\text{m}$, $110 \leq (PX_{\text{H}_2})_{\text{feed}} \leq 220$ kPa, $(PX_{\text{H}_2})_{\text{perm}} = 110$ kPa, $T = 450$ °C | 96 |
| Figure 4.8: Model predicted drops of H chemical potential due to the Pd surfaces, the Pd bulk and porous substrate; $\Delta z_{\text{memb}} = 3\mu\text{m}$, $110 \leq (PX_{\text{H}_2})_{\text{feed}} \leq 220$ kPa, $(PX_{\text{H}_2})_{\text{perm}} = 110$ kPa, $T = 200$ °C | 97 |
| Figure 4.9: Model predicted drops of H chemical potential due to the Pd surfaces, the Pd bulk and porous substrate; $\Delta z_{\text{memb}} = 3\mu\text{m}$, $110 \leq (PX_{\text{H}_2})_{\text{feed}} \leq 220$ kPa, $(PX_{\text{H}_2})_{\text{perm}} = 110$ kPa, $T = 450$ °C | 98 |
| Figure 4.10: Effect of surface availability $\varepsilon_{\text{surf,perm}}$ on performance of 1, 3 and 6 μm composite membranes at $T = 250$ °C, typical operating conditions..... | 100 |
| Figure 5.1: (a) Model results showing effect of CO on H ₂ flux through free standing 1 μm and 10 μm Pd membranes. $(PX_{\text{H}_2})_{\text{feed}} = 100$ kPa, $(PX_{\text{H}_2})_{\text{perm}} = 10$ kPa. Feed side is 95% H ₂ with balance N ₂ or CO. (b) surface coverages θ_{H} and θ_{CO} for a 1 μm thick membrane at same conditions as in (a). | 110 |
| Figure 5.2: Poisoning effect of steam. Red lines indicate model results, blue lines are from experiments by Gielens et al. $\Delta z_{\text{memb}} = 1$ μm ; $(PX_{\text{H}_2})_{\text{feed}} = 20$ kPa, $(PX_{\text{H}_2})_{\text{perm}} = 5$ kPa. Feed side is 20% H ₂ and 20% N ₂ or H ₂ O | 113 |
| Figure 5.3 (a) Effect of H ₂ O poisoning on H ₂ flux through 1 μm and 10 μm thick Pd membranes. Reformate side is 20% H ₂ / balance N ₂ for no H ₂ O cases and 20%H ₂ / 20%H ₂ O balance N ₂ for steam cases. (b) Surface coverages θ_{H} and $\theta_{\text{H}_2\text{O}}$ for the 1 μm thick membrane for the same conditions as in (a). | 115 |
| Figure 5.4: (a) Model results showing combined effect of CO + H ₂ O on H ₂ flux through Pd ceramic composite membranes. $\Delta z_{\text{memb}} = 6$ μm ; see Table 4.1 for ceramic substrate properties; $(PX_{\text{H}_2})_{\text{feed}} = 124$ kPa, $(PX_{\text{H}_2})_{\text{perm}} = 30.9$ kPa. Feed side is 35% H ₂ with balance N ₂ when no CO or H ₂ O is present. 35% H ₂ , 5% CO, 15% H ₂ O, balance N ₂ for appropriate case as indicated in figure. Also shown for comparison in red and green are H ₂ fluxes with only one poisoning species present (either 5% CO or 15% H ₂ O) ; (b) surface coverage for same conditions as in (a) when neither poisoning species are present and when both species are present | 117 |
| Figure 6.1: State space variables in each segment of the membrane purifier. Note that only exit mass flow rates are stored. *Interface variables are ‘algebraic’, and are handled separately, as discussed subsequently | 121 |
| Figure 6.2: Experimental test setup for counter-current gas flow experiments on composite membrane assembly | 131 |
| Figure 6.3: Effect of reformate H ₂ partial pressure on H ₂ recovery fraction. Reformate inlet conditions are $P = 379$ kPa, 2500 sccm 5 kWe/ 1400 sccm at 2.5 kWe, H ₂ as | |

shown/ N₂ balance. Sweep inlet conditions are $P = 137$ kPa, 400 sccm 5 kWe/ 200 sccm 2.5 kWe, H₂/ Ar = 25/75 mol% 135

Figure 6.4: H-chemical potential at various locations along the length of the composite membrane purifier. $T = 350$ °C; Reformate side: $P_{\text{reformatate}} = 379$ kPa, total inlet flow = 2500 sccm, inlet H₂/ N₂ = 34/ 66 mol%); Sweep side: $P_{\text{sweep}} = 137$ kPa, total inlet flow = 400 sccm, inlet H₂/ Ar = 25/ 75 mol% 136

Figure 6.5: Effect of sweep H₂ partial pressure on H₂ recovery fraction. Reformate inlet conditions are $P = 379$ kPa, 2500 sccm 5 kWe/ 1400 sccm at 2.5 kWe, H₂ / N₂ = 34/66. Sweep inlet conditions are $P = 137$ kPa, 400 sccm at 5 kWe/ 200 sccm at 2.5 kWe, H₂ as shown/ Ar balance 137

Figure 6.6: Effect of reformate H₂ partial pressure on H₂ recovery fraction. Reformate inlet conditions are $P = 379$ kPa, 2500 sccm at 5 kWe/ 1400 sccm at 2.5 kWe, H₂ as shown/ N₂ balance. Sweep inlet conditions are $P = 137$ kPa, 400 sccm 5 kWe/ 200 sccm 2.5 kWe, H₂/ Ar = 25/75 mol% 138

Figure 6.7: H-chemical potential at various locations along the length of the composite membrane purifier. $T = 250$ °C; Reformate side: $P_{\text{reformatate}} = 379$ kPa, total inlet flow = 2500 sccm, inlet H₂/ N₂ = 34/ 66 mol%; Sweep side: $P_{\text{sweep}} = 137$ kPa, total inlet flow = 400 sccm, inlet H₂/ Ar = 20/ 80 mol% 139

Figure 6.8: CO poisoning of Pd surfaces: comparison of 2-D model results with counter-current gas flow experiments on Pd composite membranes at various temperatures. Reformate conditions: $P_{\text{reformatate}} = 379$ kPa, total inlet flow 2500 sccm (34% H₂, CO as indicated, N₂ balance). Sweep side: $P_{\text{sweep}} = 137$ kPa, total inlet flow 400 sccm (25% H₂, balance Ar)..... 140

Figure 6.9: CO poisoning effect: Hydrogen chemical potential μ_{H} at various locations along the length of the purifier and through the composite membrane. Reformate conditions: $P_{\text{reformatate}} = 379$ kPa, total flow 2500 sccm (34% H₂, 8% CO, balance N₂). Sweep conditions: $P_{\text{sweep}} = 137$ kPa, total flow 400 sccm (25% H₂, balance Ar). ... 141

Figure 6.10: H₂O poisoning of Pd surfaces: comparison of 2-D model results with counter-current gas flow experiments on a Pd composite membrane at various temperatures. Reformate conditions: $P_{\text{reformatate}} = 379$ kPa, total inlet flow 2500 sccm (34% H₂, H₂O as indicated, N₂ balance). Sweep side: $P_{\text{sweep}} = 137$ kPa, total inlet flow 400 sccm (25% H₂, balance Ar)..... 143

Figure 6.11: H₂O poisoning effect: Hydrogen chemical potential μ_{H} at various locations along the length of the purifier and through the composite membrane. Reformate conditions: $P_{\text{reformatate}} = 379$ kPa, total flow 2500 sccm (34% H₂, 18% H₂O, balance N₂). Sweep conditions: $P_{\text{sweep}} = 137$ kPa, total flow 400 sccm (25% H₂, balance Ar)..... 144

Chapter 1: Significance of H₂ purification in PEM fuel cell systems

1.1 Introduction

Proton exchange membrane fuel cell (PEMFC) systems for standalone power generation and auxiliary power generation in trucks are being developed for applications where the use of hydrocarbon fuels is necessary due to their availability and high energy density. PEMFC systems that operate on logistic fuels have potential advantages over those based on IC engines in terms of overall efficiency, reduced emissions, and overall noise. Table 1.1 compares actual performance metrics of advanced diesel generators to expected performance metrics of a liquid-fueled PEMFC generator of comparable output power. However, PEMFC systems that operate on hydrocarbon fuels require many complexities in design and operation. In addition to the fuel cell, such systems involve a hydrocarbon reformer, reformater purifier to extract H₂, and other balance of plant components. By modeling an example configuration of a liquid hydrocarbon fueled PEMFC system, the importance of different component performance metrics can be assessed. In particular, it becomes clear as H₂ recovery fraction of the membrane purifier critically affects the overall system efficiency, water balance and thermal management requirements. The importance of the membrane performance need for a detailed, high-fidelity mathematical model of the H₂ purifier is established, thereby laying the foundation for the rest of this PhD research work.

Table 1.1: Potential advantages of PEMFC systems over diesel generators^a

| | Existing 1980 vintage diesel generator ^b | ORNL ^c advanced POC ^d diesel generator | Potential PEMFC generator ^e |
|---|---|--|--|
| Weight (kg) | 403 | 242 | 181 |
| Volume (m ³) | 0.68 | 0.68 | 0.20 |
| Fuel consumption @ 3.5 kWe ^f weighted average | 2.16 | 1.63 | 1.14 |
| Fuel efficiency ^g | 17% | 23% | 32% |
| Noise (dBA @ 7m) | 70 | 65-68 | 60 |
| Emissions (g/ 3.5 kWh) | | NO _x = 42 PM ^h = 1 CO = 9.1 | NO _x = 0 PM = 0 CO = 0.95 |

In a typical hydrocarbon fueled PEMFC system, either reforming and/or partial oxidation of the hydrocarbon fuel is used to produce H₂-rich reformat from which near pure H₂ must be extracted to be suitable for current-day Nafion-based PEMFCs [1, 2]. Since both the fuel reformer and the PEMFC need water for operation, sustainable water management is also critical in standalone applications that are not

^a fueled by diesel or JP-8 and of comparable size (~ 5 kW)

^b as owned and operated by the US military

^c Oak Ridge National Laboratory, Oak Ridge, TN, USA

^d proof-of-concept

^e targets for the University of Maryland PEMFC system project

^f kilo-Watt electric output

^g based on lower-heating value (LHV) of fuel

^h particulate matter

connected to an on-demand water supply. Hence, in addition to fuel efficiency, water balance is a key metric for assessing PEMFC system viability.

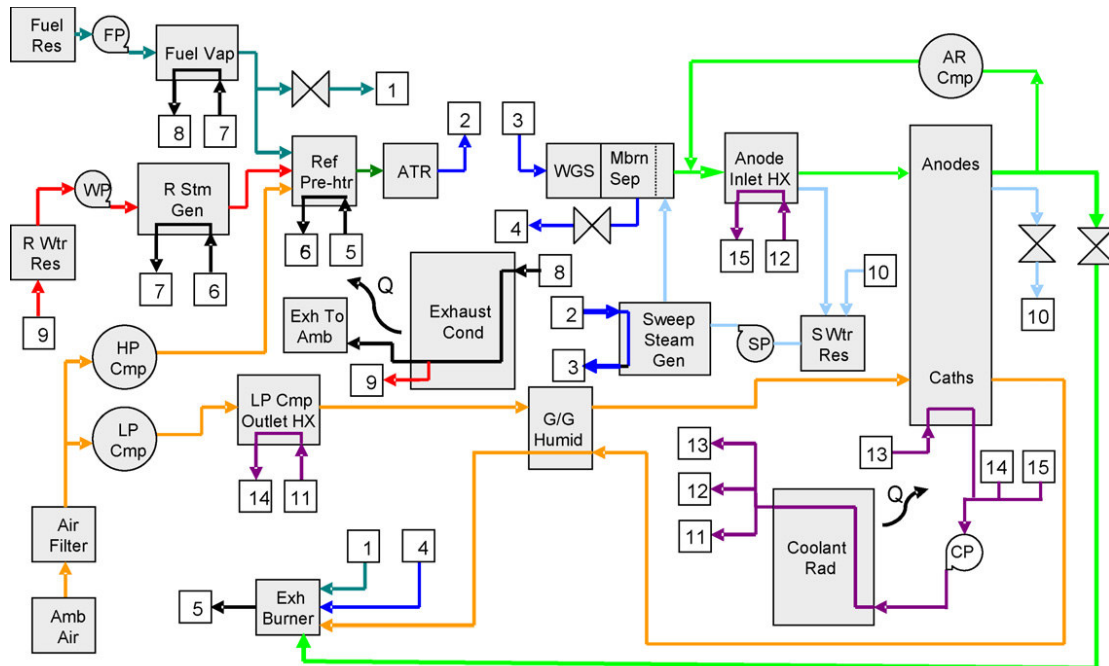
While significant work has been done on modeling individual components of a PEM fuel cell system, integrated system simulation (including balance-of-plant) presents a challenge for the design of actual fuel cell power generators. Simulating balance-of-plant is substantially more complicated when liquid hydrocarbon fuel processing and subsequent H₂ purification must be incorporated into the analysis. Recovering waste-heat and sustaining water balance in both the fuel processor and PEMFC stack require significant thermal integration and mass flow recycling. Consequently, it is difficult to evaluate single component operation outside of the context of the entire system. Integrated system models must include the PEM fuel cell stack, the fuel processing system (with steam and/or air input), a hydrogen purification process, and the requisite balance-of-plant components (liquid pumps, compressors, heat exchangers, and cooling loops). Detailed component models with multi-dimensional grids, such as for PEM fuel cell stacks [3-7] and for catalytic fuel processors [8-11] become computationally prohibitive for integrated system-level analysis for a broad range of operating conditions and design modifications. As a result, integrated system models [12-14] with lumped analysis for individual components have been used for evaluating system design and feasibility of complex integrated PEM fuel cell power plants with hydrocarbon fuel processors[15, 16].

1.2 Impact of Pd Membranes on PEMFC System Performance^a

1.2.1 System Description

The present analysis is for an example system designed to produce between 0.5 and 5 kW net power using a kerosene surrogate. By calculating mass and energy balances of the fuel processor, H₂ membrane, fuel cell system, and balance-of-plant, the model provides a critical assessment of important trade-offs between thermal efficiency and water balance and also of the necessary component performance requirements and operating conditions for efficient and sustainable system operation. Of the many possible flow configurations and thermal management strategies, the present analysis focuses on one particular configuration, as illustrated in Figure 1.1. The key features of this configuration are discussed below.

^a This section is a combined effort with Joshua B Pearlman, fellow graduate student at UMD, and others as cited in the bibliography.



LEGEND FOR CONNECTORS AND FLOWS

- | | |
|--|---|
| <ul style="list-style-type: none"> 1 Fuel supply to burner 2 Autothermal reformer to sweep steam generator (ref exh flow) 3 Sweep steam generator to water gas shift reactor (ref exh flow) 4 Retentate to exhaust burner 5 Exhaust burner to reformer pre-heater (burner exhaust flow) 6 Reformer pre-heater to reformer steam generator (burner exh flow) 7 Reformer steam generator to fuel vaporizer (burner exh flow) 8 Fuel vaporizer to condenser (burner exh flow) 9 Condensed water to reformer water reservoir 10 Condensate from anode recirculation loop to sweep water reservoir 11 Coolant radiator to LP compressor heat exchanger (cooling loop) 12 Coolant radiator to anode inlet heat exchanger (cooling loop) 13 Coolant radiator to stack cooling (cooling loop) 14 LP compressor heat exchanger to coolant pump (cooling loop) 15 Anode inlet heat exchanger to coolant pump (cooling loop) | <ul style="list-style-type: none"> — Liquid fuel — Air supply and cathode stream — Vaporized fuel / water / air mixture — Reformate and retentate — Liquid water and steam (fuel processor) — Liquid water and steam — Permeate and anode stream — Liquid coolant — Products from burner |
|--|---|

Figure 1.1: Schematic diagram showing realization of PEM fuel cell system integrated with liquid fueled ATR reactor, water–gas-shift/Pd-alloy-membrane reactor, and retentate exhaust burner for waste-heat recovery

Fuel is pumped through a fuel vaporizer and fed into a catalytic auto-thermal reformer (ATR). In the ATR, the fuel is reacted catalytically with pre-heated steam and air at operating temperatures ranging from 600 – 1000 °C to form reformate gas consisting primarily of H₂, H₂O, CO, CO₂ and N₂. Heat from the reformate gases is

used to make steam in a steam generator. The reformat may be further reacted in a water-gas-shift (WGS) reactor before being fed into a Palladium- (Pd-) based membrane purifier, where a large fraction of the H_2 is extracted for use in the PEMFC anode. While there are alternative H_2 purification technologies, the basis for choosing Pd-based membranes in this study are presented in Chapter 2. Some have proposed integrating the WGS catalyst with the Pd membrane purifier in a so-called membrane reactor to take advantage of the shifting equilibrium among the WGS gases as H_2 is selectively extracted along the length of the purifier [17-24].

The ATR and the reformat side of the purifier are maintained at an elevated pressure to create the necessary driving force for H_2 diffusion across the Pd membrane. While high-pressure water and fuel are delivered by liquid pumps, a high-pressure compressor with its high parasitic load is needed to supply air at the elevated pressure. The remaining gases from the purifier (also called retentate) still have recoverable chemical energy in the form of CO and residual H_2 . The retentate gases are reacted with the cathode exhaust in a catalytic burner, thereby recovering this energy in the form of heat that is used to pre-heat various gas/ liquid streams going into the fuel processor. After this, the gases are passed through an air-cooled condenser to recover water before being exhausted to the ambient.

The fuel supply to the PEMFC anode is managed with a recirculation loop that includes a recirculation pump. Steam is injected into the H_2 -depleted anode exhaust before being fed to the low pressure side of the Pd membrane purifier to sweep the

permeated H₂. The additional steam is introduced to maintain low H₂ partial pressure in the purifier, thereby increasing the available driving force for H₂ permeation through the Pd membrane. The H₂-rich mixture exiting the purifier is cooled using liquid coolant to about 70 °C in the anode inlet cooler before being fed to the fuel cell anode. Any water condensed in the cooling process is collected and used in the steam generator. Thus at steady state, the rate of production of H₂ from the purifier is balanced by the rate of consumption at the fuel cell anode, while the rate of injection of steam into the anode exhaust is balanced by the rate of condensation at the anode inlet cooler. However, there can be a need for purging the contents of the anode loop because of N₂ or contaminant build-up (detected directly by a drop in H₂ concentration or indirectly through a drop in cell voltages). Instead of wasting the H₂ in the loop and venting directly to the ambient, the anode loop is purged by opening a purge valve that exhausts into the catalytic burner, where the anode H₂ reacts with the cathode exhaust so that heat and water can be partially recovered.

To supply oxidant to the fuel cell cathode, atmospheric air is compressed using a low-pressure compressor. The compressor exhaust is cooled in a gas-liquid heat exchanger, and humidified using a gas-to-gas humidifier, before being sent to the cathode. The O₂-depleted cathode exhaust, after humidifying the cathode inlet air, is sent to the catalytic burner, where it provides the necessary O₂ for retentate combustion.

A liquid coolant loop removes heat from the fuel cell stack, in addition to cooling heat exchangers for the anode recirculation flow and cathode inlet flow. The coolant is circulated through a fan-cooled radiator, where the accumulated heat is rejected to the ambient.

1.2.2 System Modeling Approach

The model data is imported into MS Excel with a complex Visual Basic program running as a macro that determines steady-state operating conditions and system performance through a nested iterative sequence. The recycling of mass and heat flows, along with the feedback between system operating conditions and parasitic loads, requires such an iterative solution technique. A given iteration works by using current values for flow rates and parasitic power losses for the system to determine a new value for power produced by the fuel cell stack. This power demand is then used to recalculate fuel and air flows, thermal loads for cooling components, and associated parasitic loads (from compressors, pumps, and cooling fans) for system operation. Fuel flow rate to the system is determined iteratively through a species balance to satisfy H₂ demand from the Pd-alloy-membrane purifier. The new flow rates thus are used to update the parasitic loads, and gross power demand for the fuel cell stack is calculated from the sum of net power demand and the parasitic loads.

An iterative solution technique is used to determine temperatures in each component to satisfy entropy constraints and energy balances. Successively repeated iterations that solve species and energy balance equations are conducted until the following

criteria were met: (1) The difference in overall gross power demand and fuel cell power produced are within 10^{-4}W , (2) The internal enthalpy balance for each component is within 10^{-3}W , (3) The molar balance for the fuel cell anode recirculation loop is within $10^{-9}\text{ gmol s}^{-1}$. The iterative solver thus provides a steady-state solution of flow conditions and also necessary parasitic loads from compressors and pumps and fans for heat removal. Thermodynamic properties are calculated based on JANAF tables. Thermodynamics of surrogate kerosene ($\text{C}_{12}\text{H}_{23}$) is used for the liquid fuel [25]. Liquid enthalpies are calculated by subtracting the heat of vaporization and subsequent sensible heat removal (based on a constant liquid C_p) from the gas-phase value.

Most components as shown in Figure 1.1 are simulated with zero-order thermodynamic models. Exceptions include the combined water–gas-shift/ Pd-alloy-membrane reactor, which is simulated by a 1D flow model in order to assess the shift in H_2 driving force across the membrane as a function of length through the reactor. Models for critical heat exchangers (the exhaust condenser, coolant radiator, anode flow condenser, and air compressor outlet heat exchanger, all indicated in Figure 1.1) utilize component geometry to determine power needs for fans and coolant pump associated with those heat exchange processes.

The fuel cell stack is modeled as a liquid-cooled isothermal reactor with cell voltage, V_{cell} , versus current density, i ($\text{A}\cdot\text{cm}^{-2}$), defined by a polarization curve comparable to recently published data for a system based on Ballard Power Systems technology

[26]. An energy balance is used to calculate the coolant flow load and the consequential pump and fan work required for the fuel cell radiator loop. The gas-to-gas humidifier, which recaptures humidity for the cathode inlet from the cathode exhaust, is assumed to be large enough to humidify the cathode inlet flow to saturation at its exhaust temperature. For the fuel cell stack model, the water balance requires knowledge of where the water product is removed (either with the anode or cathode flows). In this study a net fraction of 15% product water back to the anode is used as a constant stack average value, consistent with some experiments on thin-film Nafion PEMFCs [27].

Fuel conversion in the ATR takes place through reactions with both steam and O_2 . Steam-to-carbon (S/C) and oxygen-to carbon (O/C) ratios are user-specified inputs and set high enough for sufficient H_2O and O_2 inputs to achieve complete fuel conversion. The exit reformate composition is based on water–gas-shift equilibrium of H_2 , CO , CO_2 and H_2O at the calculated outlet temperature. For the cases presented here, the fuel processor inlet temperature $T_{\text{reformer,in}}$ is not allowed to increase above $500\text{ }^\circ\text{C}$, assuming sufficient heat input for water and fuel vaporization, with subsequent gas flow preheating. While $T_{\text{reformer,in}}$ is adequate for all reactor conditions with an exothermic reactant mixture, it is too low for conditions where endothermic steam reforming is the dominant reaction. The current study includes an analysis of the performance trade-offs between varying S/C and O/C ratios, with the sum of these held constant at 2.4 and a slightly exothermic baseline case of S/C = 1.6 and O/C = 0.8.

The water–gas-shift/Pd-alloy-membrane reactor is modeled with the reformat stream and the sweep stream in counter-flow. The integrated water–gas-shift reaction increases H_2 driving potential along the length of the Pd-alloy-membrane. Furthermore, as gases flow along the length of the reactor, H_2 diffusion across the membrane favors additional H_2 production in the reformat stream to maintain equilibrium. To simulate this effect more accurately, the water–gas-shift reactor is discretized into four segments with local energy balances solved iteratively to determine temperature and mole fraction profiles along the length of the reactor. In the discrete approximation, the water–gas-shift reaction is assumed to reach equilibrium at the entrance to each segment.

The reactor is assumed to be of sufficient size that H_2 diffusion is not limited by mass transfer. Therefore, the amount of hydrogen that diffuses through the membrane is based upon a specified H_2 recovery fraction. This represents the ratio of H_2 recovered through the membrane to the sum of H_2 entering in the reformat stream and H_2 produced through water–gas-shift in the membrane reactor. In the present study, membrane H_2 recovery fraction is varied with a baseline case set at 75%. Significantly higher H_2 recovery efficiencies are not considered feasible with an ATF, because of the loss of H_2 partial pressure difference that serves as a driving potential across the membrane.

The low-pressure-air compressor supplies air to the fuel cell cathode. Inlet conditions are set to ambient, and the outlet pressure is determined to match the cumulative pressure drop through components in the cathode loop. The outlet enthalpy and temperature are determined from an isentropic efficiency, which is determined through cubic polynomials fitted to publicly available data for a rotary vane compressor. These account for variations in pressure ratio and mass flow rate. The required work input is then determined by the enthalpy change through the compressor, plus any heat loss to the ambient. A similar approach is adopted for the high-pressure air compressor for the fuel processor and for the anode recirculation compressor models, except that isentropic efficiency depends only on pressure ratio. Power required by the coolant pump, reformer water pump, fuel pump, and sweep steam water pump are determined from the isentropic value divided by a user-specified isentropic efficiency. For the relatively small power demand of the pumps compared to other parasitic loads in the system, isentropic efficiencies are simply set constant at 0.50.

Individual heat exchanger models for the exhaust condenser, low-pressure-air compressor cooler, anode flow condenser, and coolant radiator are based on geometry (appropriate to each heat exchanger), with corresponding heat transfer and pressure drop correlations, intended for maximum heat rejection in minimal volumes. For the exhaust condenser, a target outlet temperature for the system exhaust flow is defined as 10 °C higher than ambient temperature, but not less than 30 °C because of the diminishing benefit in water recovery below this point. The cooling air velocity

requirement for the exhaust cooling load is determined using heat transfer correlations in the literature. To prevent uncontrolled growth in condenser fan power under high heat load conditions, the model relaxes burner exhaust gas outlet temperature such that the cooling air velocity does not exceed $3 \text{ m}\cdot\text{s}^{-1}$. Based on the air velocity, the air-side pressure drop is calculated using correlations from literature. Fan power is determined by calculating the enthalpy difference required to drive air through the calculated pressure drop, in combination with characteristic isentropic efficiency maps.

Calculations in the coolant loop radiator are handled similarly to those in the exhaust condenser, with the exception that there is no need to control the fan speed as this was bounded for all cases in this study. The anode flow condenser transfers heat from hot anode gas to the coolant loop. Calculations for this condenser are done similar to those for the exhaust condenser by using literature values. The coolant outlet temperature is limited to $\leq 90 \text{ }^\circ\text{C}$ to prevent boiling. This has the effect of enforcing a minimum coolant mass flow rate through the heat exchanger. Appropriate safeguards are built into the model to ensure compliance with second law, and maintain positive coolant flow. No condensation takes place in the air compressor outlet heat exchanger, but it is otherwise similar to the anode flow condenser. Both heat exchangers use the same modeling approach.

Exhaust gas from the retentate burner provides heat inputs to the reformer steam generator, fuel vaporizer, and reformer preheater. Each of these is represented by a

zero-order model that determines the burner exhaust outlet temperature iteratively to satisfy an enthalpy balance. Maximum allowable outlet temperatures are specified for the flows being heated. A zero-order model also represents heat rejection from the fuel cell stack to the coolant loop. In this model, the coolant outlet temperature is limited to 80 °C in order to prevent excessive stack temperature and the accompanying risk of Nafion membrane dry out.

1.2.3 System Model results

Results from the system model identify how critical parameters influence both overall efficiency and water balance for the integrated power plant. Baseline conditions for user-specified variables used in the current system simulations are provided in Table 1.2.

Table 1.2: Critical baseline system parameters

| <i>Parameter</i> | <i>Value</i> |
|--|--------------|
| Ambient conditions | |
| Temperature, T_{amb} (K) | 303 |
| Relative humidity, ϕ_{amb} | 50% |
| Fuel cell conditions and properties | |
| Operating temperature, T_{cell} (K) | 338 |
| Pressure drop across stack at 1 A cm ⁻² current density (bar) | 0.5 |
| Stoichiometric ratio of cathode air flow | 1.8 |
| Stoichiometric ratio of anode H ₂ flow | 1.5 |
| Fraction of water produced in fuel cell transported to anode | 15% |
| Number of cells per stack | 25 |
| Stack membrane area per cell (cm ²) | 487 |

| <i>Parameter</i> | <i>Value</i> |
|--|--------------|
| Current density at 8000 W gross power, i_{ref} (A cm ⁻²) | 1.0 |
| Fuel reformer (ATR) conditions | |
| Inlet oxygen to carbon (O/C) ratio | 0.8 |
| Inlet steam to carbon (S/C) ratio | 1.6 |
| Maximum inlet temperature, $T_{ref,in,max}$ (K) | 773 |
| Minimum pre-heater approach temperature (K) | 20 |
| Minimum approach temperature for steam generator (K) | 40 |
| Maximum temperature out of steam generator (K) | 470 |
| Water–gas-shift membrane reactor conditions | |
| Differential pressure across membrane (bar) | 6.0 |
| Sweep steam to H ₂ ratio in the membrane separator | 0.20 |
| Membrane reactor H ₂ recovery fraction | 75% |
| Temperature out of the sweep steam generator (K) | 450 |
| Balance-of-plant conditions: | |
| Radiator coolant outlet temperature (K) | 333 |
| Burner exhaust condenser temperature difference (K) | 10 |
| Electric inverter efficiency | 93% |
| Electric motor efficiency | 90% |

For a given simulation condition, the overall system efficiency η_{th} is found from equation (1.1), which shows η_{th} in terms of fuel cell power out, parasitic loads \dot{W}_{lost} , and enthalpy input of the hydrocarbon fuel in $\dot{m}_{HC,in}h_{HC,comb}$.

$$\eta_{th} = \frac{\dot{W}_{net}}{\dot{Q}_{HC}} = \frac{n_{cells} A_{cell} i V_{cell} - \dot{W}_{lost}}{\dot{m}_{HC,in} h_{HC,comb}} \quad (1.1)$$

η_{th} can be broken up into three components: the combined efficiency of the fuel processor and Pd-alloy-membrane η_{FP} , the efficiency of the fuel cell itself η_{FC} , and the efficiency of the balance-of-plant η_{BOP} . These three sub-system efficiencies are shown in each expression in parenthesis in the right-hand-side of equation (1.2).

$$\eta_{th} = \eta_{FP}\eta_{FC}\eta_{BOP} = \left(\frac{\dot{m}_{H_2,memb} h_{H_2,comb}}{\dot{m}_{HC,in} h_{HC,comb}} \right) \times \left(\frac{n_{cells} A_{cell} i V_{cell}}{\dot{m}_{H_2,memb} h_{H_2,comb}} \right) \times \left(\frac{n_{cells} A_{cell} i V_{cell} - \dot{W}_{lost}}{n_{cells} A_{cell} i V_{cell}} \right) \quad (1.2)$$

η_{FP} is proportional to the H₂ membrane recovery fraction which in this model is set constant, and variations in η_{FP} are primarily due to changes in the S/C and O/C ratios of the fuel processor. η_{FC} is proportional to V_{cell} because for the recirculated anode flow at steady state, i will be proportional to $\dot{m}_{H_2,memb}$. Thus, as V_{cell} drops with higher i and higher stack power densities, η_{FC} will tend to fall off, and this decrease in η_{FC} with increased power can more than offset improved efficiencies in the compressors as they approach their capacity with increased system power.

The chief purpose of elucidating the system model in this chapter is to describe the sensitivity of system efficiency and water balance of the PEMFC system to the H₂ purifier recovery fraction; hence only selected results from the system modeling studies are presented here. However, it is important to discuss results that have implications for the design and control of almost all components in the system,

including the membrane purifier. Figure 1.2 shows η_{th} as a function of \dot{W}_{net} for 3 different T_{amb} : 10, 30, and 50 °C. For all three T_{amb} , η_{th} decreases as \dot{W}_{net} rises above 1500W. This is due to the drop in η_{FC} . The decrease in η_{th} at low power densities is due to the large decrease in η_{BOP} caused by relative increases in the compressor and fan loads \dot{W}_{lost} to fuel cell power output \dot{W}_{gross} as \dot{W}_{net} decreases below 1500W as illustrated for all T_{amb} in Figure 1.2.

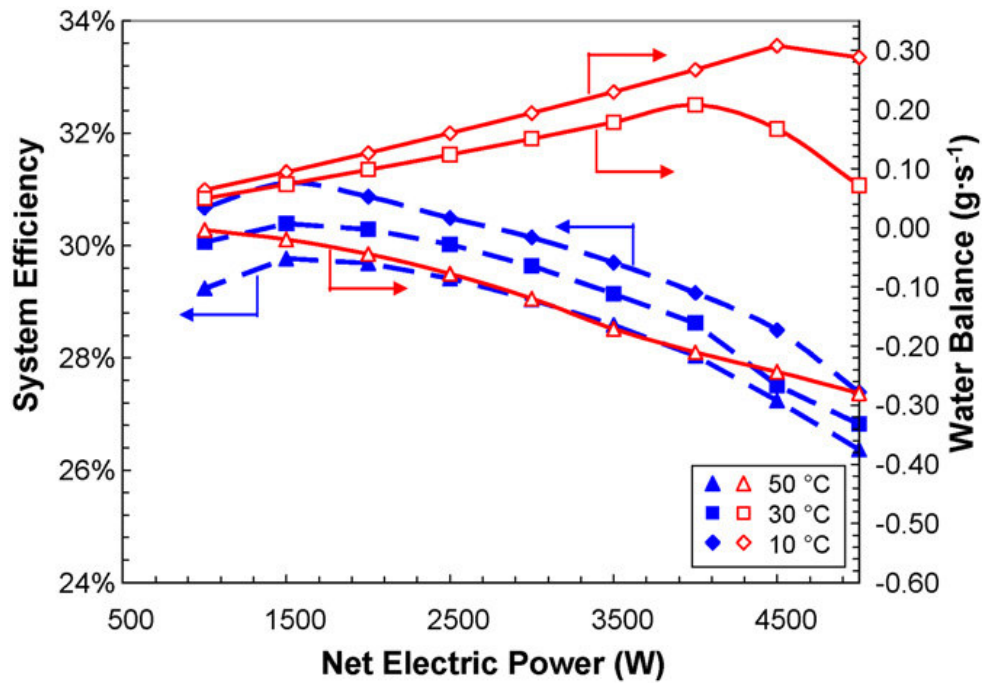


Figure 1.2: Overall system efficiency and total water balance (in g s^{-1} accumulated) as functions of net electric power for the liquid-fueled PEM fuel cell system at baseline conditions (see Table 1.2) at three different ambient temperatures. Numbers on top of bars indicate T_{amb} .

The trends in η_{th} as a function of \dot{W}_{net} are consistent at all 3 T_{amb} , but also as shown in Figure 1.2, there is a monotonic decrease in η_{th} with increasing T_{amb} . This is due to

an increase in \dot{W}_{lost} due to compressor loads rising with T_{amb} . The drop in η_{th} is approximately 2% points for each 20 °C rise in temperature, and this result shows the importance of stating system efficiency values at a given T_{amb} .

For a small-scale fuel cell generator, changes in total parasitic loads \dot{W}_{lost} with operating conditions determine how η_{BOP} influences the overall η_{th} . Figure 1.3 shows changes in parasitic loads with \dot{W}_{net} at three T_{amb} (for the otherwise baseline conditions). The parasitic loads are broken out into groups of components—the LP compressor for the cathode flow, HP compressor for the reformer air supply, cooling fans for the fuel cell radiator and exhaust condenser, and pumps (including all liquid pumps and the anode recirculation compressor). At the baseline reformer conditions (S/C = 1.6 and O/C = 0.8), the LP and HP compressors are the chief contributors to the parasitic power demand. Both compressor demands increase similarly with \dot{W}_{net} and T_{amb} .

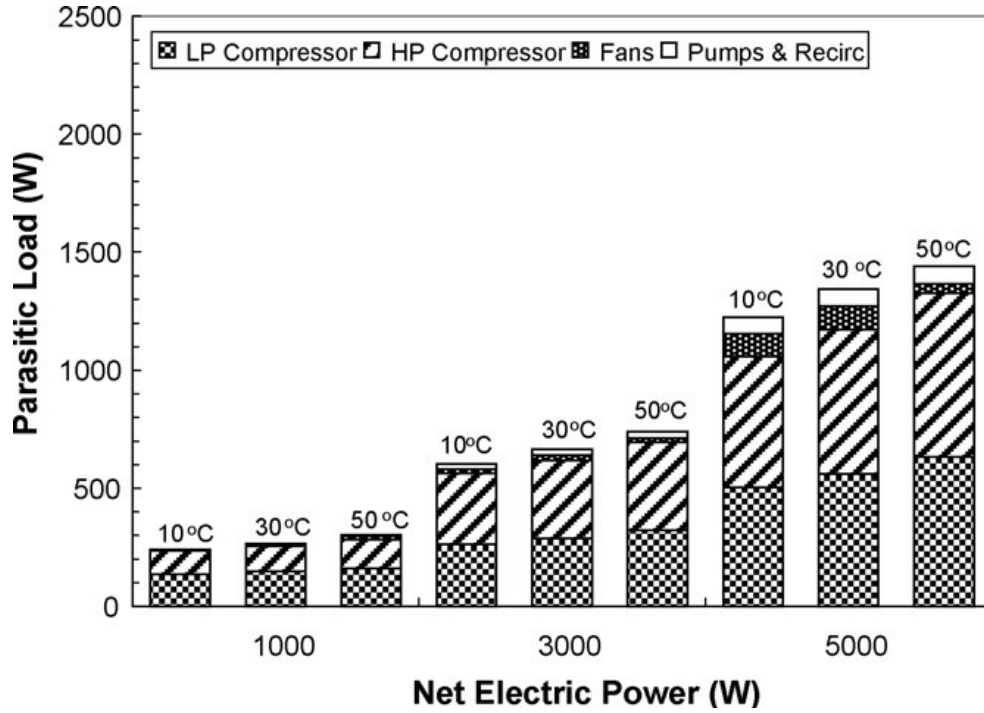


Figure 1.3: Parasitic loads for LP and HP compressors, cooling fans, and liquid pumps for the liquid-fueled PEM fuel cell system at baseline conditions (see Table 1.1) at three different ambient T_{amb} and \dot{W}_{net}

In addition to η_{th} , overall system water balance is a critical measure of the system performance. Water balance is measured by the difference between the water collected from the exhaust condenser and the anode inlet heat exchanger (condenser) and the amount of water demanded by the fuel processor and the sweep steam for the low-pressure side of the Pd-alloy-membrane.

For this PEMFC generator with a liquid-fuel reformer and a Pd alloy- membrane purifier, η_{th} is very sensitive to both the fuel cell operation voltage (through η_{FC}) and the membrane H_2 recovery fraction (through η_{FP}). As η_{FP} increases, decreased fuel consumption requires less air and water flow rates to the fuel processor, which lowers

parasitic power consumption and thus increases η_{BOP} . Increases in membrane recovery fraction improve η_{FP} and thus η_{th} as shown in Figure 1.4.

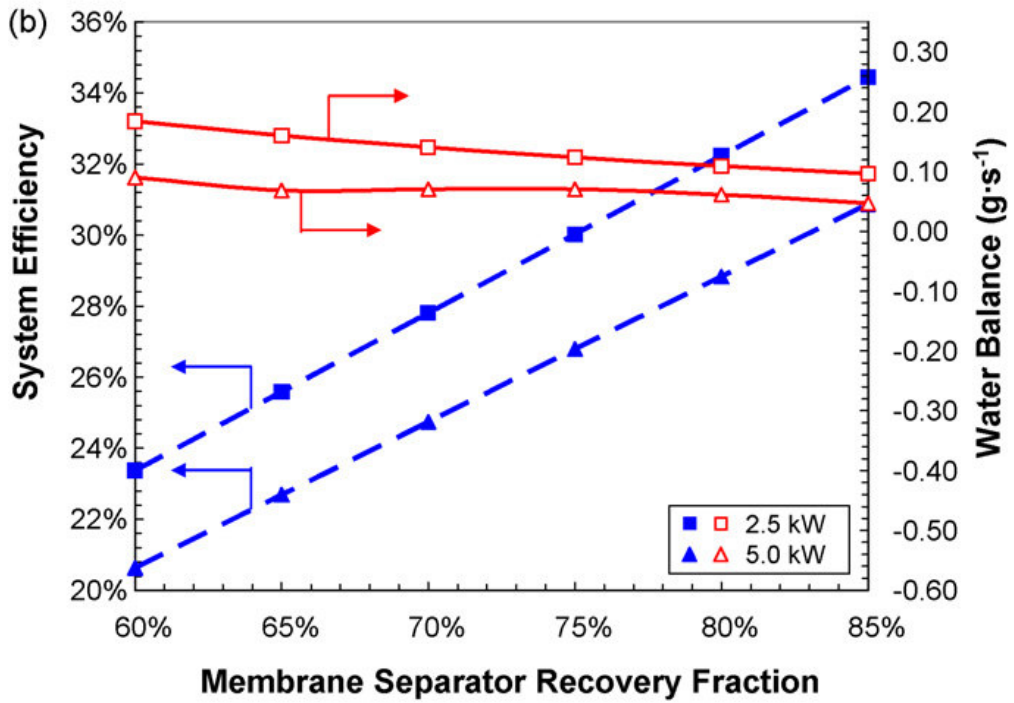
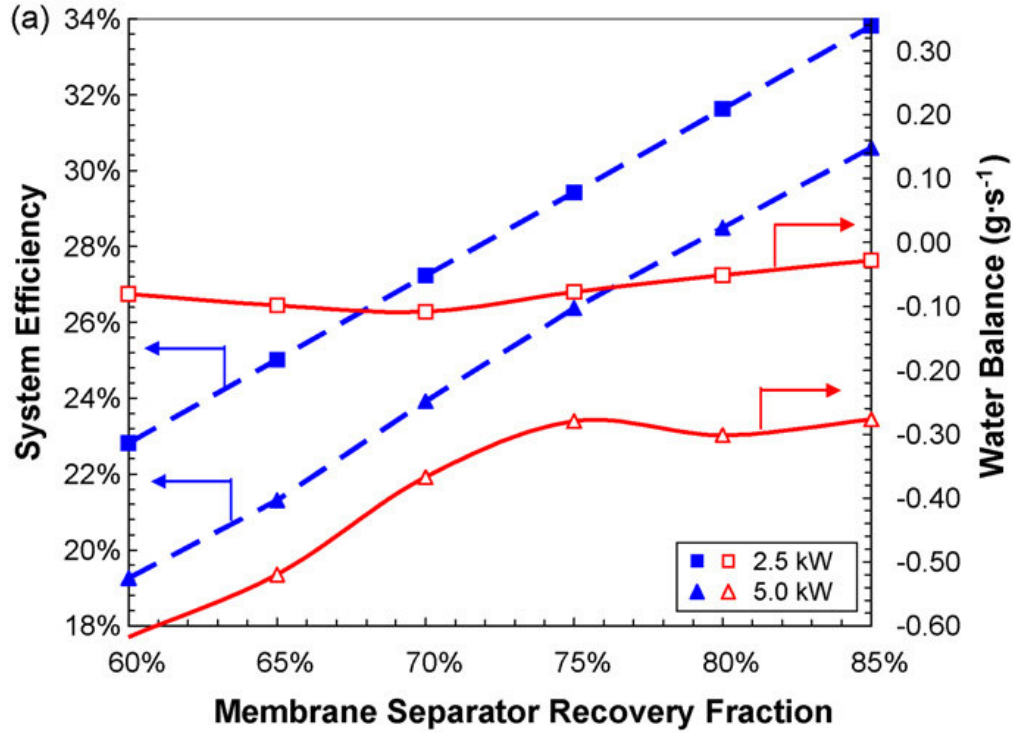


Figure 1.4: System efficiency η_{th} and total water balance as functions of H₂ recovery fraction of the purifier for full-load and half-load conditions: (a) $T_{amb} = 50\text{ °C}$ and (b) $T_{amb} = 30\text{ °C}$.

The recovery fraction of the Pd-alloy-membrane not only impacts η_{th} , but also the operating temperatures of many of the system's components. Figure 1.5 illustrates the effect of recovery fraction on a range of critical high T locations associated with the fuel processor and the exhaust burner. For lower membrane recovery fractions, the increased H_2 content in the retentate flow results in a higher outlet temperature from the exhaust burner. Since the amount of heat that can be recovered from the system is limited, any extra heat must be rejected to the ambient, which significantly reduces η_{th} . This drop in η_{th} with reduced membrane recovery fractions is exacerbated by higher T_{amb} . At lower T_{amb} as shown in Figure 1.4a, sufficient water can be recovered from the burner exhaust condenser to achieve a net positive water balance across a range of membrane recovery fractions. By contrast, at high T_{amb} (50 °C) as illustrated in Figure 1.4b, the higher T_{exh} limits the water recovery and does not allow for improved water balances with reduced membrane recovery fractions. Thus, no benefits can be achieved by reducing membrane recovery fractions at high T_{amb} operation. The trends shown in Figure 1.4 indicate that the design and control of the water-gas-shift/membrane reactor and H_2 purifier is central to achieving an efficient and operable generator when it is chosen as part of the fuel processing sub-system.

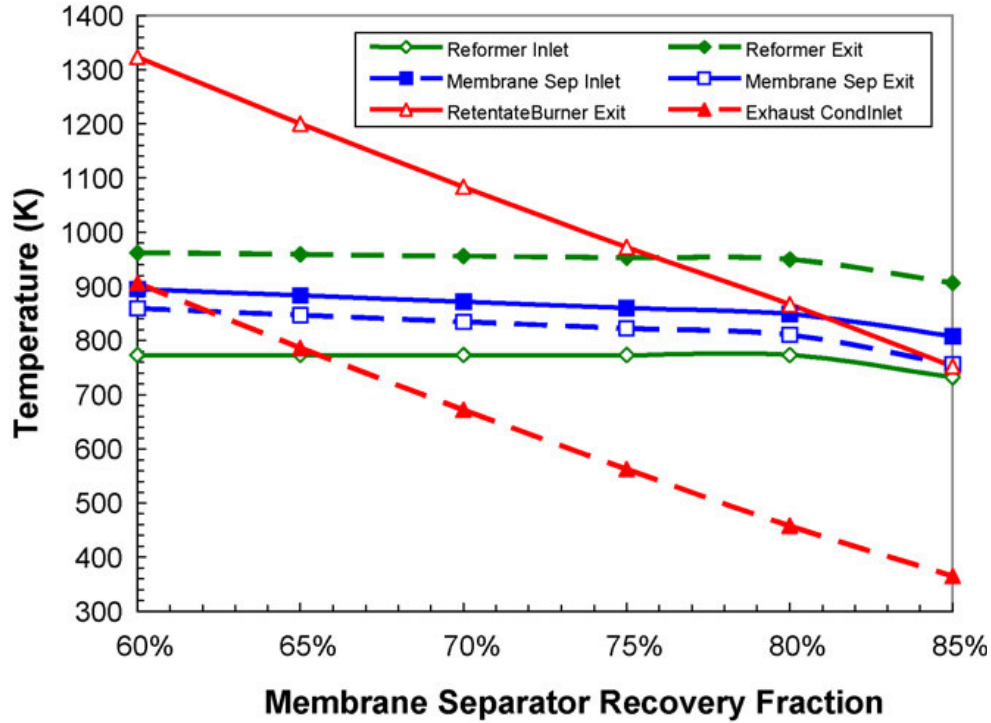


Figure 1.5: Critical system temperatures as functions of H₂ recovery fraction of the Pd alloy-membrane for $\dot{W}_{net} = 2.5$ kW at $T_{amb} = 30^\circ\text{C}$.

1.3 Additional considerations for H₂ purifier design

Although purifier efficiency is held constant for each run of the model, certain interactions between other system components and the purifier need to be considered for design and control of most important components in the system. For example, by pressurizing the reformat side of the purifier, the HP compressor creates the necessary H₂ driving force for the transfer of H₂ from the reformat side to the pure H₂ side. In the absence of mass transfer limitations, purifier recovery fraction can be increased by increasing HP compressor outlet pressure and thereby the driving force. However, the concomitant decreases in η_{BOP} and η_{FC} have to be taken into account before a decision on the design pressure for the HP compressor can be made. On the

other hand, a low reformat pressure increases the size of the purifier for a given recovery fraction, and also reduces the second-law limit on mass transfer between high pressure and low pressure sides of the purifier, thereby reducing the maximum allowable recovery fraction.

The purifier recovery fraction is also affected by the composition of gases on the low pressure (or pure H₂ side) of the purifier. During normal operation of the PEMFC using air as the oxidant, N₂ migration occurs from the cathode to the anode. This N₂ usually results in a decrease in η_{FC} due the dilution of H₂ concentration. However, the low pressure side of the purifier is part of a recirculation loop that includes the PEMFC anode, so that the H₂ depleted anode exhaust, mixed with additional steam, enters the purifier on this side. As will be discussed in this thesis, presence of N₂ in the anode exhaust increases H₂ recovery fraction in the purifier by increasing the available H₂ driving force across the membrane. Therefore in actual implementation, there is a trade-off between purifier recovery fraction and η_{FC} corresponding to the N₂ concentration in the anode. Moreover, N₂ in the anode loop adds to the throughput of the anode recirculation pump, thereby increasing its electric demand and decreasing η_{BOP} . Taking into account the above considerations, if an optimum N₂ concentration can be determined for a given set of system operating conditions, the anode purge frequency can be adjusted so as to maintain this target concentration. It can be seen from the above discussion that the design and control of the HP compressor, ATR, H₂ purifier, PEMFC and the anode recirculation pump are strongly inter-dependent.

As will be discussed in greater detail in subsequent chapters, the high cost of Pd makes it important to limit the use of the metal in commercial power applications. Therefore, thin film (~1-10 μm thick) membranes have been targeted for fuel cell systems designs and numerous research efforts are ongoing to develop portable. Due to the large cross-membrane differential pressures such as those in this system realization, these thin film membranes have to be supported by depositing them onto a porous matrix such as α -alumina or porous stainless steel (PSS). Although Pd use is limited through the use of this porous support, it adds to the weight, volume and thermal mass of the purifier, thereby introducing additional complexities in packaging, thermal management and transient operation.

Yet another consideration is the integration of a catalyst that promotes the water-gas shift (WGS) reaction ($\text{H}_2\text{O} + \text{CO} \rightleftharpoons \text{H}_2 + \text{CO}_2$) on the reformate side of the membrane purifier to take advantage of the shifting equilibrium along the length of the purifier as H_2 is selectively extracted. Although the integrated WGS-membrane reactor increases H_2 driving force, and therefore higher recovery fraction (or smaller size for a given recovery fraction) than a similarly sized Pd membrane purifier without the WGS, this advantage needs to be quantified so that it can be weighed against (a) added design complexities involved with the integration of such a catalyst, (b) alternative design approaches such as coupling a WGS reactor in series between two Pd membrane purifiers.

Competing technologies to Pd-based membrane purification are being developed for H₂ purification in PEMFC system applications (for example see [28] and [29]). While it is certainly not in the scope of this dissertation to critically evaluate and compare the different technologies, a high-fidelity mathematical model for the Pd-membrane based approach is a powerful tool from a system development viewpoint, as it can aid, through parametric studies, in evaluating the limits of performance of this technology.

1.4 Summary

PEMFC based generators that can run on liquid-hydrocarbon fuels offer many potential advantages over those based on traditional IC engines. However, due to its complexity, several important design and control trade-offs must be understood before a successful system can be built. The system modeling work presented in this chapter, helps to understand the trade-offs among key system performance metrics such as efficiency and water balance.

The Excel-based model with an iterative macro program utilizes a steady state system calculator. The combined WGS-membrane reactor for H₂ purification is represented through a 1-D model that captures the shifting equilibrium among WGS gases as H₂ is selectively removed from the reformate gases. For a system that produces between 0.5 and 5.0 kW net electric power, model results indicate that purifier H₂ recovery fraction is very critical to system efficiency, water balance and thermal management. Furthermore, there are minimum and maximum limits of this recovery fraction

(depending on the particular system operating conditions and the ambient) beyond which sustainable system operation is not possible. Purifier efficiency in turn is affected by design and control choices on many other components such as the HP compressor, the ATR, the anode recirculation pump and the fuel cell itself. Therefore, a detailed mathematical model that captures the physics of H₂ purification across a broad range of operating conditions is a valuable tool not only in the design and control of the purifier, but also in evaluating decisions on a number of key system components.

Chapter 2: Literature review of Pd-based membranes and objectives of current study

2.1 Introduction

In this chapter, the construction and working of a Pd-based membrane reactor for H₂ purification in standalone PEMFC applications is presented. The need for developing a mathematical model for the design, optimization and control of such a membrane purifier is established. Then, the membrane reactor modeling literature is reviewed. Important limitations of existing models form the basis for the motivation to build and validate a new mathematical model for Pd-based membrane reactors.

As shown in Chapter 1, H₂ purification plays a central role in standalone PEMFC systems that run on hydrocarbon fuels. There are three major approaches to separating H₂ from reformat gases: (1) pressure-swing adsorption (PSA), (2) fractional distillation, and (3) membrane separation. Currently, membrane separation is considered to be the most promising for portable power applications because of low energy consumption, possibility for continuous operation, lower volume, ease of operation, and cost effectiveness [30].

2.1.1 Membrane purifier and membrane reactor

The concept of a membrane purifier is shown in Figure 2.1.

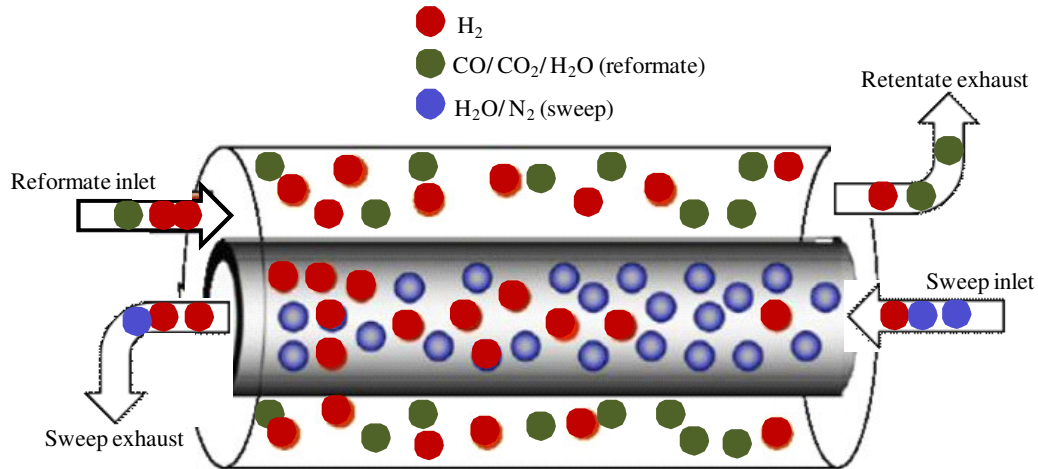


Figure 2.1: Schematic illustration of a membrane purifier operated in counterflow mode: reformate gases ($\text{H}_2 + \text{CO} + \text{CO}_2 + \text{H}_2\text{O} + \text{N}_2$) enter the shell side of the purifier from the left. H_2 depleted reformate gases (also called retentate) leave the purifier on the right. Sweep gases (typically H_2O and/ or N_2) enter the inner tube from the right side. The H_2 -rich stream exits on the left side and is fed into the PEMFC anode.

H_2 perm-selective membranes separate reformate and sweep gases that are fed into the high-pressure side of the purifier, typically in a counterflow arrangement. Just as in heat exchangers, the most common geometries are planar and cylindrical. At any location along the length of the purifier, the H_2 partial pressure difference between the two gas streams is the fundamental driving force for H_2 transfer. The H_2 transfer may occur via various different processes, depending on the type of membrane employed. To increase this driving force and reduce the size of the purifier, the reformate gases are usually maintained at an elevated pressure. Similarly, the H_2 partial pressure on the sweep side must remain adequately low either by the use of a vacuum pump, or by sweeping the H_2 using a “sweep” gas [19, 21, 31-34].

A catalyst that promotes the water-gas shift reaction ($\text{H}_2\text{O} + \text{CO} \rightleftharpoons \text{H}_2 + \text{CO}_2$) can be integrated into the reformat side of the membrane purifier to take advantage of the shifting equilibrium as H_2 is selectively withdrawn, thereby providing increased H_2 driving force, while simultaneously reducing CO content. Such a purifier with integrated WGS is often referred to as a WGS membrane reactor.

The most promising H_2 membrane materials are metals, silica, zeolites, carbon-sieves, and polymers. Due to their simultaneous high permeability and H_2 selectivity, metallic membranes are attractive for small PEMFC applications [35]. This is especially true because these membranes are theoretically impermeable to CO, which is present in hydrocarbon-reformat streams and detrimental to low-temperature PEMFC performance [1, 2, 36]. Metallic membranes are also impermeable to other PEMFC poisons such as H_2S , which effectively acts as an irreversible poison to PEMFC anode electrocatalysts [37].

2.2 Pd- H_2 and Pd-alloy- H_2 interactions

The Pd-Hydrogen system has been one of the most studied since Thomas Graham first discovered the diffusion of hydrogen through a hot Pd tube [38-40].

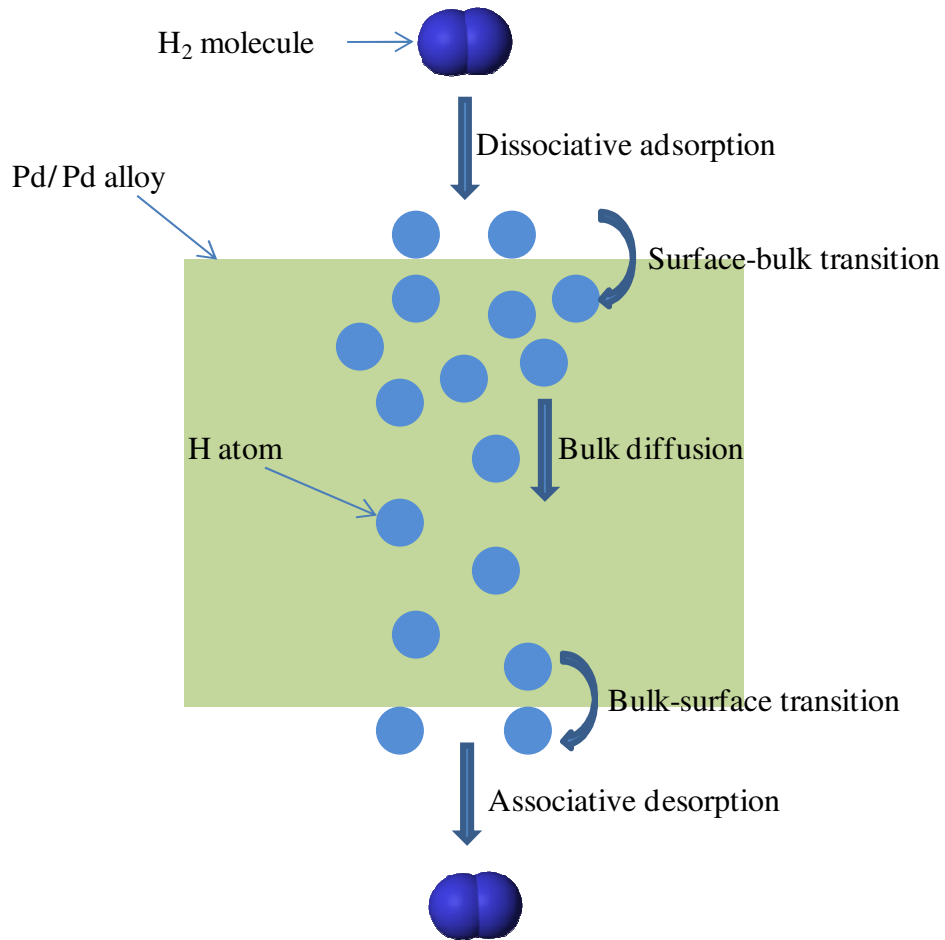


Figure 2.2: Steps involved in H₂ transport across a Pd-alloy membrane

Ward & Dao have summarized the hydrogen permeation mechanism through a Pd-alloy membrane as consisting of distinct steps [41], as shown in Figure :

- 1) molecular diffusion of H₂ from the bulk of the feed gas to the vicinity of the metallic surface
- 2) dissociative adsorption on to the metallic surface
- 3) transition of surface adsorbed H-atoms into the bulk metal
- 4) diffusion of H-atoms across the membrane bulk
- 5) transition to the permeate side surface

- 6) associative desorption from the metallic surface on the permeate side, and
- 7) molecular diffusion away from the surface into the bulk of the permeate gas.

The Pd-H system, just as most other metal-H systems, exhibits distinct phases depending on the temperature and composition: the dilute α -phase, the disordered β -phase and the mixed $\alpha+\beta$ phase (see [42] for an extensive review of the Pd-H phase diagram). The transition between these phases involves a discontinuous change in miscibility, and a concomitant discontinuous change of the Pd metal lattice constant. For the Pd-H system, the $\alpha \rightarrow \alpha+\beta$ transition occurs over a temperature and composition range that is encountered during start-up or shut-down of the purifier in a typical PEMFC system. This is the primary reason for alloying Pd with other metals such as silver, copper, gold and aluminum for H₂ membrane applications [43-48].

One of the most widely studied alloys is Pd_{0.77}Ag_{0.23}, which has a higher permeability to hydrogen compared to Pd [39, 45, 49-55]. For this alloy, the $\alpha \rightarrow \alpha+\beta$ transition occurs at a much lower temperature compared to pure Pd, thereby making it amenable to more aggressive start-up, shut-down and load cycling [56]. Furthermore, it has been found to be less susceptible than pure Pd to surface contamination by hydrocarbon reformat gases such as CO and H₂O [57]. Recently, there has also been a lot of interest in the Pd-Cu and Pd-Au alloys because of their high tolerance to sulfur compounds, which are present in varying quantities in JP-8 and diesel reformat gases [43, 47]. The $\alpha \rightarrow \alpha+\beta$ transition in some Pd-Au alloys occurs below

room temperature, thereby making them suitable for any kind of load and thermal cycling.

2.3 Pd membrane supports

Although Pd and its alloys have many advantages that make them attractive for portable PEMFC systems, their cost is a major concern in any commercial application. Other operating conditions being held constant, the H₂ flux through a Pd-alloy membrane is inversely related to its thickness (though not necessarily proportional). Hence, the total required membrane area reduces when thinner Pd-alloy membranes are employed. This in turn, results in a disproportionate decrease in the mass of precious metals (Pd or Pd + Au/Ag/Cu) required for the purifier. Thinner membranes also result in a purifier that has a rapid response to variation in H₂ demand. Because of the above reasons, very thin (~1-10 μm) Pd-alloy films are preferred as opposed to thick Pd-alloy sheets or tubes (> 20 μm).

However, thin films do not have the mechanical strength to withstand the cross-membrane differential pressures that are required to be maintained in order to increase permeance and limit the purifier size (described earlier in this chapter). For this reason, the films are supported on a porous matrix. Materials such as porous α-Al₂O₃ [49, 58, 59], porous YSZ [59], or porous stainless steel (PSS) [60, 61] are most commonly used for this purpose. The metallic film together with the porous support is called a composite membrane. Reviews of the development of Pd membranes for H₂ separation have been presented by several authors [35, 62, 63]. The minimum

thickness of Pd film that can be deposited on a porous substrate to make a reliable purifier depends inversely on the pore size. However, smaller pore sizes increase the resistance of the support to gas transport (discussed in detail subsequently). Hence, an intermediate nano-porous ceramic layer is usually applied on top of a meso-porous ceramic bulk substrate. In case of some PSS supports, the surface is oxidized before plating Pd to avoid inter-metallic Pd-Fe diffusion at higher temperatures [64].

2.4 Mathematical modeling of Pd membranes

Computational modeling efforts of Pd-based H₂ membranes have been mainly focused on two areas. The first area involves atomistic modeling using density functional theory (DFT) to predict the fundamental interactions between the alloy components and adsorbates from the gas phase [65-82]. These atomistic models explore preferred surface phases and energetics of hydrogen diffusion into the bulk of the metal alloy.

The second area of modeling is focused on macro-scale reactor design and often relies on high-level approximations such as modified Sievert's law, shown here in equation (2.1) [61, 83, 84].

$$J_{\text{H}_2} = \frac{K_{\text{H}}}{\Delta z_{\text{memb}}} \left[(P X_{\text{H}_2})_{\text{feed}}^n - (P X_{\text{H}_2})_{\text{permeate}}^n \right] \quad (2.1)$$

In equation (2.1), PX_{H_2} are the H_2 partial pressures on the high-pressure feed and low-pressure permeate side, Δz_{memb} is the Pd film thickness, and K_H is a fitting parameter. When $n = 0.5$, equation (2.1) becomes Sievert's law and K_H is referred to as Sievert's constant. The $n = 0.5$ condition implies that the hydrogen transport through a particular membrane configuration is dominated by the H-atom diffusion through the metallic membrane. On the other hand, when $n > 0.5$, it implies that other processes have some role in limiting the hydrogen transport, but the particular underlying physics are masked by the empirical fit. Therefore, models based on Sievert's law are not adequate for design of membranes for PEMFC system applications, as discussed in detail below.

Progress in membrane manufacturing technology has enabled very thin membranes, wherein surface processes have become increasingly important relative to bulk diffusion [45, 61, 85, 86]. Sievert's law assumes that the interaction rate between species on the surface of the metal and those just inside the metal are much faster compared to the time scales involved in diffusion through the bulk metal; in other words, the surface and the bulk metal in the immediate vicinity of the surface are assumed to be in fast equilibrium with each other. With very thin membranes, the bulk diffusion time scales are reduced, and hence the rates of surface-bulk interactions become important.

The second reason for the giving importance to surface processes is competitive adsorption. Gao et al have published a review of the chemical stability of Pd and Pd

alloys [57]. The main challenges to chemical stability are the presence of CO, H₂O and sulfur compounds like H₂S in the feed gas, which are bound to be present in differing quantities depending on the type of fuel used and the type of reformer upstream of the H₂ purifier. While all these species result in a decrease of H₂ flux through the composite membrane (compared to a pure H₂ feed at the same H₂ partial pressure), the effects of CO and H₂O are considered reversible i.e. the H₂ flux can be recovered by passing an inert gas for a few hours at high temperatures. This has led to the conclusion that CO and H₂O compete with H₂ to adsorb on the Pd surface sites, thereby reducing the number of sites available for H₂ desorption.

The effects of competition for Pd surface sites for the various reformate gases including H₂, CO, H₂O and smaller hydrocarbons need to be incorporated in order to realistically assess trade-offs involved in the design and operation of membrane purifiers in hydrocarbon-fueled PEMFC applications [87]. H₂ and H₂O competition for sites can also be important when steam is included in a sweep gas across the low-pressure side of the H₂ membrane.

Recently, Unemoto et al have published papers on the effects of these co-existing gases such as CO, H₂O and CH₄ on Pd_{0.77}Ag_{0.23} [46, 87]. In these papers, they have also summarized a number of similar studies carried out on Pd and Pd-alloys. They found that CO and H₂O do not affect the H₂ flux through a 20μ membrane at temperatures higher than 630K. However, other authors have reported reduction of H₂ flux in the presence of CO even at about 670K [56, 88-90]. Some of these studies

have also attempted to develop a mathematical model for H₂ permeation in the presence of CO by using empirical fits to experiments. These do not take into account the energetics of H₂/ CO/ H₂O adsorption or the interaction among surface species or the presence of adsorbing gases on the permeate side of membranes, and hence are unlikely to be valid over a wider range of operating conditions. Moreover, the effects of reformat gases differ considerably with the alloy used.

The activity of H on a Pd-alloy surface or inside the metallic bulk is a function of the H-concentration itself. Therefore, the thermo-kinetics of H₂ adsorption, solution and diffusion through Pd alloys are influenced by the local H-concentration in the metal, and these non-ideal effects become more important at low temperatures (~ 300 °C) [91, 92]. These will be discussed in more detail in the next chapter.

As discussed in the previous section, Pd-alloy membranes are often supported on porous substrates to provide mechanical stability. The substrates add to the H₂ transport resistance of the Pd film. Whereas in case of thicker membranes (>20 μm), this substrate resistance can be largely ignored, it becomes significant as the thickness and thus resistance of the metallic membrane is reduced with thinner (< 10 μm) Pd-alloy membranes derived from improved coating technologies. Many recent experimental studies have demonstrated the significance of the support-layer resistance [35, 52, 56, 60, 61, 83, 84, 93-101]. Some of these studies were carried out with thicker (> 20 μm) Pd films such that the support layer resistance was not a significant contribution. One of the recent studies speculates that Pd-Al interactions

may influence Pd membrane permeance due to detrimental Pd-Al reactions [59]. Differences in supported membrane fluxes may also be attributed to how the dense Pd membrane interfaces with porous substrates and how that interaction adds to the resistance of H₂-transport through the supported composite membrane. The rough porous substrates also influence membrane surface morphology and thus the thickness and quality of the Pd layer itself [84]. Optimizing such composite membranes is important for the effectiveness, response time and cost considerations in a typical fuel cell system.

2.5 Summary and need for a new mathematical model

As demonstrated by the experimental work of Peters et al [56], and modeling studies of Barbieri et al [102], detailed understanding of trade-offs associated with Pd-membrane design parameters such as membrane thickness, membrane support pore structure, and gas-flow channel geometry is required to effectively integrate a membrane purifier with a fuel cell system. Therefore, an accurate model for H₂ permeation through Pd-based membranes across a wide range of membrane thicknesses and operating conditions can play a critical role in implementing these membranes into hydrocarbon fuel processing for PEMFC systems.

Some previously published models fit experimentally observed data by adjusting the $\frac{1}{2}$ pressure exponent in Sievert's law (equation (2.1)) to a value between 0.5 and 1, in addition to fitting K_H . However, such a modification of the exponent does not fully

demonstrate the physics involved, and hence the parameters derived through this process usually only apply to a limited range of operating conditions.

Recent efforts have begun to incorporate surface processes to understand the performance of thin Pd-based membranes for H₂ purification. Ward and Dao [41] have estimated parameters for the multi-step mechanism for pure H₂ permeation through Pd membranes discussed in the previous section. However, there is no evidence that this model predicts solubility of H in Pd (it will be shown in this thesis that predicting solubility is a critical first step in the ability to predict H₂ flux through a Pd-based membrane). The Ward & Dao model also does not take into account interactions between the adsorbed species or the non-ideal nature of atomic-H dissolution and diffusion through the bulk metal. Moreover, Gielens et al [103] have shown that the same parameters are not applicable for Pd-Ag alloys. Therefore, there is a need to develop an improved micro-kinetic model for H₂ permeation through Pd-based membranes that can then be integrated into reactor-scale models.

Subsequent chapters of this thesis addresses some of the limitations of previous modeling efforts, and establishes a scientific procedure for the determination of parameters of a micro-kinetic model for H adsorption, solution, diffusion, dissolution, and ultimate desorption with Pd-based membranes. Where available, values from first-principles-based studies are used. As an example, these parameters have been calculated for both pure Pd and the Pd_{0.77}Ag_{0.23} alloy. This microkinetic model provides a solid basis for further expansion to include competitive adsorption of other

gases for Pd-alloy membrane design for hydrocarbon reformat purification. This expanded model is combined with porous media transport model (for the porous substrates), and is then used to build a comprehensive reactor model that can be used to assess the performance of any given configuration. The reactor model also has a provision for including the water-gas shift reaction to assess the advantages associated with integrating a WGS catalyst with the reformat stream.

2.6 Objectives of current study

The remnant of this dissertation aims to build and validate a mathematical model to predict the performance of a Pd-alloy based H₂ purifier in the context of a hydrocarbon based PEM fuel cell system. The process of building this model is summarized below:

1. An improved Pd alloy-H₂ interaction is presented. A systematic procedure to estimate the parameters of this model is developed; model parameters are derived for pure Pd and the Pd_{0.77}Ag_{0.23} alloy.
2. Thermochemistry for competitive adsorption of other reformat-gas species (CO & H₂O) on pure Pd membrane surfaces is added to the Pd-H₂ interaction model.
3. A porous media transport model is combined with the Pd-membrane model to form a 1-D “through the membrane” model.
4. The 1-D model is subsequently integrated with channel flow CFD-code to result in a comprehensive “down the channel” membrane purifier model.

This mathematical model is an essential step in the design and optimization of a Pd-membrane based purifier in the PEMFC system context. The design and optimization process is summarized in Figure .

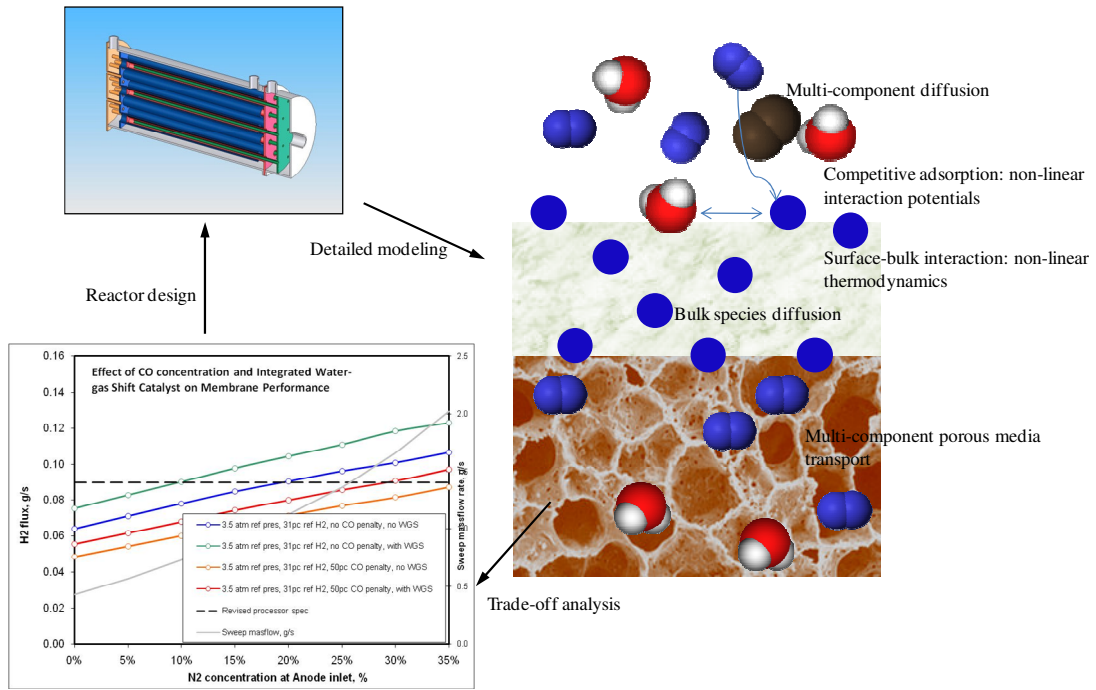


Figure 2.3: Schematic illustration of the objective of building a Pd-membrane based purifier model in the context of a PEM fuel cell system

Chapter 3: Modeling Pd-H₂ and Pd_{0.77}Ag_{0.23}-Pd interactions

3.1 Introduction

Optimizing thin-film Pd/ Pd-alloy membranes for H₂ purification requires detailed understanding of all possible rate-controlling processes including surface adsorption, solution into the bulk metal, bulk diffusion, dissolution, and desorption. H₂ permeation through both Pd and Pd_{0.77}Ag_{0.23} alloy is analyzed by extending diffusion models in the literature with a microkinetic model for surface and bulk reactions between H₂ and the metal. A new procedure is developed to derive values of model parameters from experimental data and first principles studies from literature. For Pd_{0.77}Ag_{0.23}, model results compare extremely well with literature over a broad range of membrane thicknesses (1-20 μm) and operating conditions. The importance of surface processes increase with decreased film thicknesses (below 10 μm) characteristic of recent advances in membrane technology. Previously observed enhancement of H₂ flux after heat treatment in air is explained by increased surface area. Sensitivity of H₂ flux to various thermokinetic parameters provides further insight as to when different processes are rate-controlling. A similar procedure for finding model parameters is implemented for pure Pd, and the corresponding solubility data match very well with literature values over a wide range of temperatures and pressures.

Previous modeling studies in the literature have in general not attempted to match H₂ solubility and diffusion through Pd alloys for a range of membrane thicknesses and

operating conditions. In this chapter, H₂ permeation through both Pd and Pd_{0.77}Ag_{0.23} alloy is analyzed by extending diffusion models in the literature with a microkinetic model for surface and bulk reactions between H₂ and the metal. A new procedure is developed to derive values of model parameters from experimental data and first principles studies from literature. This model provides a solid basis for further expansion to include competitive adsorption of other gases for Pd-alloy membrane design for hydrocarbon reformat purification.

The chapter will first present the governing conservation equations used to model gas-surface, surface-surface, surface-bulk and bulk species interactions. The experimental data and first principles calculations in literature to estimate the thermokinetic parameters in the model are then discussed. The microkinetic model is used for a parametric study and for sensitivity analysis of H₂ flux to key model parameters. In the model description, the term Pd alloy is used both for pure Pd and Pd_{0.77}Ag_{0.23} for simplicity.

3.2 Model description

For the development of the microkinetic model, the modeled system consists of two isolated semi-infinite reservoirs of gas mixtures separated by the Pd alloy membrane. The reservoir with higher $(PX_{H_2})_{feed}$ represents the feed or reformat mixture, and the one with lower $(PX_{H_2})_{perm}$ represents the permeate or sweep mixture. The model is strongly governed by the energetics associated with the different processes: 1) H₂ dissociative adsorption on the reformat side, 2) solution of surface H into the bulk

metal, 3) diffusion of H through the bulk metal, 4) dissolution of H from the bulk metal to the surface, and 5) H₂ formation and desorption on the sweep side.

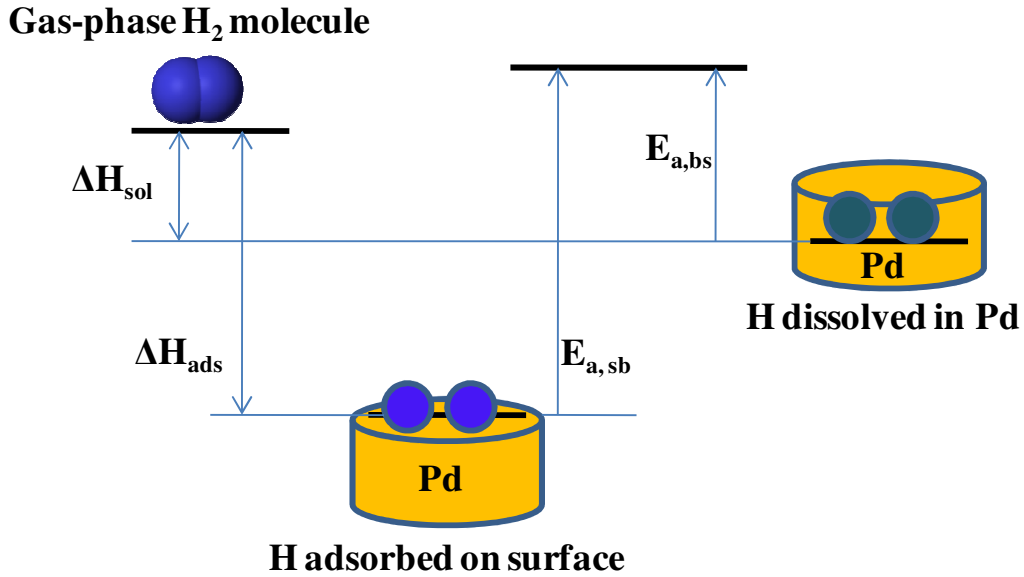


Figure 3.1: Energy levels associated with H in Pd

Figure schematically illustrates energy levels associated with the different hydrogen states: H₂ molecule in the gas-phase, adsorbed H-atom on the Pd alloy surface, and dissolved H-atom in the metallic bulk. Figure also shows the activation energy barriers associated with the transition among these three states. Figure does not show that the energy levels for both the surface and bulk-phase H atoms depend on the surface coverage and bulk mole fractions of H respectively. The interaction potentials associated with the energy levels in these states will be discussed below.

Assuming ideal gas behavior, the gas mixtures are represented by three state variables: pressure P , temperature T , and molar composition X_k . The species

adsorbed onto either of the alloy surfaces are modeled, using a mean field approach, as surface coverages θ_k on a surface with a fixed concentration of total surface sites $\Gamma_{\text{Pd,surf}}$. Each surface species is assumed to occupy one surface site. Since each interstitial site in the disordered Pd alloy can accommodate at most one H-atom, the bulk metal is modeled as a solid phase that consists of a fixed volumetric concentration of interstitial sites $\Gamma_{\text{Pd,bulk}}$. Bulk interstitial sites either contain a dissolved H-atom (represented by mole fraction $X_{\text{H,bulk}}$) or are unoccupied (represented by mole fraction $X_{\text{Pd,bulk}} = 1 - X_{\text{H,bulk}}$). Thus, the thermodynamically important H/Pd (or H/Pd_{0.77}Ag_{0.23}) ratio is numerically equal to $X_{\text{H,bulk}}$, and molar concentration of H can be obtained as $C_{\text{H}} = \Gamma_{\text{Pd,bulk}} X_{\text{H,bulk}}$.

3.2.1 Surface processes

All surface reaction rates are calculated using the Cantera software package [104] according to mass-action kinetics as discussed here. For H₂ adsorption, the forward reaction rate constant is calculated as a sticking coefficient from equation (3.1), which assumes no energy barrier for adsorption and only a sticking probability s^0 with the potential for a power-law dependence on T .

$$k_{\text{ads}} = \left(\frac{s^0 T^{\beta_{\text{ads}}}}{\Gamma_{\text{Pd,surf}}^2} \sqrt{\frac{RT}{2\pi W_k}} \right) \quad (3.1)$$

The H₂ desorption reaction is modeled with Arrhenius rate constants as shown in equation (3.2).

$$k_{\text{des}} = \left(A_{\text{des}} T^{\beta_{\text{des}}} \exp\left(-\frac{E_{\text{a,des}}(\theta_k)}{RT}\right) \right) \quad (3.2)$$

The kinetic model accounts for the effect of surface species interaction potentials on activation energy barriers E_a associated with these reactions, and thus, $E_{\text{a,des}}$ can be linear functions of surface coverages as indicated in equation (3.2).

Equations for calculating the rate constants for surface-bulk interactions are critically modified from Ward & Dao's model [41], as shown in equations (3.3).

$$\begin{aligned} k_{\text{sb}} &= k_{\text{sb},\infty} \exp\left(-\frac{E_{\text{a,sb}}}{RT}\right) \\ k_{\text{bs}} &= k_{\text{bs},\infty} \exp\left(-\frac{E_{\text{a,bs}}}{RT}\right) \times \\ &\exp\left(\frac{\mu_{\text{H}}^{\text{E}}(T, X_{\text{H,bulk}})}{RT}\right) \times \exp\left(\frac{\Delta\mu_{\text{sol}}^0(T) - \Delta\mu_{\text{sol}}^0(T_{\text{ref}})}{RT}\right) \end{aligned} \quad (3.3)$$

The bulk-to-surface reaction rate constant in equation (3.3) is multiplied by a factor to account for the excess free energy $\mu_{\text{H}}^{\text{E}}$ associated with dissolution of H in the metallic bulk, which is significantly negative for both Pd and Pd_{0.77}Ag_{0.23} [91]. The bulk-surface reaction rate constant is also multiplied by another factor to account for changes in the heat of solution with temperature. To calculate the rate of progress of

surface-bulk reactions, the bulk interstitial molar density for surface-bulk reactions is changed from $\Gamma_{\text{Pd,bulk}}$ to $\eta \cdot \Gamma_{\text{Pd,bulk}}$, where η is that fraction of interstitial sites in the Pd-Ag alloy that are preferred locations for the H-atom (for pure Pd, $\eta = 1$).

As can be inferred from Figure , the surface-bulk activation energy $E_{a,\text{sb}}$ and the bulk-surface activation energy $E_{a,\text{bs}}$ are related through the heat of solution ΔH_{sol} and heat of adsorption ΔH_{ads} , as shown in equation (3.4).

$$E_{a,\text{sb}} = |\Delta H_{\text{ads}}| - |\Delta H_{\text{sol}}| + E_{a,\text{bs}} \quad (3.4)$$

The net rate of gas, surface, and bulk phase species production per unit surface area due to surface reactions are obtained by summing the rate of progress over all surface reactions in equation (3.5).

$$\dot{S}_k = \sum_{i=1}^{i_{\text{tot}}} \left(\nu_{ki} \left(k_i \prod_{k=1}^{k_{\text{tot}}} [X_k]^{v_{ki}} \right) \right) \quad (3.5)$$

In this equation, $[X_k]$ represents gas-phase molar concentrations, surface site density, or the modified bulk-phase mole fractions for gas, surface, and bulk phase species respectively.

For surface species, the rate of change of surface coverages θ_k is given by equation (3.6).

$$\Gamma_{\text{Pd,surf}} \frac{d\theta_k}{dt} = \dot{s}_k \quad (3.6)$$

The rate of change of the bulk H mole fraction, $X_{\text{H,bulk}}$, near each surface is determined by the imbalance in surface-bulk reactions and internal H diffusion across the membrane. The resulting conservation equation for the near-surface bulk phase region in equilibrium with the surface (with thickness δ) is shown in equation (3.7).

$$\Gamma_{\text{Pd,bulk}} \delta \frac{dX_{\text{H,bulk}}}{dt} = \varepsilon_{\text{surf}} \dot{s}_{\text{H,bulk}} \mp J_{\text{H,diff}} \quad (3.7)$$

In equation (3.7), \dot{s}_k is multiplied by a surface roughness factor $\varepsilon_{\text{surf}}$ is applied to account for the increased surface roughness per unit area of membrane. $\varepsilon_{\text{surf}}$ is used to account for the increase in surface roughness upon heat treatment of thin membranes observed in experiments such as those conducted by Mejdell et al [45].

$J_{\text{H,diff}}$ is from feed to the permeate side, and hence in equation (3.7), it is subtracted from the surface production rate on the feed side and added to the surface production rate on the permeate side. The thickness of the bulk phase δ , in equilibrium with the surface, wherein surface-bulk reactions impact $X_{\text{H,bulk}}$ was varied from 0.05 to 0.1 μm , but it was found that the value does not affect the steady state results. Hence, $\delta = 0.05 \mu\text{m}$ is chosen and held constant for the results reported in this thesis.

3.2.2 Bulk diffusion

The atomic flux $J_{\text{H,diff}}$ through the membrane is modeled as Fickian diffusion with a proportionality constant D_{H} , as shown in equation (3.8). This is one of the important improvements over Ward & Dao's model: it allows for the activity of H in Pd $a_{\text{H,bulk}}$ to be different from the nominal concentration $C_{\text{H,bulk}}$.

$$\begin{aligned}
 J_{\text{H,diff}} &= -D_{\text{H}} \frac{\partial a_{\text{H}}}{\partial z} \\
 &\approx D_{\text{H}} \frac{(a_{\text{H,bulk}})_{\text{feed}} - (a_{\text{H,bulk}})_{\text{perm}}}{\Delta z} = 2 \cdot J_{\text{H}_2}
 \end{aligned} \tag{3.8}$$

The experimental data used to validate the diffusion model were measured at a sufficiently high temperature so that a linear activity gradient is assumed. Alternatively, the membrane thickness could be discretized into cells, and a finite difference approximation could be applied to calculate the activity gradient at each cell. The activity is further calculated as shown in equation (3.9), where γ_{H} is the activity coefficient for H in Pd alloy.

$$a_{\text{H,bulk}} = \gamma_{\text{H}} C_{\text{H,bulk}} = \gamma_{\text{H}} \Gamma_{\text{Pd,bulk}} X_{\text{H,bulk}} \tag{3.9}$$

γ_{H} is directly calculated from equilibrium solubility data (when gas-phase H_2 is in equilibrium with dissolved H, [92]), by using equation (3.10)). γ_{H} quantifies the curvature of the $(PX_{\text{H}_2})^{1/2}$ vs. $X_{\text{H,bulk}}$ characteristic at a given temperature and

composition; in other words, it captures the deviation from Sievert's law, thereby accounting for the change in activity with H content due to H-H atomic interactions within the Pd metal.

$$\gamma_{\text{H}} = \left\{ \frac{\partial \left(\ln(PX_{\text{H}_2})^{1/2} \right)}{\partial \ln X_{\text{H,bulk}}} \right\}_{\text{eq}} \quad (3.10)$$

The diffusion coefficient D_{H} can be calculated from a concentration independent Arrhenius-type diffusion coefficient as shown in equation (3.11).

$$D_{\text{H}} = D_{\text{H},\infty} \exp\left(-\frac{E_{\text{Diff}}}{RT}\right) \quad (3.11)$$

3.3 Numerical Implementation

For the Pd alloy-H₂ thermochemistry, JANAF polynomial-coefficients are taken for the gas-phase H₂ properties, and similar coefficients for the surface-adsorbed H and the bulk-dissolved H are derived from the gas-phase H₂ numbers and the ΔH and ΔS of gas-surface and gas-bulk global reactions at a reference temperature $T = T_{\text{ref}}$ (estimating these numbers is discussed in the following section). These JANAF polynomial coefficients are used in the Cantera software package [105], which also handles the surface reaction rate calculations at any given temperature as described in equations (3.1), (3.2), (3.3) and (3.5). One set of equations (3.6) and (3.7) for each of the two surfaces of the Pd alloy membrane forms a system of ODEs. The corresponding state-space vector consists of surface coverages on either surface

($\theta_{k,\text{feed}}$ and $\theta_{k,\text{perm}}$) and near-surface bulk H-mole fractions ($X_{\text{H,feed}}$ and $X_{\text{H,perm}}$). The feed and permeate side gases, are treated as semi-infinite reservoirs, and serve as boundary conditions for each run of the model. The MATLAB integration routine *ode15s* is used for this problem because of the stiffness involved.

3.4 Parameter estimation for pure Pd

As will be shown further, matching equilibrium H solubility in the Pd alloy over a wide-range of T and PX_{H_2} is an essential first step toward predicting the flux through a Pd alloy membrane. A systematic method to calculate these parameters will be presented in this section, taking pure Pd as an example.

Since most thermodynamic parameters are energy sensitive, it is convenient to choose a reference temperature at which these will be fixed. Parameter variation with temperature is estimated when possible from reliable literature measurements and first-principle calculations where measurements are not available. For the Pd-H₂ interaction model, this reference temperature T_{ref} is chosen to be 250 °C, since many experimental data from literature are available at that temperature.

$\Delta H_{\text{sol}}(T_{\text{ref}})$ is taken from Flanagan's review [42]. The surface chemistry mechanism is adapted from a previously developed mechanism for H₂ oxidation on metallic Pd nano-particles [106]. As suggested by equation (3.2), the activation energy for H desorption from a Pd surface is given by the previous work as a function of the H-coverage on the surface, as shown in equation (3.12).

$$E_{a,des} = -\Delta H_{ads}^0 + \varepsilon_{H-H}\theta_H \quad (3.12)$$

Here, ΔH_{ads}^0 is the heat of adsorption at zero-coverage. Other surface kinetic parameters s^0 , β_{ads} , A_{des} , β_{des} , $\Gamma_{Pd,surf}$, ΔH_{ads}^0 , and ε_{H-H} are taken from the previous microkinetic model [106], while $\Gamma_{Pd,bulk}$ and $k_{bs,\infty}$ are taken from Ward and Dao [41]. The bulk-surface activation energy $E_{a,bs}$ is assumed to be close to the activation energy for bulk diffusion E_{diff} , which is consistent with the observations of Ward & Dao [41]. $E_{a,bs}$ is then calculated using equation (3.4).

As discussed in the previous section, the excess free energy μ_H^E associated with H in Pd results from the H-H interactions. Since only the dilute α -phase of the Pd-H system is modeled, it is reasonable to assume that these interactions are pair-wise, and hence at a given temperature, μ_H^E is a linear function of concentration X_H . The proportionality constant g_1 is a Gibbs-type function that is mainly dependent on temperature, as shown in equation (3.13). There is no attempt to further separate g_1 into its enthalpic and entropic components h_1 and s_1 ($g_1 = h_1 - Ts_1$) due to lack of sufficient experimental data, and estimating g_1 at a given temperature is sufficient for the purposes of this study.

$$\mu_H^E(T, X_{H,bulk}) \approx g_1(T)X_{H,bulk} \quad (3.13)$$

To estimate g_1 and $k_{sb,\infty}$ at the reference temperature $T_{\text{ref}} = 250 \text{ }^\circ\text{C}$, PX_{H_2} is set equal on both sides of the membrane and varied over a range to calculate the solubility profile. $g_1(T_{\text{ref}})$ and $k_{sb,\infty}$ are varied until the solubility $X_{\text{H,bulk}}$ vs. PX_{H_2} matches with experimental curves in the literature [40, 107], and the results are given in Table 3.1.

Table 3.1: Values for parameters in microkinetic model for pure Pd-H₂ interaction

| <i>Parameter</i> | <i>Value</i> | <i>Units</i> | <i>Reference</i> |
|---|----------------------|---|------------------|
| s^0 | 6.4 | K ^{0.5} | [106] |
| β_{ads} | -0.5 | - | [106] |
| A_{des} | $5.71 \cdot 10^{18}$ | m ² gmol ⁻¹ s ⁻¹ | [106] |
| β_{des} | 0.0 | - | [106] |
| $k_{\text{bs},\infty}$ | $1.03 \cdot 10^{13}$ | s ⁻¹ | this work |
| $k_{\text{sb},\infty}$ | $1.36 \cdot 10^{13}$ | s ⁻¹ | [24] |
| E_{diff} | 22,150 | J gmol ⁻¹ | [24] |
| $E_{\text{a, sb}}$ | 56,000 | J gmol ⁻¹ | this work |
| $\Gamma_{\text{Pd,bulk}}$ | 108,700 | gmol m ⁻³ | [24] |
| $\Gamma_{\text{Pd,surf}}$ | $1.75 \cdot 10^{-8}$ | gmol m ⁻² | [106] |
| g_1 | 21,000 | J gmol ⁻¹ | this work |
| T_{ref} | 523 | K | - |
| $\Delta H_{\text{ads}}(T_{\text{ref}})$ | -42,000 | J gmol ⁻¹ | [106] |
| $\varepsilon_{\text{H-H}}$ | 8,000 | J gmol ⁻¹ | [106] |
| $\Delta H_{\text{sol}}(T_{\text{ref}})$ | -8,000 | J gmol ⁻¹ | [108] |
| $d(\Delta\mu_{\text{sol}}^0)/dT$ | 9.0 | J gmol ⁻¹ K ⁻¹ | this work |
| dg_1/dT | 63.0 | J gmol ⁻¹ K ⁻¹ | this work |
| $D_{\text{H},\infty}$ | $2.9 \cdot 10^{-7}$ | m ² s ⁻¹ | [41] |

The value of $-48.0 \text{ kJ}\cdot\text{mol}\cdot\text{H}^{-1}$ thus obtained for $g_1(T_{\text{ref}})$ agrees well with the previous literature [40]. Fixing $g_1(T_{\text{ref}})$ and $k_{\text{bs},\infty}$, the free energy of the global reaction of H

solution ΔG_{sol}^0 at T_{ref} is calculated, which allows ΔS_{sol}^0 at T_{ref} to be found, and the resulting value of $-51.0 \text{ J}\cdot\text{mol}\cdot\text{H}^{-1}\cdot\text{K}^{-1}$ agrees well with literature values [91]. Values of $\frac{\partial(\Delta\mu_{sol}^0)}{\partial T}$ and $\frac{\partial g_1}{\partial T}$ are adjusted so that the H_2 solubility profile matches with literature data at temperatures $150 \text{ }^\circ\text{C} < T < 427 \text{ }^\circ\text{C}$ [40, 107]. Figure shows these solubility profiles at various temperatures.

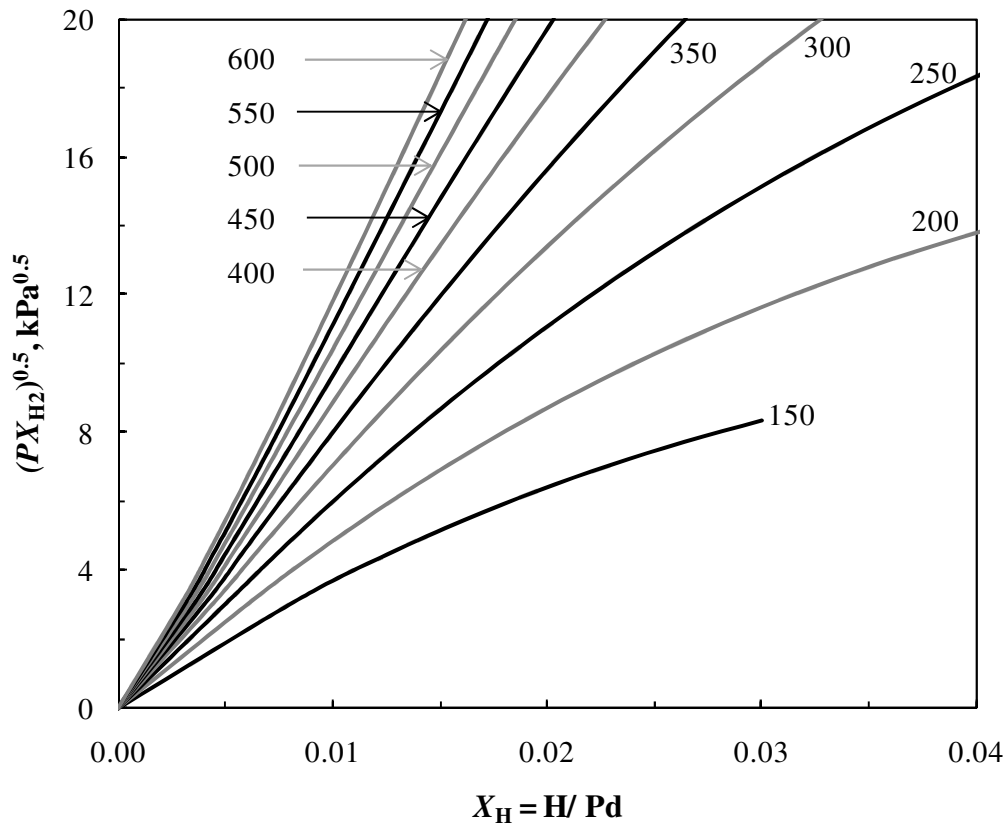


Figure 3.2: Equilibrium solubility profiles of H in Pd at various T (shown in $^\circ\text{C}$ next to each profile)

For each temperature, the thermodynamic activity coefficient

$$\gamma_H = \left\{ \frac{\partial(\ln(PX_{H_2})^{1/2})}{\partial \ln X_{H,bulk}} \right\}_{eq}$$

is calculated as a function of X_H .

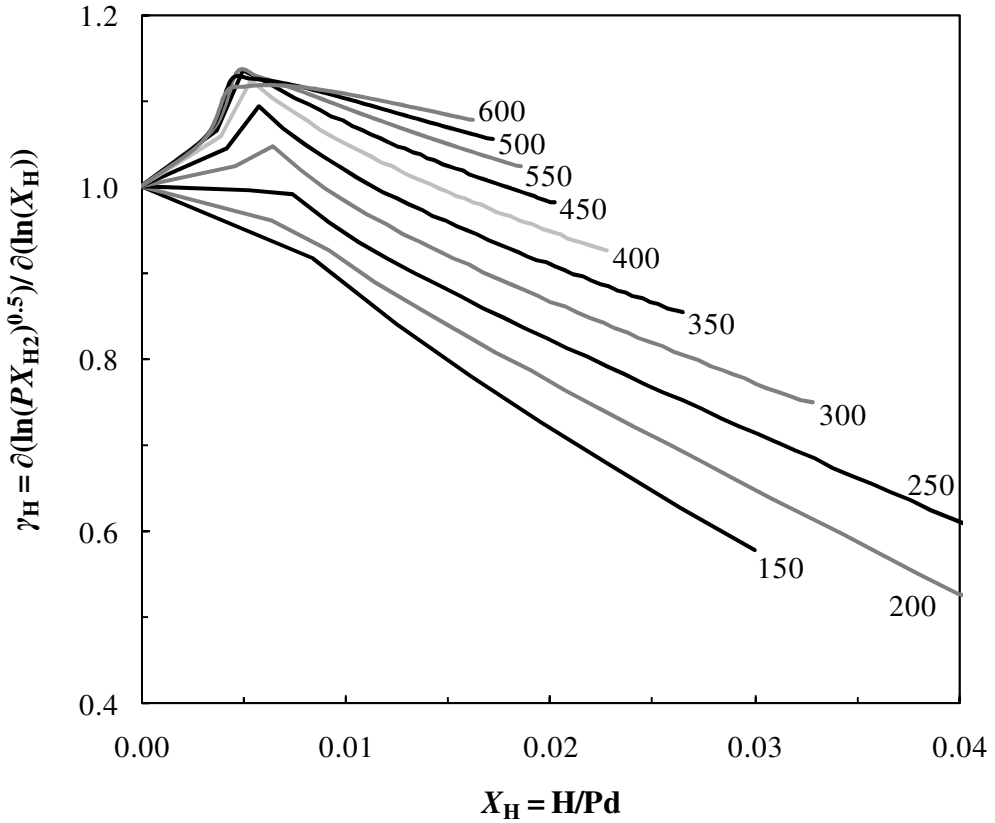


Figure 3.3: γ_H values at various temperatures (shown in °C next to each line)

Plots of γ_H are shown in Figure . In general, these too are in good agreement with literature values [108]. However, the thermodynamic factor has been discussed in literature as being ≤ 1 . Here it is shown that it can attain values >1 at high temperatures and low-H concentrations.

Although there is considerable scatter in the experimental data for H₂ flux through pure Pd membranes [41], the Ward & Dao model values for $D_{H,\infty}$ and E_{diff} gave good agreement in general with results extrapolated from recent high-pressure experiments on thick Pd membranes [109] (Figure), actual experimental values at these pressures are not available from Hara et al. Further validation of values for $D_{H,\infty}$ and E_{diff} are presented in chapter 4. The model is also in good agreement with 1 μm thick free standing membrane experiments by Gielens et al [110] (Figure).

When H₂ permeation is bulk diffusion limited, the relation shown in equation (3.14) holds.

$$E_{\text{a,P}} = \Delta H_{\text{sol}} + E_{\text{diff}} \quad (3.14)$$

There have been experimental studies that have indicated that $|\Delta H_{\text{sol}}|$ and E_{diff} change similarly with temperature, such that their difference $E_{\text{a,P}}$ is approximately constant [111]. Therefore, $dE_{\text{diff}}/dT \approx -d(\Delta H_{\text{sol}})/dT$. ΔH_{sol} has a gradient with temperature of approximately 9.0 J gmol⁻¹ K⁻¹ [40, 111]. The parameters and their values for pure Pd-H₂ interaction model are summarized in Table 3..1.

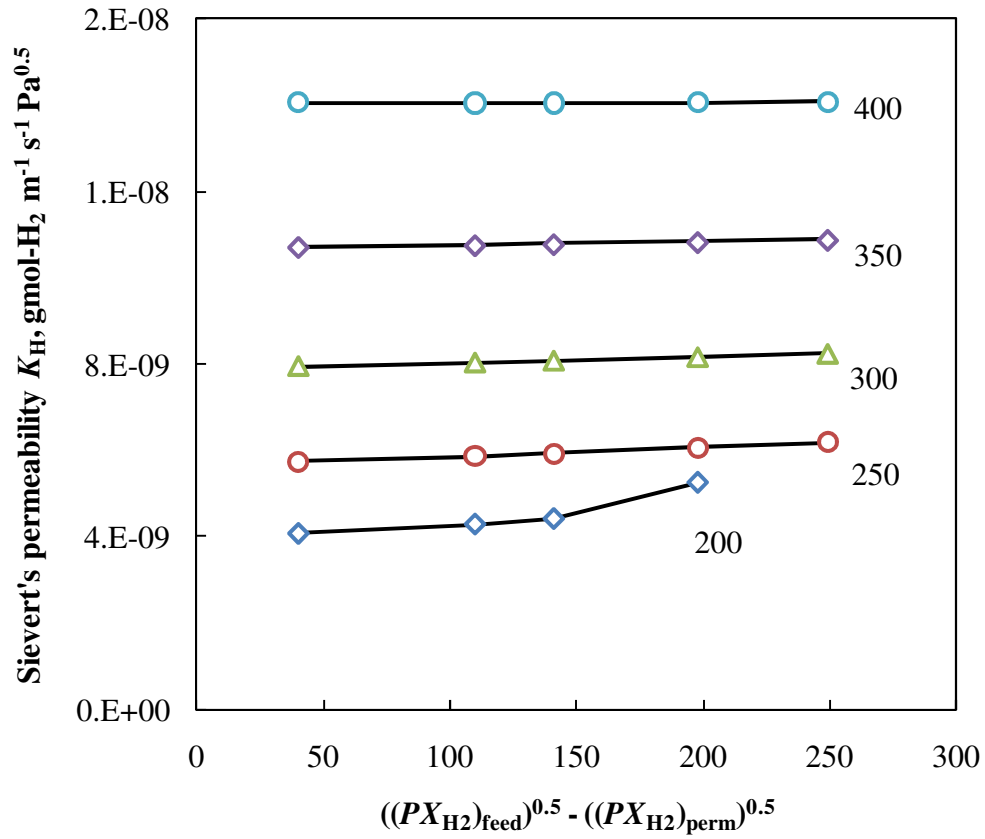


Figure 3.4: Variation of Sievert's permeability constant K_H with feed side H_2 pressure for Pd membranes at various temperatures. $\Delta z_{\text{memb}} = 60 \mu\text{m}$. $(PX_{\text{H}_2})_{\text{perm}} = 0.116 \text{ MPa}$. $(PX_{\text{H}_2})_{\text{feed}}$ is varied as shown.

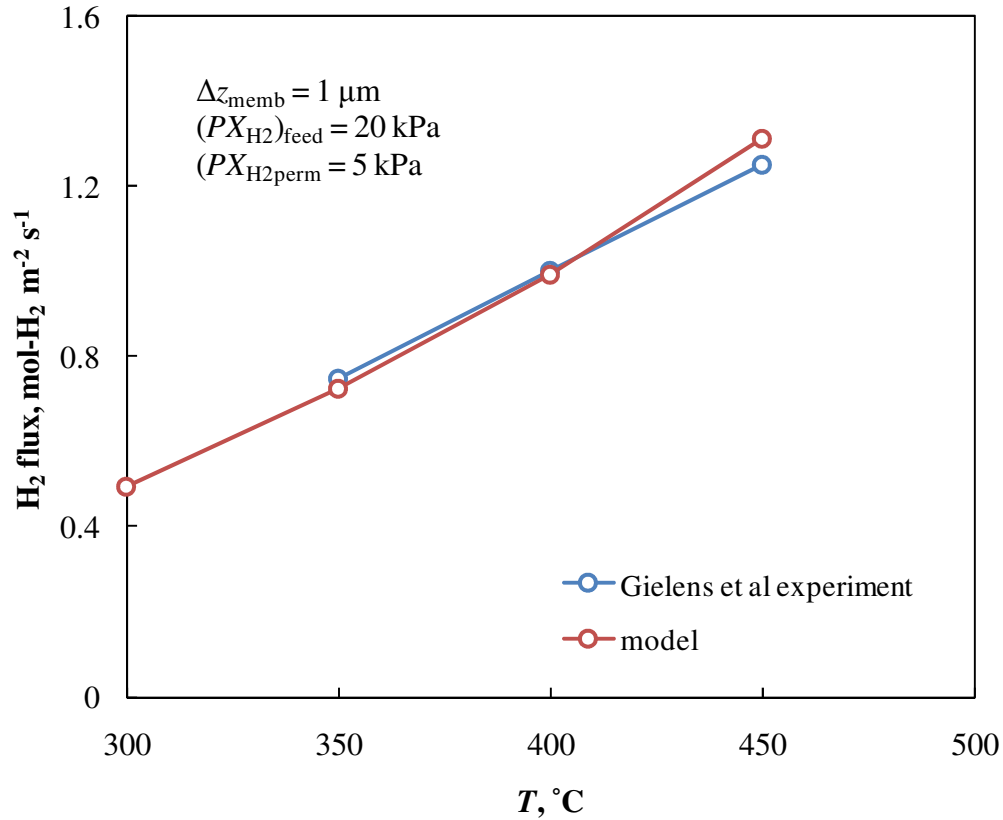


Figure 3.5: Comparison of model results with experiments by Gielens et al [110] on free standing membranes. $\Delta z_{\text{memb}} = 1 \mu\text{m}$ $(PX_{\text{H}_2})_{\text{feed}} = 20 \text{ kPa}$. $(PX_{\text{H}_2})_{\text{perm}} = 5 \text{ kPa}$

Further validation of the H₂ diffusion model will be done in the following chapter, where flux through a composite membrane is measured, and is compared with results from a model that combines this microkinetic model with porous media transport equations. The complete list of parameters and their values are summarized in Table 3.1.

3.5 Parameter estimation for Pd_{0.77}Ag_{0.23}

For H adsorption and solution into the Pd alloy, measurements have been provided in the literature. $\Delta H_{\text{sol}}(T_{\text{ref}})$ for H into Pd_{0.77}Ag_{0.23} is set at $-17.0 \text{ kJ} \cdot \text{molH}^{-1}$ from the

work of Flanagan et al [91]. The smaller of their two estimated values is chosen because it is closer to the corresponding value measured by Picard et al for the Pd_{0.75}Ag_{0.25} alloy at 282 °C [40].

For adsorption enthalpy ΔH_{ads} , it is clear from the first principles study of Lovvik and Olsen that ΔH_{ads} on a Pd_{0.75}Ag_{0.25} surface is lower than the corresponding Pd surface for any of the potential adsorption sites [112]. Since this is the closest in composition in their study to the Pd_{0.77}Ag_{0.23} alloy, ΔH_{ads} for one H atom on a clean surface is reduced from -42.0 to -35.0 kJ molH⁻¹. The same repulsive surface H atom interaction potential was used as for pure Pd [106], which causes ΔH_{ads} to decrease with θ_{H} by $-8.0 \cdot \theta_{\text{H}}$ kJ molH⁻¹. For the H₂ sticking coefficient s^0 , surface site density $\Gamma_{\text{Pd,surf}}$, and the dependence of ΔH_{ads} on θ_{H} are retained from the previous reference for pure Pd [106]. Although clear adsorption rates have not been reported for the alloy, the extent of Pd migration to the surface on the high-pressure side [112] where H₂ adsorption is more rate-controlling suggests that s^0 for pure Pd should provide a good approximation. Furthermore, previous studies suggest that H adsorption has a similar preference of surface sites on Pd/Ag as on Pd [112]. Finally sensitivity studies performed by varying s^0 by as much as 20% indicated no significant effect on the net H₂ flux through the membrane and thus the sticking coefficient from the previous study on pure Pd was used in this study.

Following similar arguments as Ward and Dao [41], the surface-bulk activation energy $E_{\text{a,bs}}$ is set close to the activation energy for bulk diffusion E_{diff} , ~26.0 kJ

molH⁻¹ for this alloy, as discussed subsequently. $E_{a, sb}$ is then obtained from equation (3.4). The exact values of $E_{a, sb}$ and $E_{a, bs}$ are less important than ΔH_{sol} as long as both E 's are within reasonable range of E_{diff} such that the solution or dissolution process does not become a strong kinetic limitation.

The bulk molar density $\Gamma_{Pd, bulk}$ is obtained by multiplying the mass density of the alloy with the known average molar mass. The mass density is estimated by linearly interpolating data from the first principles study of Kart et al [113]. Of the available interstitial sites, the H-atom is known to prefer sites surrounded by either five or six Pd atoms, at least at low temperatures [91]. Assuming a disordered lattice, binomial theorem can be used to calculate η ($= 0.5426$). η effectively reduces the surface-bulk reaction rates and the bulk diffusion coefficient pre-exponential $D_{H, \infty}$ and thus it does not impact the steady-state balance between bulk diffusion and surface-bulk reactions as illustrated by equation (3.7).

The balance between bulk-phase dissolution and permeation is determined largely by the $k_{bs, \infty} / k_{sb, \infty}$ ratio. $k_{sb, \infty}$ is taken from the Ward & Dao [41], and $k_{bs, \infty}$ is estimated as follows. From the work of Flanagan et al [91], an approximation to the excess free energy is applied as shown in equation (3.13). Since H content is relatively low for the operating conditions of this paper, this approximation is assumed to be sufficiently accurate.

$k_{bs,\infty}$ and $g_I(T_{ref})$ are changed to match the solubility profile from Flanagan et al [91] at temperature T_{ref} . The resultant value of $g_I(T_{ref})$ is very close to the experimentally derived value by the same authors, thereby confirming that the entropic effects are captured with sufficient accuracy. Since enthalpic and entropic contributions to g_I ($g_I = h_I - Ts_I$) are difficult to quantify, a linear change with temperature is assumed, and the slope dg_I/dT is estimated based on the change in slopes of ΔH_{sol} with $X_{H,bulk}$ from the work of Picard et al [40]. Similarly, a linear change with temperature is assumed for μ_{sol}^0 , and $d\mu_{sol}^0/dT$ is estimated by trial and error so that the solubility matches those measured by the same authors at two additional temperature points, 282 and 427 °C. Although experimental data suggests that ΔH_{sol} has a larger rate of change with respect to temperature, $d\Delta H_{sol}/dT$ is assumed to be the significant contribution to $d\mu_{sol}^0/dT$. Figure shows that the model results compare well with experimental solubility data.

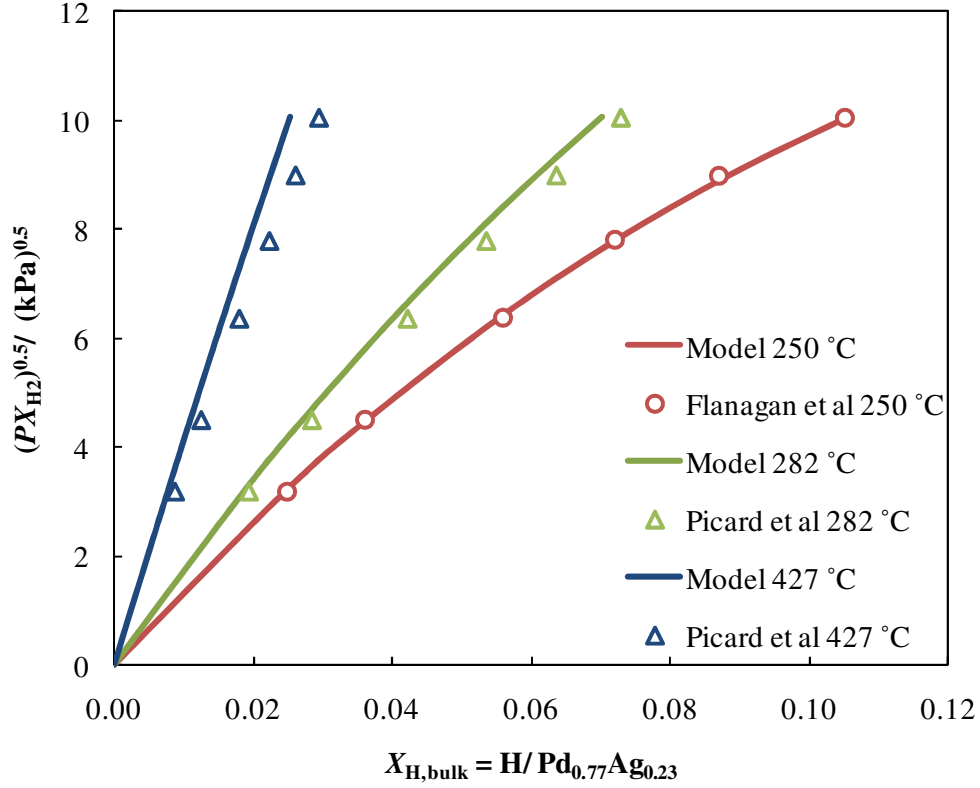


Figure 3.6: Solubility of H in Pd_{0.77}Ag_{0.23}: model results match with experimental values from literature

Solubility plots are constructed for temperatures from 250-600 °C, using the above

solubility model. For each temperature, the slope $\gamma_H = \left\{ \frac{\partial(\ln(PX_{H_2})^{1/2})}{\partial \ln X_{H,bulk}} \right\}_{eq}$ is found to

be relatively constant for $PX_{H_2} \leq 120$ kPa. Such a low pressure regime is reasonable for fuel reformat streams used in PEMFC applications. Hence, unlike pure Pd where γ_H can be as low as 0.6, γ_H for H in Pd_{0.77}Ag_{0.23} is modeled as depending only on T and its value is interpolated from data points generated as described above and provided in Table 3.2.

Table 3.2: Calculated values of γ_{H} for H in Pd_{0.77}Ag_{0.23}

| T ($^{\circ}\text{C}$) | γ_{H} |
|----------------------------|---------------------|
| 250 | 0.7940 |
| 282 | 0.8703 |
| 300 | 0.8959 |
| 350 | 0.9407 |
| 400 | 0.9618 |
| 427 | 0.9680 |
| 500 | 0.9849 |
| 550 | 0.9888 |
| 600 | 0.9907 |

The next important step is estimation of the activation energy for bulk diffusion E_{diff} . Unemoto et al have published experimental data on 20 μm thick Pd_{0.77}Ag_{0.23} membranes at 500 and 600 $^{\circ}\text{C}$ [87]. For these relatively thick membranes, H₂ permeation was bulk-diffusion limited, and reformat and sweep gases were in equilibrium with the near-surface bulk on each side. The apparent activation energy for permeation $E_{\text{a,p}}$, is calculated from the Arrhenius equation to be about 9.0 kJ molH⁻¹. Following similar arguments as in pure Pd, equation (3.14) is assumed to be valid with a near-constant $E_{\text{a,p}}$, giving $E_{\text{diff}}(T_{\text{ref}}) = 26.0 \text{ kJ} \cdot \text{molH}^{-1}$, and $dE_{\text{diff}}/dT \approx -d(\Delta H_{\text{sol}})/dT = 3.0 \text{ J gmol}^{-1} \text{ K}^{-1}$.

The diffusion coefficient pre-exponential $D_{\text{H},\infty}$ that fits the above data from Unemoto et al best is estimated to be about $4.0 \cdot 10^{-7} \text{ m}^2 \text{ s}^{-1}$ (Figure).

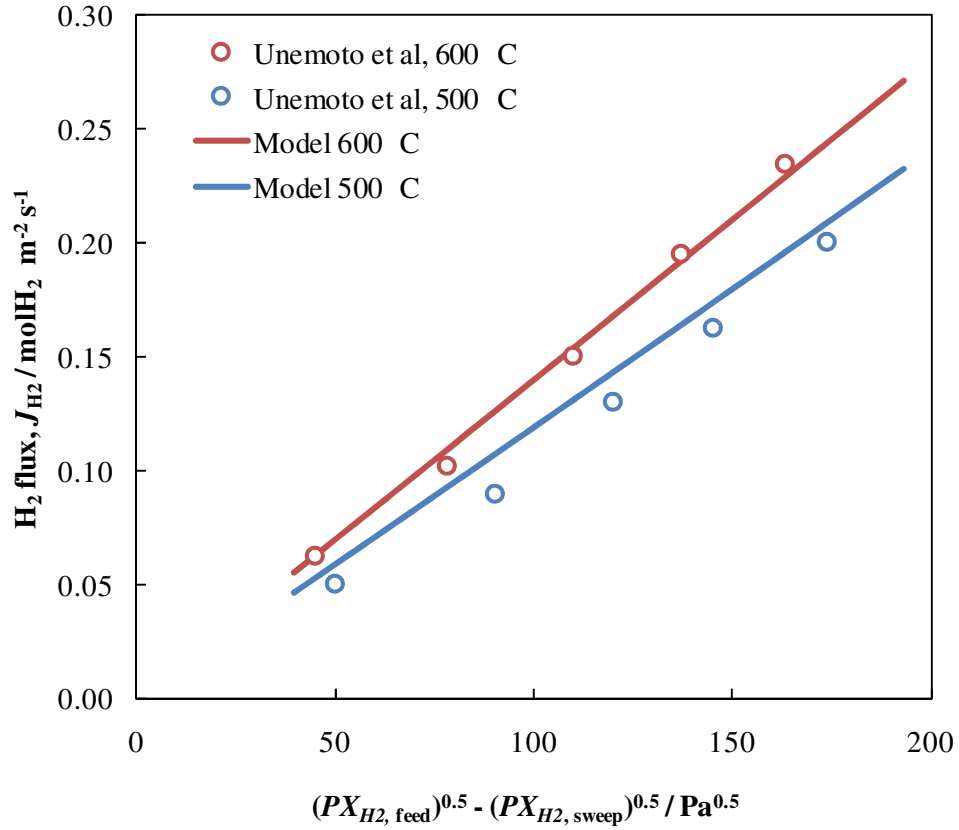


Figure 3.7: High temperature H₂ permeance model predictions for thick Pd_{0.77}Ag_{0.23} membranes compare well with experiments ([87]).

Both $E_{\text{diff}}(T_{\text{ref}})$ and $D_{\text{H},\infty}$ are in close agreement with experimental values obtained by Wang et al [92]. This concludes the estimation of parameters for the H₂-Pd_{0.77}Ag_{0.23} model, which is summarized in Table 3.3.

Comparing parameters for pure Pd and the Pd-Ag alloy, it can be seen that the Pd-Ag alloy has a higher heat of solution ΔH_{sol} than the pure metal. The activation energy for desorption from the surface E_{des} is low, which results in a lower activation energy for transition to bulk $E_{\text{s,b}}$. Finally, the H-H interactions (g_1) are not so strong in the

alloy, thereby resulting in lower γ_{H} values. The above three factors are the main reasons for the alloy being more permeable to H_2 than the pure metal.

Table 3.3: Parameter values in microkinetic model for $\text{H}_2\text{-Pd}_{0.77}\text{Ag}_{0.23}$ interaction

| <i>Parameter</i> | <i>Value</i> | <i>Units</i> | <i>Reference</i> |
|---|--------------------------------|---|------------------|
| s^0 | 6.4 | $\text{K}^{0.5}$ | [41] |
| β_{ads} | -0.5 | - | [41] |
| A_{des} | $5.71 \cdot 10^{21}$ | $\text{m}^2 \text{ kmol}^{-1} \text{ s}^{-1}$ | [41] |
| β_{des} | 0.0 | - | [41] |
| $k_{\text{bs},\infty}$ | $4.2 \cdot 10^{13}$ | s^{-1} | this work |
| $k_{\text{sb},\infty}$ | $1.36 \cdot 10^{13}$ | s^{-1} | [29] |
| E_{bs} | 26.0 | kJ gmol^{-1} | This work |
| E_{diff} | 26.0 | J kmol^{-1} | This work |
| E_{sb} | 44.0 | kJ gmol^{-1} | This work |
| $\Gamma_{\text{Pd,bulk}}$ | 108.7 | kmol m^{-3} | [45] |
| $\Gamma_{\text{Pd,surf}}$ | $1.75 \cdot 10^{-8}$ | kmol m^{-2} | [41] |
| η | 0.5426 | - | This work |
| g_l | 21.0 | kJ gmol^{-1} | This work |
| T_{ref} | 523 | K | - |
| $\Delta H_{\text{ads}}(T_{\text{ref}})$ | $-35.0 + 8.0\theta_{\text{H}}$ | kJ gmol^{-1} | [41] |
| $\Delta H_{\text{sol}}(T_{\text{ref}})$ | -17.0 | kJ gmol^{-1} | [46] |
| $d(\Delta\mu_{\text{sol}}^0)/dT$ | 3.0 | $\text{J gmol}^{-1} \text{ K}^{-1}$ | This work |
| dg_1/dT | 16.7 | $\text{J gmol}^{-1} \text{ K}^{-1}$ | This work |
| $D_{\text{H},\infty}$ | $4.0 \cdot 10^{-7}$ | $\text{m}^2 \text{ s}^{-1}$ | This work |

3.6 Model Results for $\text{H}_2\text{-Pd}_{0.77}\text{Ag}_{0.23}$

As discussed in the previous section, experiments on thick membranes by Unemoto et al, where H_2 flux is bulk diffusion limited, were used to derive key parameters for the model. The model is now compared against experiments by Mejdell et al, which are

done using thin free-standing $\text{Pd}_{0.77}\text{Ag}_{0.23}$ membranes [45]. These membranes show significant improvement in H_2 flux at $300\text{ }^\circ\text{C}$ after heat treatment in air at $400\text{ }^\circ\text{C}$. The magnitude of improvement depended on membrane thickness, and has been largely attributed to a 3-4X improvement in surface area. Therefore, for the heat-treated films, the model is modified by setting $\varepsilon_{\text{surf}} = 4.0$, and the results give excellent agreement with experimental data after heat treatment over a range of membrane thicknesses as illustrated in Figure 3.8.

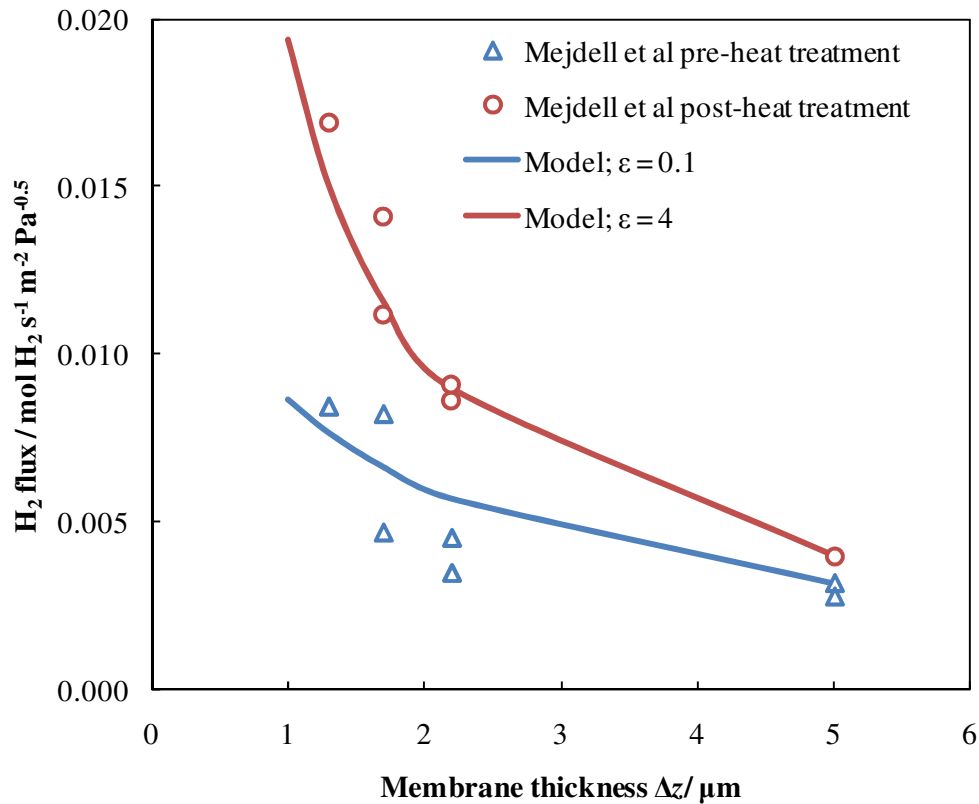


Figure 3.8: Comparison of model results with experimental data by Mejdell et al [45]. $T = 300\text{ }^\circ\text{C}$. Feed side is pure H_2 at 120 kPa, and sweep side is pure H_2 at 100 kPa.

While K_H , permeability based on Sievert's law, is relatively constant at $\approx 2.0 \cdot 10^{-8}$ $\text{gmol-H}_2 \text{ m}^{-1} \text{ s}^{-1} \text{ Pa}^{-0.5}$ for membrane thicknesses from 1-5 μm , it is important to note that this value is substantially greater than from that obtained by assuming Sievert's law and extrapolating (with an Arrhenius expression) the experimental data of Unemoto et al [46, 87]. Their measured values of $2.37 \cdot 10^{-8}$ and $2.80 \cdot 10^{-8}$ $\text{gmol-H}_2 \text{ m}^{-1} \text{ s}^{-1} \text{ Pa}^{-0.5}$ at 500 and 600 $^\circ\text{C}$ respectively extrapolates using an Arrhenius expression for K_H back to $1.43 \cdot 10^{-8}$ $\text{gmol-H}_2 \text{ m}^{-1} \text{ s}^{-1} \text{ Pa}^{-0.5}$ at 300 $^\circ\text{C}$. Changing ϵ_{surf} does not result in any significant change to these values. As such, this result demonstrates the importance of the non-linear nature of H_2 solubility and H diffusion in calculating H_2 flux, especially through thin membranes at low temperatures.

The pre- and post-heat treatment results from Mejdell et al [45] clearly indicate that surface processes play a critical role in limiting H_2 flux prior to heat treatment. However, when using a nominal value of $\epsilon_{surf} = 1.0$ for the pre-heat treatment data, model results do not match very well with experimental data. A fitted K_H for this data is substantially lower than the expected Sievert's law value of $1.43 \cdot 10^{-8}$ $\text{gmol-H}_2 \text{ m}^{-1} \text{ s}^{-1} \text{ Pa}^{-0.5}$ at 300 $^\circ\text{C}$. The low K_H suggests that other factors are at play in these experiments. One possible explanation is contamination of the surface by species during the manufacturing process. Contamination can cause a simultaneous reduction in k_{sb}^0 and k_{bs}^0 due to a loss in available sites for adsorption. Surface contamination can also explain the large variation within membrane samples of similar thicknesses. A ϵ_{surf} value of 0.1 gave results that tracked the mean of the pre-heat treatment (Figure). Such a low ϵ_{surf} suggests substantial surface contamination existed prior to heat

treatment, and although this is somewhat speculative, the model does track very nicely the non-linear increase of the flux with decreasing membrane thickness.

After validating the model against experimental data, some parametric studies were performed over a range of operating conditions and membrane thicknesses, and results are summarized in Figure -Figure . As membrane thickness increases from 1 to 10 μm , the importance of bulk-phase diffusion over and against surface reactions rises. This is shown in the temperature variation of H_2 flux for the different membrane thicknesses – 1, 5, and 10 μm in these figures.

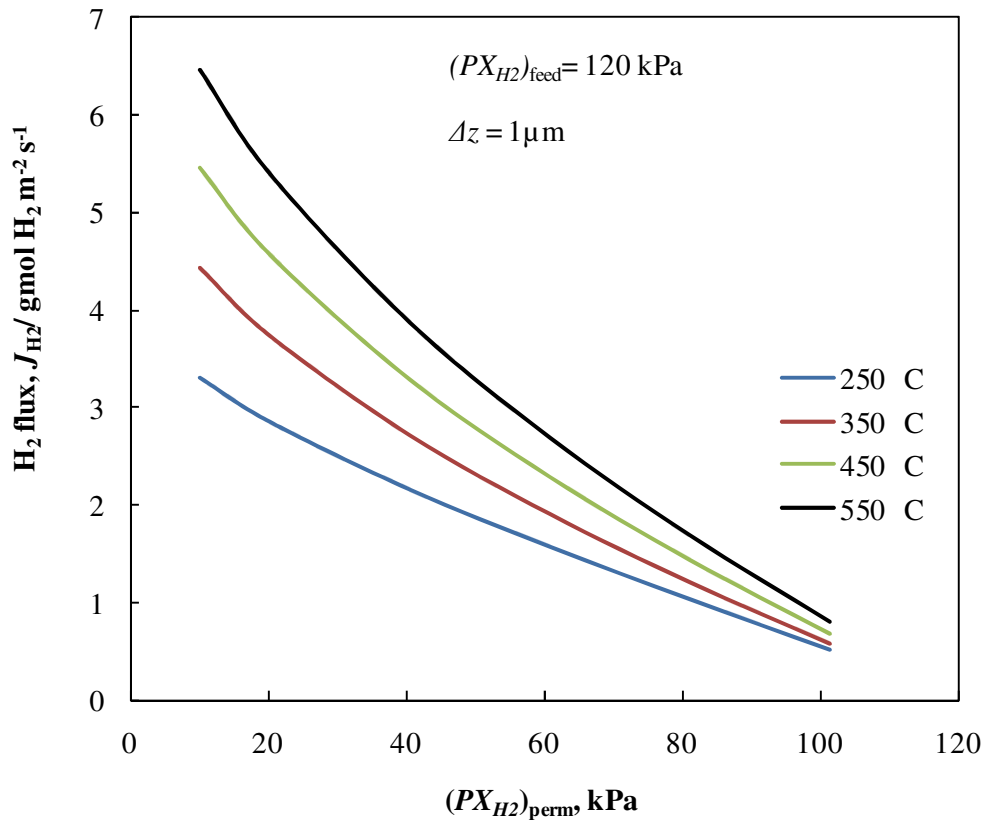


Figure 3.9: H_2 flux through a 1 μm thick $\text{Pd}_{0.77}\text{Ag}_{0.23}$ membrane at $250 < T < 550$ $^\circ\text{C}$, when the feed side is maintained at 120 kPa.

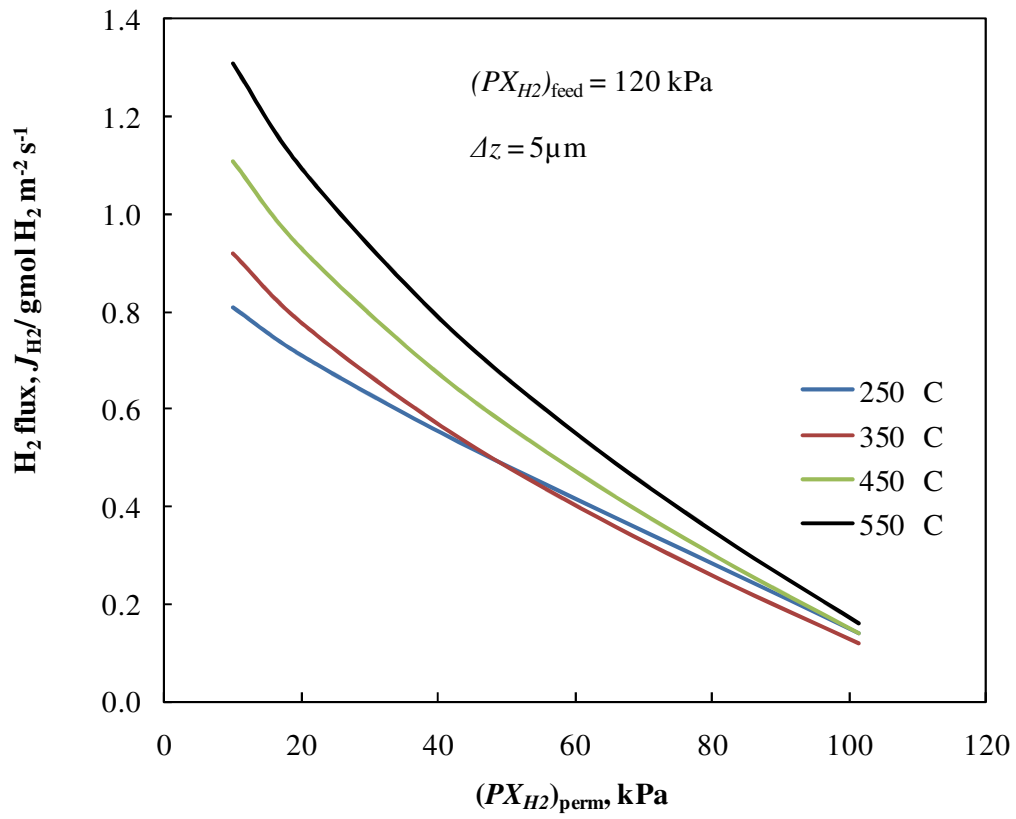


Figure 3.10: H_2 flux through a $5 \mu\text{m}$ thick $\text{Pd}_{0.77}\text{Ag}_{0.23}$ membrane at $250 < T < 550$ °C, when the feed side is maintained at 120 kPa

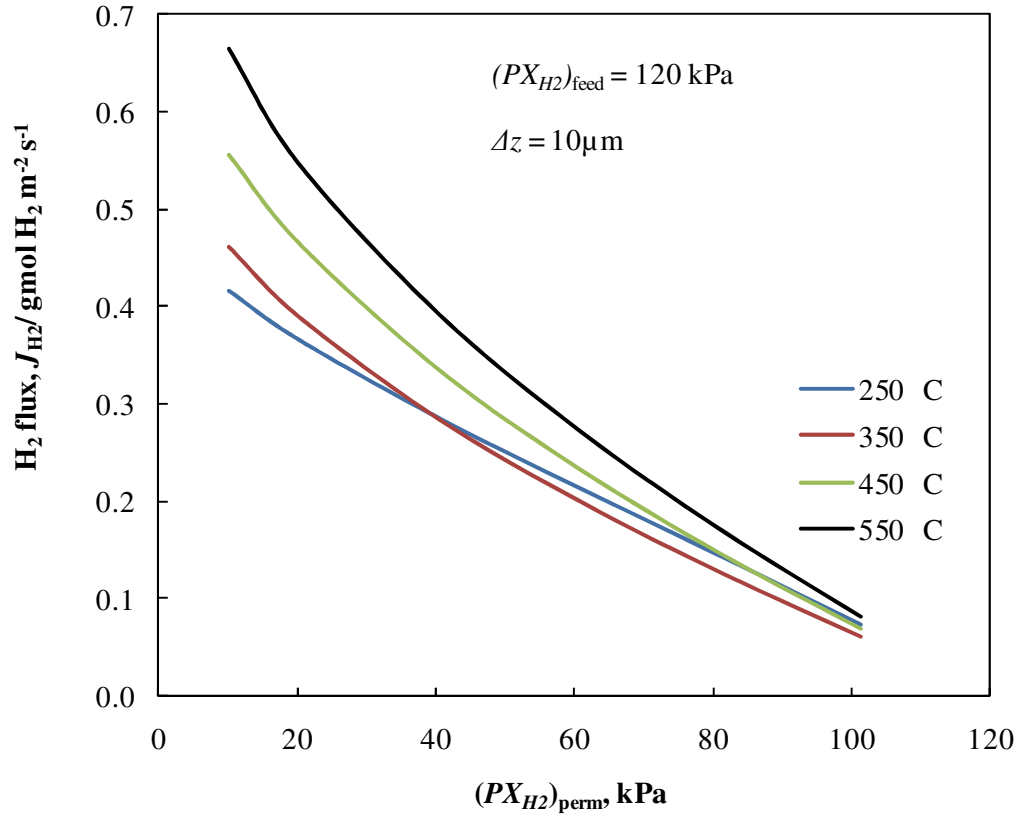


Figure 3.11: H₂ flux through a 10 μm thick Pd_{0.77}Ag_{0.23} membrane at 250 < T < 550 °C, when the feed side is maintained at 120 kPa

For the thinner 1 μm membrane results (Figure), high flux rates are primarily controlled by the adsorption and desorption reactions on the feed and the permeate side respectively. Both rates increase with T and thus there is a monotonic increase in flux with T . However for the thicker 5 μm membrane (Figure), bulk diffusion becomes more important in determining the H₂ fluxes. This results in non-monotonic dependence of the flux with temperature at lower temperatures. This is because the decrease in H solubility with increasing temperature lowers the $X_{H,bulk}$ gradient competes against the increase in bulk diffusivity D_H as indicated in equation (3.11) and (3.7). This results in higher fluxes predicted for 250 °C than 350 °C at higher

$(PX_{H_2})_{perm}$ where the gradient in $X_{H,bulk}$ in the membrane becomes critical. This effect grows even more significant for the thicker 10 μm membrane (Figure). For this thickness, the H_2 flux is even more strongly controlled by bulk diffusion, and the higher solubility at 250 °C results in even stronger non-monotonic fluxes with T at the higher $(PX_{H_2})_{perm}$. This non-monotonic flux behavior with T for thick membranes was also experimentally observed by other authors [92].

The results in Figure -Figure show that for these range of conditions a constant K_H for each T does not capture the behavior for the range of $(PX_{H_2})_{perm}$ particularly for the lower T . This is illustrated by observing the different shapes in the curves for 250 °C vs. the higher T conditions. This non-ideal behavior is in part due to the dependence of ΔH_{sol} on $X_{H,bulk}$ and the relatively high $X_{H,bulk}$ at the lower T .

The same data is used to derive an effective Sievert's law coefficient K_H by fitting the flux data to equation (2.1) for a range of T and membrane thicknesses. The effective K_H is found by varying $(PX_{H_2})_{perm}$ for a fixed $(PX_{H_2})_{feed}$. Figure shows data sets for $(PX_{H_2})_{feed}$ fixed at 120 kPa and 70 kPa respectively. Ideally, K_H would be independent of $(PX_{H_2})_{feed}$. However at low temperatures, the non-linear H solubility results in a variation in the bulk-phase driving force that increases faster than $(PX_{H_2})^{1/2}$. Hence, the fitted K_H rises with $(PX_{H_2})_{feed}$ as shown in the figure. Data at higher temperatures provide a better fit to equation (2.1), and at these temperatures, the effective K_H does not depend on membrane thicknesses or $(PX_{H_2})_{feed}$, as to be expected. It is also important to note that at lower temperatures, K_H values vary

significantly with membrane thickness, and this variation is higher at $(PX_{H_2})_{\text{feed}}$. In general, the individual fits for K_H were relatively poor at these low temperatures, indicating stronger effects of non-ideal effects at these conditions. This analysis further underscores the fact that the utility of Sievert's law approximations is limited in typical fuel cell system conditions.

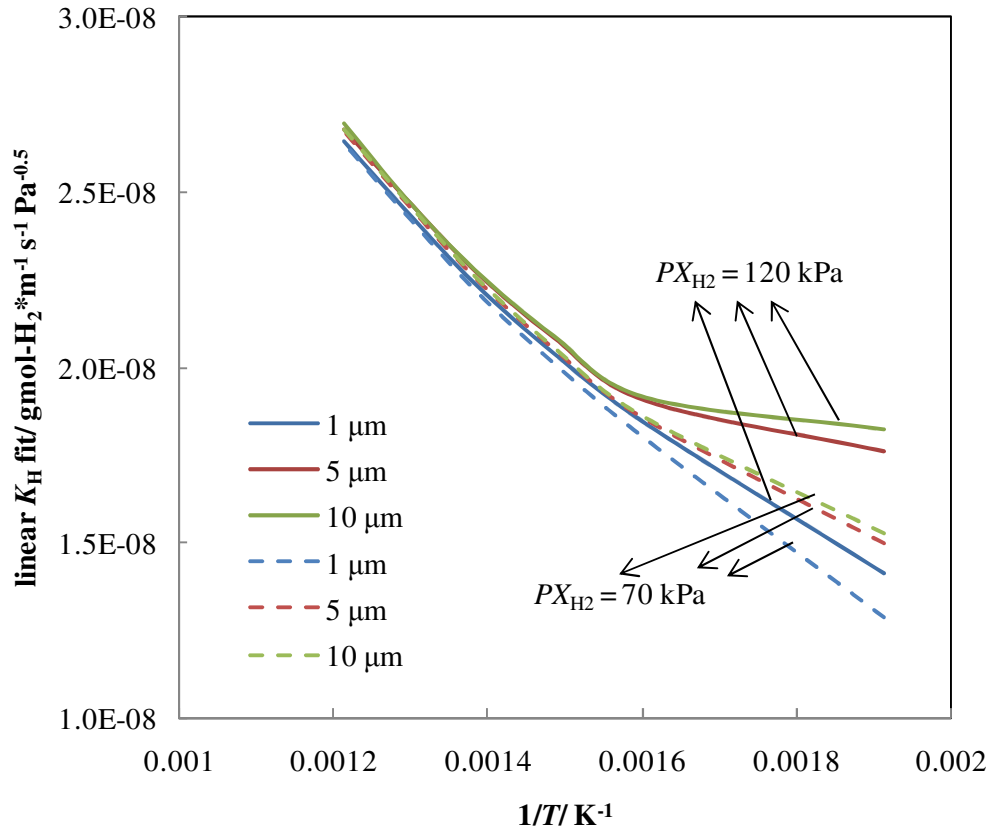


Figure 3.12: Model results: variation of linear-fit Sievert's law coefficient K_H with temperature and membrane thickness. Feed side is at 120 kPa, and sweep side is varied between 10 and 100 kPa (both sides are pure H_2).

To further understand the importance of different parameters on the H_2 flux predictions, the sensitivity of the H_2 flux to key model parameters are calculated. The parameters are varied by 0.1%, and relative change in J_{H_2} is found. The bars in the

graph are the ratios of the relative changes in J_{H_2} to the relative parameter change ($\frac{\delta J_{H_2}/J_{H_2}}{\delta p/p}$ where p is the parameter under study). Typical operating conditions are chosen ($\Delta z = 5 \mu\text{m}$, $(PX_{H_2})_{\text{feed}} = 120 \text{ kPa}$, $(PX_{H_2})_{\text{perm}} = 50 \text{ kPa}$, $T = 400 \text{ }^\circ\text{C}$). It can be seen from Figure 3.13 that the model is sensitive to $\Delta H_{\text{ads}}(T_{\text{ref}})$, $\Delta H_{\text{sol}}(T_{\text{ref}})$ and $E_{\text{diff}}(T_{\text{ref}})$. However, the excess free energy g_I is expected to have a larger influence at lower T . It is also important to note that a reduction in the surface adsorption energy, as would occur if other species such as CO compete with H for surface sites and electrons from the alloy bulk, has a potential to reduce the H_2 flux significantly.

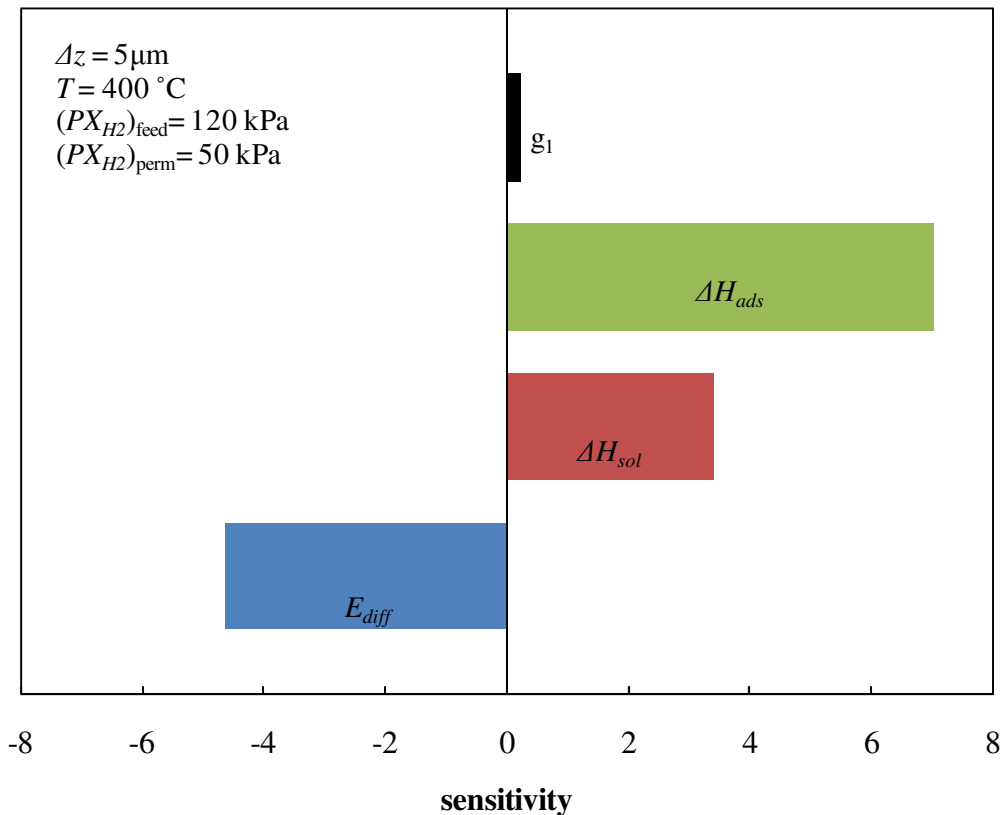


Figure 3.13: Model results: sensitivity of H_2 flux at typical conditions to key parameters.

For example, an uncertainty of $0.5 \text{ kJ}\cdot\text{mol}^{-1}$ in the experimental value of ΔH_{ads} results in an uncertainty in J_{H_2} of $\sim 0.1 \text{ mol}\cdot\text{m}^{-2}\cdot\text{s}^{-1}$ at a nominal J_{H_2} value of $1 \text{ mol}\cdot\text{m}^{-2}\cdot\text{s}^{-1}$. Although values of the above parameters are different for pure Pd, the sensitivity of H_2 flux to each of these parameters is expected to show similar trends as for $\text{Pd}_{0.77}\text{Ag}_{0.23}$.

3.7 Summary

This chapter provides a thermokinetic basis for further model development and design of Pd alloy membranes for H_2 membrane purifiers in PEMFC applications. A microkinetic model for H adsorption, solution, diffusion, dissolution, and desorption with Pd-based membranes has been presented, and parameters for this model have been calculated for both pure Pd and $\text{Pd}_{0.77}\text{Ag}_{0.23}$ membranes. Experimental data from multiple studies and first principles DFT calculations from previous references have been used to estimate the thermokinetic parameters critical for modeling the surface and bulk processes in the membrane. Parametric studies using the model have been presented for the $\text{Pd}_{0.77}\text{Ag}_{0.23}$ alloy membrane, and key parameters have been identified for sensitivity. This microkinetic model provides a solid basis for further expansion to include competitive adsorption of other gases and porous media transport equations.

The models predict H_2 solubility and permeance with reasonable accuracy across a broad range of membrane thicknesses and operating conditions. It has been

demonstrated that a critical step in predicting the H₂ flux involves predicting H₂ solubility in the alloy. To this end, this model represents many improvements over previous modeling efforts, including the use of non-ideal thermodynamics. The importance of surface processes in thin membranes has also been established, with help from literature data. This chapter also highlights the non-linear behavior of the total flux with respect to $(PX_{H_2})_{perm}$, and provides a valuable design tool for going beyond past studies using Sievert's law to develop optimized membranes for PEMFC applications.

Chapter 4: Pd-composite membranes

4.1 Introduction

Porous matrices are often used to provide structural support to thin Pd-based metallic membranes in H₂ separation applications. Optimizing such composite membranes requires detailed understanding of all possible rate-controlling processes including surface and bulk processes in the metal and diffusion of gases through the porous media. In the work described in this chapter, a composite membrane is fabricated by depositing a thin (~5-6 μm) Pd film on a porous α-Al₂O₃ tube and H₂ permeance of this composite membrane is measured over a range of operating conditions. The rate-controlling processes for the H₂ permeation are evaluated with a computational model that combines the detailed thermo-kinetic Pd-H₂ interaction model developed and validated in the previous chapter with a porous media transport model. The porous media transport model is independently calibrated using experimental measurements. The combined composite membrane model gives good agreement with experiments over a large range of temperatures (250-450 °C) and H₂ partial pressures (100-385 kPa). This validated model is then used to analyze the importance of design parameters such as Pd thickness and support micro-structure on H₂ flux through the membrane. These parametric studies will also aid in assessing trade-offs between membrane structural robustness and overall performance.

Advances in plating techniques have created the potential for very thin defect-free Pd-based metallic membranes to be commercially employed in such applications. The

large cross-membrane differential pressures that must be maintained to increase permeance and thereby reduce required membrane area require adequately robust mechanical supports (or substrates) for maintaining structural integrity. Materials such as porous α -Al₂O₃ [49, 58, 59], porous YSZ [59], or porous stainless steel (PSS) [60, 61] are most commonly used for this purpose. As discussed in chapter 2, the bulk porous support is usually coated with a thin nano-porous layer to minimize Pd from interacting with the stainless steel. This thin intermediate layer could either be made of ceramic, or oxide of the stainless steel itself. One of the recent studies speculates that Pd-Al interactions may influence Pd membrane permeance due to detrimental Pd-Al reactions [59]. Differences in supported membrane fluxes may also be attributed to how the dense Pd membrane interfaces with porous substrates and how that interaction adds to the resistance of H₂-transport through the supported composite membrane. Whereas in case of thicker membranes (>20 μ m), this substrate resistance can be largely ignored, it becomes significant as the thickness and thus resistance of the metallic membrane is reduced with thinner (< 10 μ m) Pd-alloy membranes derived from improved coating technologies. The rough porous substrates also influence membrane surface morphology and thus the thickness and quality of the Pd layer itself [84]. Optimizing such composite membranes is important for the effectiveness, response time and cost considerations in a typical PEMFC system.

Many recent experimental studies have demonstrated the significance of the support-layer resistance [35, 52, 56, 60, 61, 83, 84, 93-101]. Some of these studies were

carried out with thicker ($> 20 \mu\text{m}$) Pd films such that the support layer resistance was not a significant contribution. However, many of these studies with both thicker and thinner Pd membranes attempted to fit experimental data to a modified Sievert's law equation by varying the pressure exponent n between 0.5 and 1.0 as shown in equation (2.1) (page 34).

In equation (2.1), when $n = 0.5$, it becomes Sievert's law and K_H is referred to as Sievert's constant. The $n = 0.5$ condition implies that the hydrogen transport through a particular membrane configuration is dominated by the H-atom diffusion through the metallic membrane. On the other hand, when $n > 0.5$, it implies that other processes have some role in limiting the hydrogen transport, but the particular underlying physics are masked by the empirical fit. For thinner films where the porous media transport can be an important rate-limiting process, equation (2.1) is unlikely to be applicable over a large range of temperatures or operating pressures. Recent modeling studies by Iwuchukwu and Sheth [114] and Caravella et al. [102] have addressed this issue by adding porous media transport considerations to the H_2 -Pd interaction model proposed by Ward & Dao [41]. However, these modeling studies did not validate their H_2 -Pd interaction models, especially the associated non-ideal thermodynamics [111, 115]. Also, these recent studies of composite membranes have not presented a clear validation of the model against experiments. The models assume that hydrogen-transport resistances due to the metallic membrane and the porous substrate are additive, and that there is little interaction between the two.

In this chapter, the H₂-Pd interaction model presented in the previous chapter is combined with a porous media transport model. Flow resistance of the bare (non Pd-coated) ceramic substrate is measured to estimate parameters for the porous media transport model. These independently validated models are then combined into a composite membrane model, which is in turn validated with experiments on a 5-6 μm thick Pd membrane supported on a porous α-Al₂O₃ tube. This validated model provides key insight into rate-limiting processes and the significance of metal-ceramic interface on membrane performance.

4.2 Porous media transport model

4.2.1 Model equations

To model transport in the porous support, the gas is assumed to be ideal with state variables temperature T , pressure P and mass fractions Y_k . The isothermal species conservation equation for the porous media is shown in equation (4.1) in terms of species mass fractions Y_k and density ρ :

$$\frac{\partial(\phi_g \rho Y_k)}{\partial t} + \frac{\partial j_k}{\partial r} = 0 \quad (4.1)$$

j_k is the mass flux through the porous media must be found for H₂ and diluent gases. Summing equation (4.1) over all those species provides total mass conservation. To calculate j_k , the dusty-gas model (DGM) is implemented to model the multi-component gas transport in porous media [116, 117]. For the tubular geometry of

interest in the current study, the DGM model can be expressed as an implicit relationship among molar concentration $[X_k]$, molar flux $J_k = j_k/W_k$, and radial concentration and pressure gradients as shown in equation (4.2).

$$\sum_{l \neq k} \left(\frac{[X_l]J_k - [X_k]J_l}{(PD_{kl}^e/\overline{RT})} \right) + \frac{J_k}{D_{k,Kn}^e} = -\frac{1}{\tau_g} \frac{\partial [X_k]}{\partial r} - \frac{[X_k]B_g}{D_{k,Kn}^e \mu_g} \cdot \frac{1}{\tau_g} \frac{\partial P}{\partial r} \quad (4.2)$$

In equation (4.2), μ_g is the mixture-averaged viscosity, and D_{kl}^e and $D_{k,Kn}^e$ are the effective molecular diffusion coefficients and Knudsen diffusion coefficients. These are calculated as shown in equations (4.3) and (4.4):

$$D_{kl}^e = \frac{\phi_g}{\tau_g} D_{kl} \quad (4.3)$$

$$D_{k,Kn}^e = \frac{4}{3} \cdot \frac{\phi_g}{\tau_g} r_p \sqrt{\frac{8RT}{\pi W_k}} \quad (4.4)$$

The porosity ϕ_g and mean pore radius r_p of the porous media are estimated using porosimetry techniques [118]. The tortuosity τ_g is usually fitted to experimentally measured gas flow resistance as outlined subsequently in this chapter. The ordinary binary diffusion coefficients D_{kl} in equation (4.3) and μ_g are calculated from kinetic gas theory. The permeability of a porous media can be approximated by the Cozeny-Karman relationship (equation (4.5)):

$$B_g = \frac{\phi_g^3 r_p^2}{18\tau_g (1-\phi_g)^2} \quad (4.5)$$

In equation (4.2), the DGM diffusion coefficients are calculated as $D_{kl}^{DGM} = H^{-1}$, where the elements of matrix H are given by equation (4.6) (where δ_{kl} denotes the Kronecker delta):

$$h_{kl} = \left[\frac{1}{D_{k,Kn}^e} + \sum_{j \neq k} \frac{X_j}{D_{kj}^e} \right] \delta_{kl} + (\delta_{kl} - 1) \frac{X_k}{D_{kl}} \quad (4.6)$$

4.2.2 Numerical implementation

For the Pd-H₂ thermochemistry, the numerical implementation has been recorded in the previous chapter. The corresponding state-space vector consists of surface coverages on either surface ($\theta_{k,feed}$ and $\theta_{k,perm}$) and near-surface bulk H-mole fractions ($X_{H,feed}$ and $X_{H,perm}$). The feed and permeate side gases, are treated as semi-infinite reservoirs, and serve as boundary conditions for each run of the model. The MATLAB integration routine *ode15s* is used for this problem because of the stiffness involved.

For the porous media transport model, the asymmetric ceramic substrate (bulk mesoporous ceramic tube with a thin nano-porous ceramic coating on the OD) is

discretized into slices or cells. For the current study, the bulk macroporous substrate (which is held at a fixed radial thickness of 2.2 mm) is discretized into four cells of equal radial thickness. The thin mesoporous ceramic layer (fixed at a 24 μm radial thickness) is discretized into two cells of equal radial thickness. An increase in the number of discretizations does not change the predicted steady-state flux significantly. For the model with the porous support, the state-space vector consists of average temperature, pressure and composition of the gas in each of these cells. The gas properties on the high and low pressure sides (OD and ID of the asymmetric support respectively) are maintained constant for a given run of the model, and served as boundary conditions for the first and last cells in the substrate. Again, the Matlab solver *ode15s* is used to integrate equation (4.1) to steady state.

For the combined composite membrane model, the above two models are combined into a system of ODEs (consisting equations (3.6) and (3.7) on each Pd surface, and equation (4.1) in each discretized cell of the porous media). At the porous media-Pd film interface, H_2 desorption rates on the permeate side of the Pd film serve as the effective boundary condition for the first cell in the mesoporous layer in the porous support. Because of the specific experimental test conditions in this study, where pure H_2 streams at near fixed pressures exists on both sides of the composite membrane, the 1-D “through-the-membrane” model is adequate for comparing the model predictions and experiments. As such, the model was not implemented here with axial discretization along the length of the membrane.

4.3 Experiment

4.3.1 Bare substrate pressure drop

A porous α -alumina tube (length = 300 mm, OD = 5.7 mm, ID = 3.5 mm, $\phi_g = 22\%$, $r_p = 0.5 \mu\text{m}$) is chosen as a substrate for a mesoporous coating and thin Pd membrane. Before depositing the mesoporous Al_2O_3 layer or electroless deposition of Pd on this tube, the permeability of the bare substrate is measured with Helium gas at room temperature. The flow rate through the membrane varies linearly with the gas pressure-drop in the range of pressures tested, and the permeance $j_{\text{tot}}/(\rho(P_{\text{feed}} - P_{\text{perm}}))$ is calculated from the experimental measurements to be $2.24 \cdot 10^{-4} \text{ m}^3 \cdot \text{m}^{-2} \cdot \text{s}^{-1} \cdot \text{kPa}^{-1}$) at room temperature. The porous substrate model described above is used to match the flow resistance by varying the otherwise uncertain tortuosity τ_g . The other properties for the porous substrate are listed in Table and are based upon physical characterization of the substrate. By using the model, a reasonable value of $\tau_g = 2.75$ provides a good fit to the porous substrate flow resistance and is used in the combined models to discuss below.

In order to anchor the Pd film effectively but minimize penetration of Pd into the macropores of the bare substrate, an intermediate Al_2O_3 mesoporous ceramic layer ($\sim 24 \mu\text{m}$ thick, $\phi_g \approx 22\%$, $r_p = 0.05 \mu\text{m}$) is deposited on the outer diameter of the bare substrate using a sol gel process. With the addition of this intermediate layer, total permeance of the asymmetric tube is measured to decrease to $1.97 \cdot 10^{-4} \text{ m}^3 \cdot \text{m}^{-2} \cdot \text{s}^{-1} \cdot \text{kPa}^{-1}$. Using the porous media model again with the added mesoporous layer cells, τ_g for the mesoporous layer is varied to fit the results and a value of 1.4

provided reasonable agreement. While it is not expected that the smaller porosity mesoporous layer should have a lower τ_g than the more porous bare support, the limited thickness of this layer may result in the reduced τ_g for this layer.

Table 4.1: Material properties of the two layers in the asymmetric α -alumina tube

| <i>Parameter</i> | <i>macroporous bulk</i> | <i>mesoporous layer</i> |
|-------------------|-------------------------|-------------------------|
| φ_g | 22% | 22% |
| r_p (nm) | 500 | 50 |
| τ_g (fitted) | 2.75 | 1.4 |

4.3.2 Pd-ceramic composite membrane testing

A 5-6 μm Pd layer is deposited using electroless plating on the outside of the mesoporous layer on a 300 mm long porous tube. After plating, the tube is cut and the analyzed with a scanning electron microscope. Figure 1.4 shows a typical SEM cross-section of the Pd membrane and the mesoporous layer, with a relatively uniform 5-6 μm Pd film. The Pd film does have a polycrystalline nature but the grain sizes appear to be on the order of the film thickness and as such diffusion through/across the grain boundaries is not expected to have a significant impact on the bulk diffusion of H through the Pd film. The mesoporous intermediate ceramic layer is typically around 30 μm ($\pm 5 \mu\text{m}$) thick and its microstructure is evident in Figure .

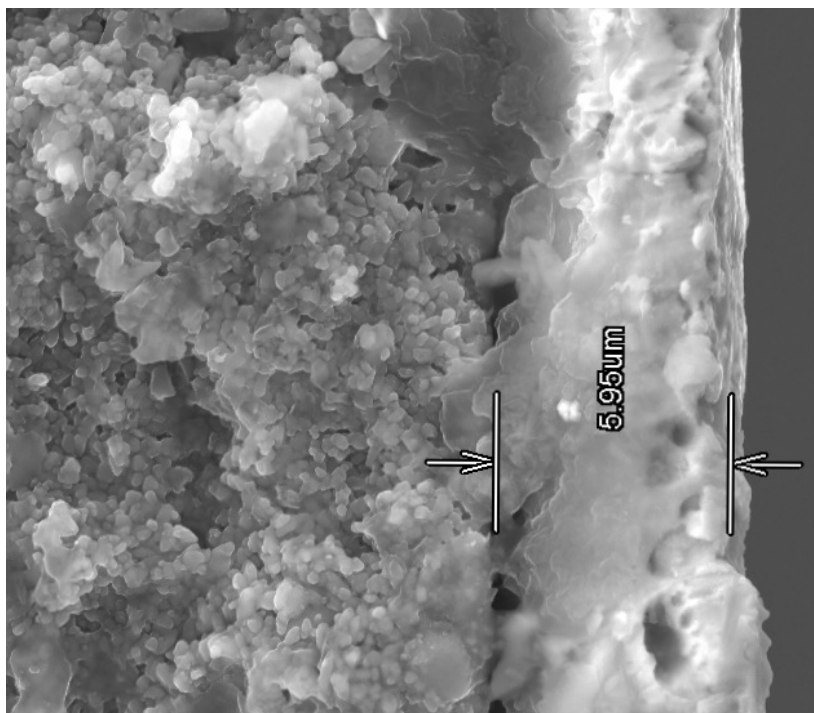


Figure 4.1: A typical cross-sectional electron-micrograph of the Pd-ceramic composite membrane. The porous macroporous & mesoporous layers can be distinguished from the brighter Pd metal.

For experimental tests, a Pd-coated tube with a 100 mm long test section is centered inside a stainless steel tube (9.5 mm OD) with the help of Swagelok® fittings with graphite ferrules as shown in Figure . The active Pd length, or distance between the graphite ferrules is 87.5 mm. The membrane test assembly includes the annular compartment exposed to the Pd membrane for the high pressure feed side and the inside of the hollow ceramic tube acting as the low pressure permeate side. To check for leaks, the feed side was pressurized to 140 kPa gage pressure with N₂ at room temperature, while the permeate side was open to atmosphere. A pressure transducer (with a minimum sensitivity of 7 Pa) connected to the high-pressure side did not detect any measurable drop in pressure over 30 minutes, confirming that the

membrane had no significant pinholes and that the graphite seals were sufficiently leak-right.

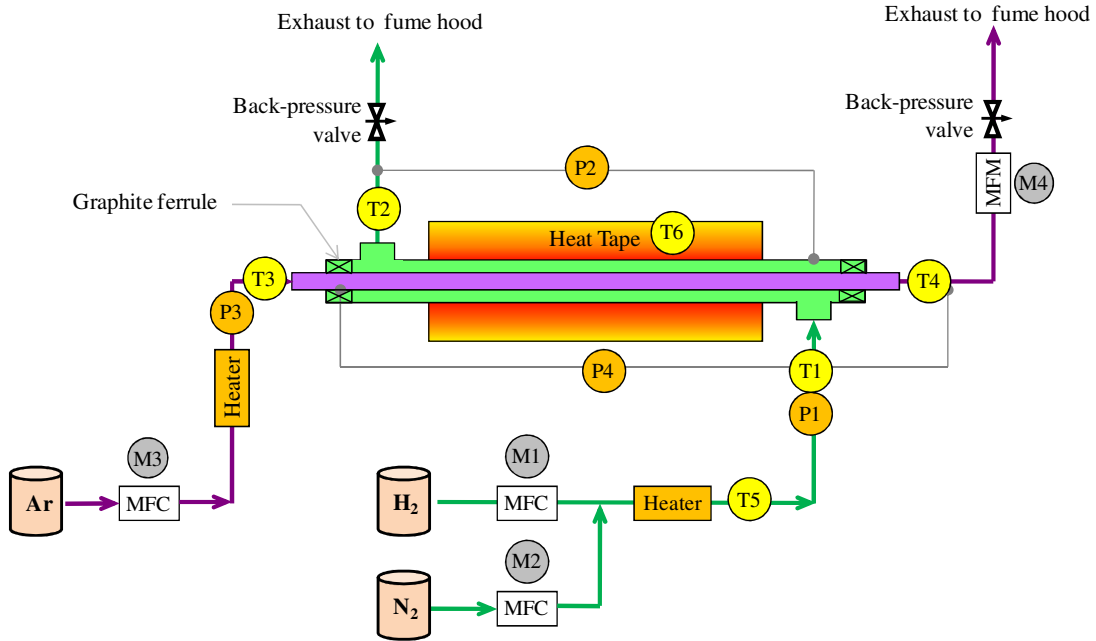


Figure 4.2: Experimental setup for pure H₂ composite membrane tests

As shown in Figure , temperatures and pressures were measured at inlet and exit of feed and permeate flows. In addition, two thermocouples measured the temperature at the center of the Pd-ceramic tube on the permeate side. To prevent heat loss and to ensure isothermal operation, the assembly was insulated with Fibrafax alumina wool. While inert gases were passed on either side of the membrane, temperature was slowly increased to 350 °C, ensuring that all thermocouples were within 10 °C of one another. The pressure drop between the inlet and exit of each stream is measured to be less than 70 Pa for all test conditions, and hence is neglected in the analysis. Since H₂ is the only gas on either side of the membrane under the flux conditions, the low pressure differentials along the length of the tube implies that the 1-D model as

described in the previous section is adequate to model this system if H₂ is the only gas on either side of the composite membrane.

To check for leakage at higher temperatures, electronic mass flow controllers (Brooks 5850E) (M1 and M3) control the flow of N₂ on the Pd side and Ar on the ceramic side of the membrane assembly. A magnetic mass spectrometer (ThermoFisher Prima δb) measures N₂ leaking to the permeate side. Even at the highest temperature (450 °C), no N₂ is detected at a cross-membrane pressure differential of 200 kPa. At this temperature, air is passed on both feed and permeate sides to remove any adsorbed contaminants on the Pd surfaces. The air is purged with N₂ and Ar on each side respectively before introduction of H₂ to avoid a combustion event.

For the H₂ flux measurements for the 6 μm thick Pd membrane, the permeate side mass flow controller (M3 in Figure 1.5) is shut off, effectively dead-ending the permeate side of the composite membrane. Pure H₂ is introduced through M1, and pressure was controlled with the help of back pressure valves located downstream of the membrane. The experiments at $T > 300$ °C are performed first, because these correspond to the strictly dilute α -phase in the Pd-H phase diagram [42]. Next, the membrane assembly is purged with inert gases until no traces of H₂ remained in the system (confirmed with mass spectrometer analysis of purge gases). T is then lowered and held at 250 °C and 200 °C for the corresponding data.

The results for the composite Pd membrane testing are shown as symbols in Figure for the entire range of testing temperatures and for a range of H₂ partial pressure driving forces with $100 \leq (PX_{H_2}) \leq 400$ kPa. The measured average H₂ fluxes (J_{H_2}) are plotted in Figure vs. $(PX_{H_2})_{\text{feed}}^{0.5} - (PX_{H_2})_{\text{perm}}^{0.5}$ to assess the applicability of Sievert's law to fitting the data. For the supported 6 μm thick Pd membrane, the experimental data suggest a near linear relationship between J_{H_2} and $(PX_{H_2})_{\text{feed}}^{0.5} - (PX_{H_2})_{\text{perm}}^{0.5}$ for the lower temperature data. On the other hand, the scatter in the data at the two highest temperatures is explained in part by the fact that particularly at high temperatures, the flux data is not best fitted with an $n = 0.5$ as discussed below. Variations in permeate side pressure in the experimental tests, particularly at the high T , cause the experimental data to show significant scatter when plotted vs. $(PX_{H_2})_{\text{feed}}^{0.5} - (PX_{H_2})_{\text{perm}}^{0.5}$.

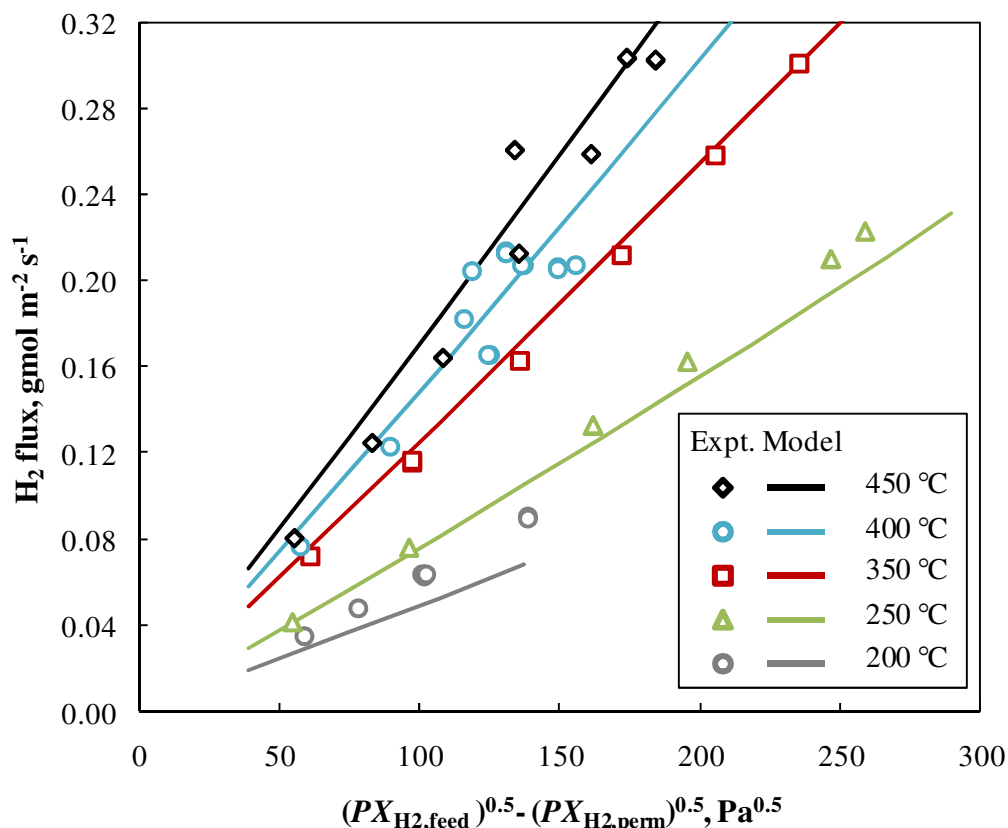


Figure 4.3: Comparison of experimental data (symbols) with model results for Pd-ceramic composite membranes at $200 < T < 450$ °C.

The experimental data actually suggest that the best fit using equation (2.1) for the experimental data suggest higher values of n over the range of temperatures tested. At the lowest $T = 200$ °C, the fitted n value is about 0.85. At 200 °C, the solubility of H in Pd is non-linear with $(PX_{H_2})^{0.5}$, as shown in Figure (page 54), due to the strong H-H interaction potential. As T increases to 350 °C, the fitted n drops to 0.69 due to the reduced importance of the non-idealities in the Pd-H thermodynamics with increasing T and due to the fact that at these intermediate temperatures, bulk metal diffusion still plays a significant role in the total resistance to H₂ flux across the membrane. As T increases further, the fitted n increases again, because the substrate

resistance (which scales with $\Delta(PX_{H_2})^{1.0}$) becomes increasingly important relative to the resistance of the H diffusion through the Pd bulk. Table 4.2 provides the fitted K_H and n values as a function of T .

Table 4.2: Fitted n and K_H values for experimental data at different temperatures ($\Delta z_{\text{memb}} = 6 \mu\text{m}$)

| T | n | K_H $gmol m m^{-2} s^{-1} Pa^n$ |
|-----|------|--------------------------------------|
| 200 | 0.85 | $6.0 \cdot 10^{-11}$ |
| 250 | 0.71 | $3.0 \cdot 10^{-10}$ |
| 350 | 0.69 | $5.4 \cdot 10^{-10}$ |
| 400 | 0.75 | $3.0 \cdot 10^{-10}$ |
| 450 | 0.82 | $1.2 \cdot 10^{-10}$ |

4.4 Model results and discussion

To compare with the experimental results, the composite membrane model is run over the entire range of pressures and temperatures tested in the experimental conditions. The model results are plotted as solid curves for the different test temperatures in Figure . Model results agree extremely well with the experimental measurements for $250 \leq T \leq 400$ °C and $100 \text{ kPa} \leq (PX_{H_2})_{\text{feed}} \leq 400 \text{ kPa}$. In this temperature range, the effective H_2 permeance (K_H when $n = 0.5$ in equation (2.1)) of the composite membrane does not increase with temperature exactly as D_H in equation (3.11)

because as discussed above, the decreased resistance of H diffusion through the Pd film at higher temperatures results in an increased importance of the flow resistance of the porous media. This is discussed further below, and the agreement between model predictions and experimental measurements indicates that the model captures this trade-off with sufficient accuracy.

At the highest temperature, $T = 450 \text{ }^\circ\text{C}$, the model results over-predict the experimental results by about 10%. The linear variations of ΔH_{sol} with temperature may become less accurate at higher T and lead to the over-predictions in the permeance of the Pd. In addition to issues related to the model, the experiments may have been influenced by increased temperature non-uniformity at the highest test temperatures – particularly at the edges of the test section. Although the measured temperatures were controlled to within $10 \text{ }^\circ\text{C}$, increased heat losses at the ends of the tube may have caused more significant local drops in permeance, especially near the ends of the membrane assembly for the highest test temperatures. This offers an explanation as to why the experimental permeance values at $450 \text{ }^\circ\text{C}$ are only about 10% higher than those at $400 \text{ }^\circ\text{C}$.

At the lowest temperature $T = 200 \text{ }^\circ\text{C}$, the model results under-predict the experimental results by as much as 30%. The approximations of the thermodynamic parameters, as described in the previous chapter are less accurate at lower temperatures, because of both larger variation in $X_{\text{H,bulk}}$ across the metallic membrane and of potential localized $\alpha \rightarrow \beta$ phase transitions. Furthermore, these phase

transitions can cause the metallic lattice to undergo an expansion-contraction cycle below 300 °C during exposure to higher H₂ partial pressures and can result in increased defects in the Pd film. This can also lead to slight pinholes and higher effective D_H than predicted by extrapolating results from higher temperature properties which may also explain why the experimental results at 200 °C are significantly higher than the model predictions in Figure . Experimental leak checks after measuring H₂ fluxes at 200 °C with the 5-6 μm thick Pd membranes showed minor traces of N₂ leaking across to the permeate side (~ 1 sccm at 200 kPa pressure differential across the membrane corresponding to a flow resistance of 8210 kPa·m³·m²·hr, i.e., > 5000X the flow resistance of the porous support).

To quantify further the model results, plots of H chemical potential changes across the membrane were examined in order to compare the resistance of the various processes associated with hydrogen transport across the composite membrane. Figure -Figure show the variation in the chemical potential per H (μ_H) atom at various locations across the Pd membrane for the range of $\Delta(PX_{H_2})$ tested at four different test temperatures: 200, 250, 350, and 450 °C. The resistance associated with a given step in the transport process can be quantified by the $\Delta\mu_H$ associated with that process and as such the plots in these figures provide a basis for assessing the relative importance of the processes as temperature increases. The plots show that bulk and surface processes in the Pd are primarily rate-limiting at temperatures < 300 °C. As the temperature increases above 300 °C, porous substrate resistance (for the low porosity bulk support tube tested) becomes a more and more significant fraction of the

resistance. Thus, with the current composite membranes for high temperature operation, improvement in H₂ permeance (and the accompanying reduction in size) can be achieved not only by reducing Pd film thickness but also by reducing substrate resistance (through increased porosity).

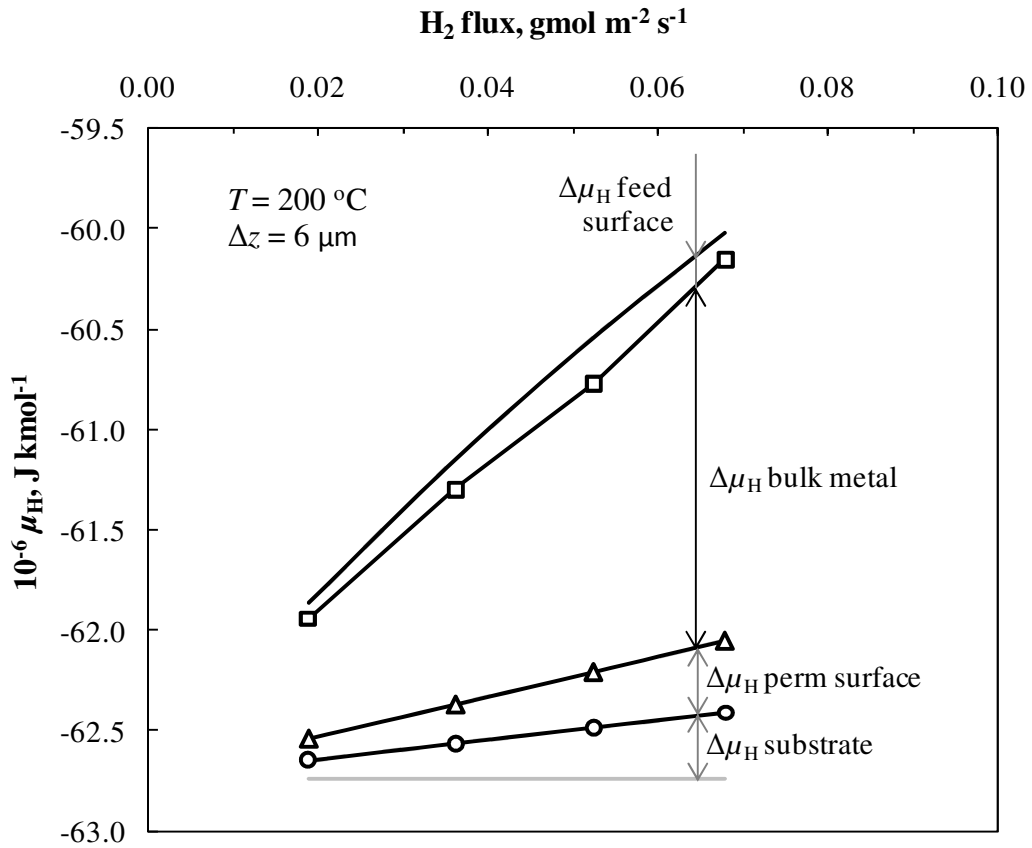


Figure 4.4: Model predicted drops of H chemical potential due to the Pd surfaces, the Pd bulk and porous substrate; $\Delta z_{\text{memb}} = 6\mu\text{m}$, $110 \leq (PX_{\text{H}_2})_{\text{feed}} \leq 220 \text{ kPa}$, $(PX_{\text{H}_2})_{\text{perm}} = 110 \text{ kPa}$, $T = 200 \text{ }^\circ\text{C}$

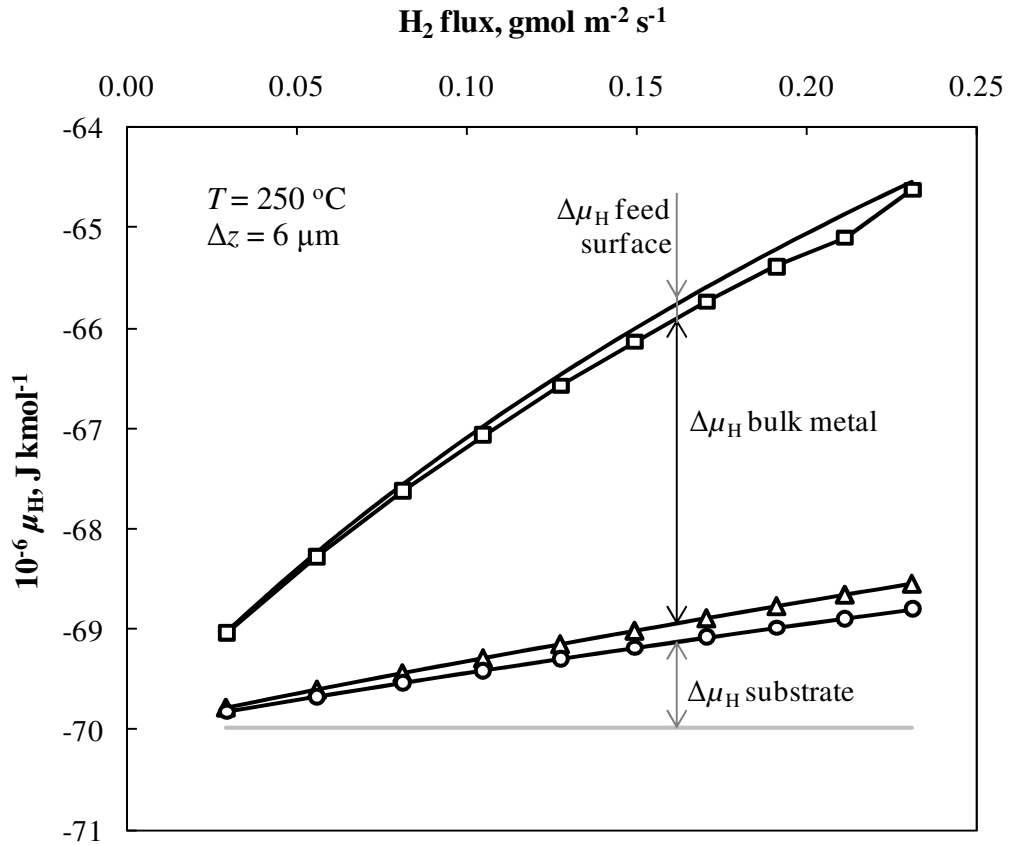


Figure 4.5: Model predicted drops of H chemical potential due to the Pd surfaces, the Pd bulk and porous substrate; $\Delta z_{\text{memb}} = 6 \mu\text{m}$, $110 \leq (PX_{\text{H}_2})_{\text{feed}} \leq 220 \text{ kPa}$, $(PX_{\text{H}_2})_{\text{perm}} = 110 \text{ kPa}$, $T = 250 \text{ }^\circ\text{C}$

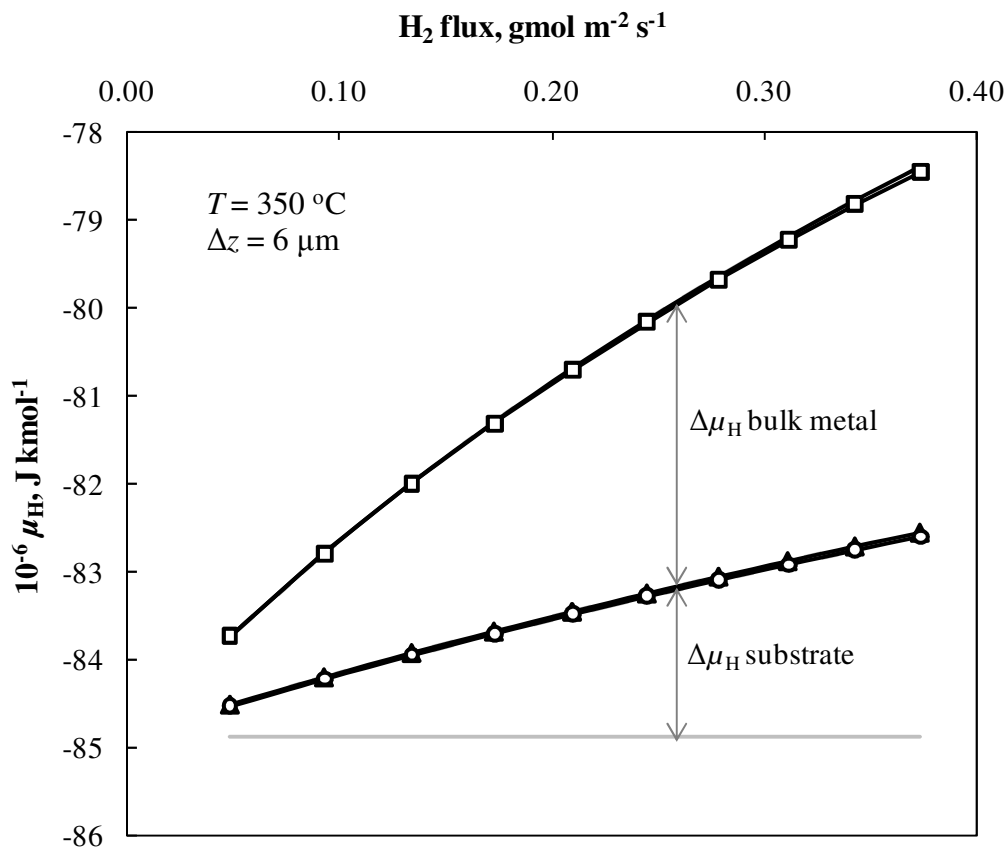


Figure 4.6: Model predicted drops of H chemical potential due to the Pd surfaces, the Pd bulk and porous substrate; $\Delta z_{\text{memb}} = 6 \mu\text{m}$, $110 \leq (PX_{\text{H}_2})_{\text{feed}} \leq 220 \text{ kPa}$, $(PX_{\text{H}_2})_{\text{perm}} = 110 \text{ kPa}$, $T = 350 \text{ }^\circ\text{C}$

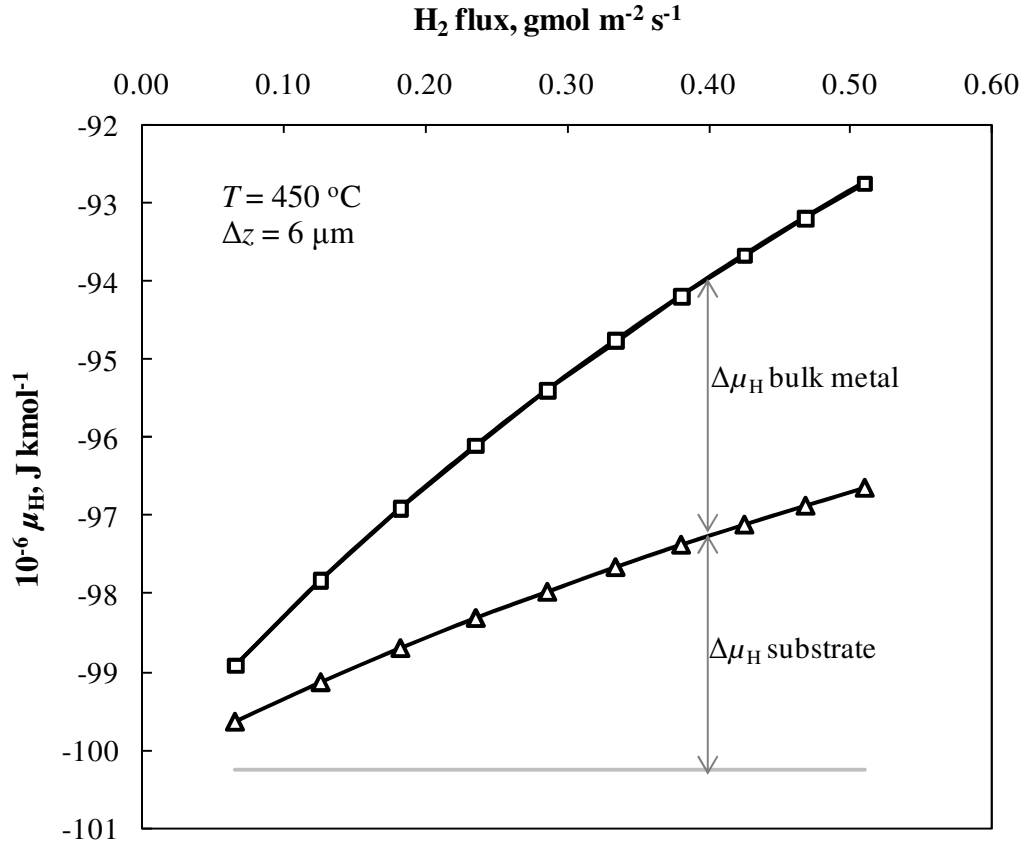


Figure 4.7: Model predicted drops of H chemical potential due to the Pd surfaces, the Pd bulk and porous substrate; $\Delta z_{\text{memb}} = 6 \mu\text{m}$, $110 \leq (PX_{\text{H}_2})_{\text{feed}} \leq 220 \text{ kPa}$, $(PX_{\text{H}_2})_{\text{perm}} = 110 \text{ kPa}$, $T = 450 \text{ }^\circ\text{C}$

With the continued attempt to develop thinner supported Pd-based membranes, the model is used to assess how a reduction in Pd membrane thickness to $3 \mu\text{m}$ influences H₂ flux performance with the existing ceramic support used in this study. The results are plotted for 200 and 450 °C in Figure and Figure . Comparing these results to the $6 \mu\text{m}$ thick Pd membrane results in Figure and Figure show that at the low temperatures (where membrane bulk H diffusion dominates), the H₂ fluxes are almost doubled. On the other hand at higher temperatures as represented by 450 °C, the fluxes only increase by a factor of $\sim 50\%$ because at such conditions, the porous support provides a substantial fraction of the resistance as indicated by the relative

height of the chemical potential difference across the porous substrate. These results indicate that improvements in permeance at high temperatures can be gained by reducing porous substrate resistance as much as by reducing Pd membrane thickness for thin-supported membranes. Reducing membrane thickness on the other hand can decrease cost, but it may also make the membrane susceptible to pin-hole formation or de-lamination, thereby decreasing H₂-selectivity and durability. Similarly, reducing substrate thickness or increasing pore-size is also associated with decreased mechanical strength and reliability.

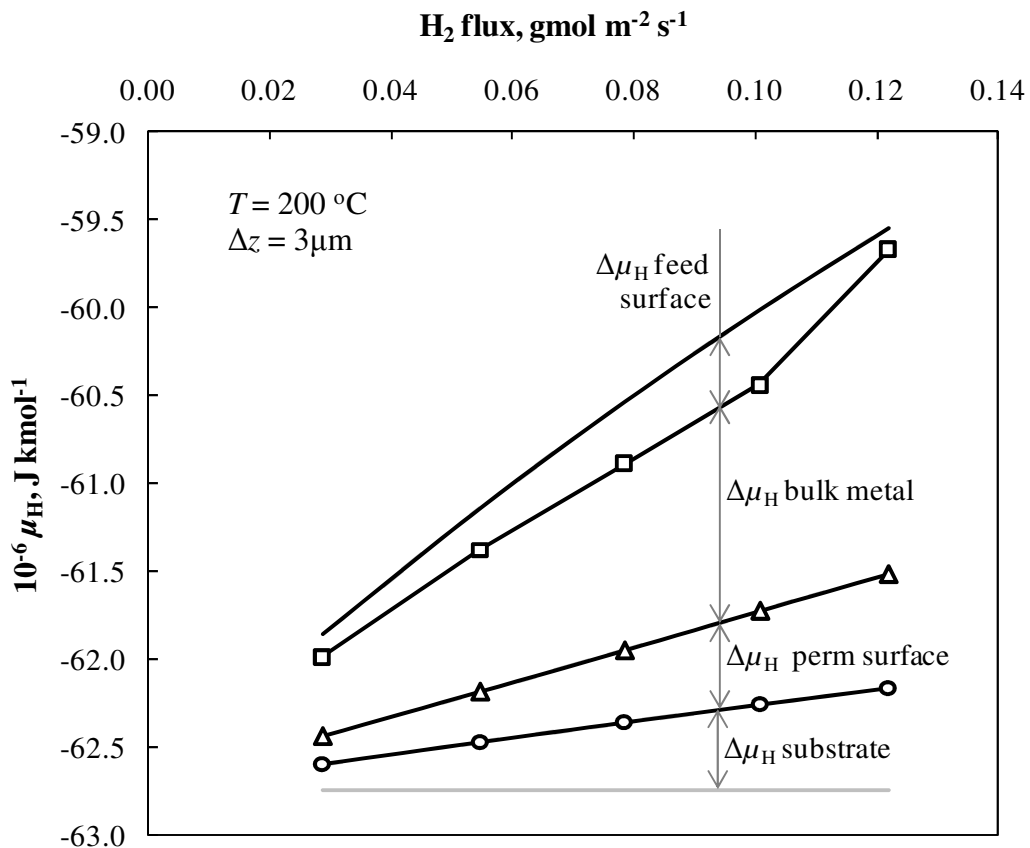


Figure 4.8: Model predicted drops of H chemical potential due to the Pd surfaces, the Pd bulk and porous substrate; $\Delta z_{\text{memb}} = 3 \mu\text{m}$, $110 \leq (PX_{\text{H}_2})_{\text{feed}} \leq 220 \text{ kPa}$, $(PX_{\text{H}_2})_{\text{perm}} = 110 \text{ kPa}$, $T = 200 \text{ }^\circ\text{C}$

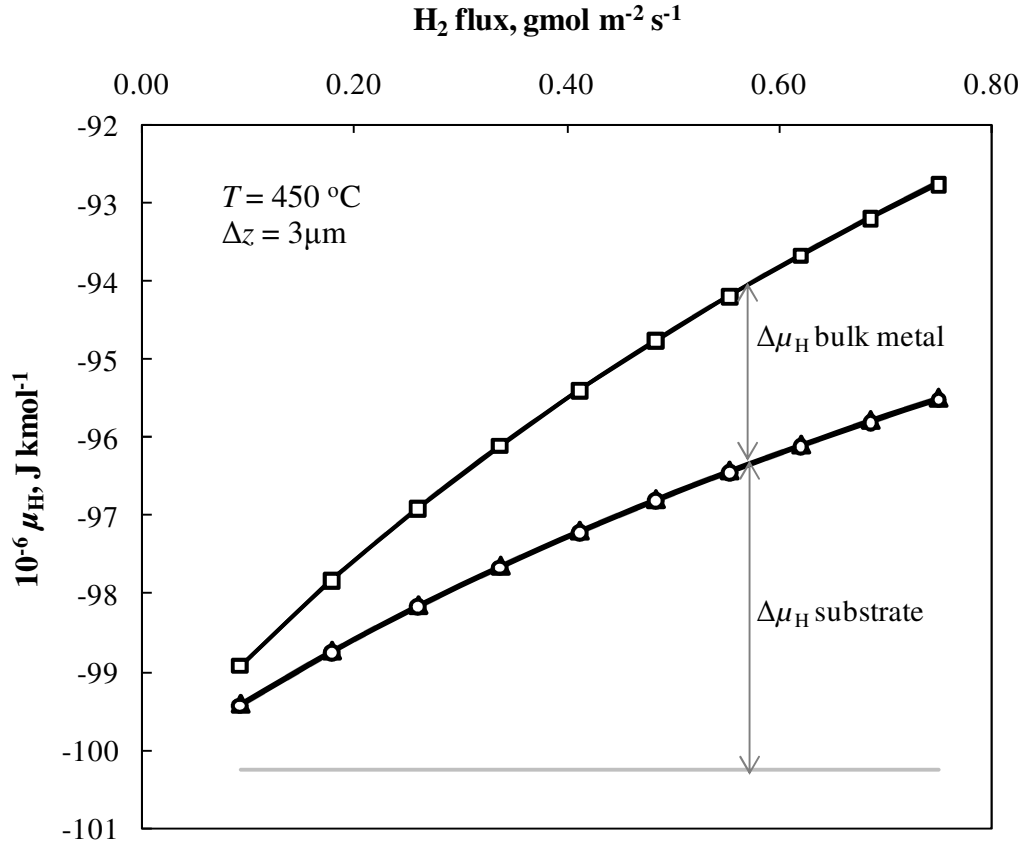


Figure 4.9: Model predicted drops of H chemical potential due to the Pd surfaces, the Pd bulk and porous substrate; $\Delta z_{\text{memb}} = 3\mu\text{m}$, $110 \leq (PX_{\text{H}_2})_{\text{feed}} \leq 220 \text{ kPa}$, $(PX_{\text{H}_2})_{\text{perm}} = 110 \text{ kPa}$, $T = 450 \text{ }^\circ\text{C}$

Another important consideration in this study is the impact of removing the intermediate mesoporous ceramic layer to reduce ceramic resistance and decrease manufacturing cost. In the absence of a mesoporous layer, some Pd particles may penetrate into the macropores of the bare ceramic substrate. While this construction may allow for a cheaper composite membrane, it can tend to reduce available surface area for desorption on the permeate side of the Pd film, thereby reducing H₂ permeance, especially at lower temperatures. The composite membrane model is used to quantify these effects by varying ϵ_{surf} at the surface in contact with the porous support. Results are shown in Figure for membrane simulations at 250 °C with the

tested 6 μm Pd-film and bare-substrate combination (without the mesoporous layer). For this thickness of membrane, the results are not sensitive to reduction in surface availability on the permeate side until ϵ_{surf} falls below 0.4. Because the surface desorption processes are not rate limiting at this membrane thickness, it takes significant drops in ϵ_{surf} before the membrane performance is impacted by the loss in area.

The model was run for thinner Pd membranes (3 and 1 μm thick) with results plotted in Figure . It is understood that membranes as thin as 1 μm may require some sort of surface reconfiguration to reduce pore size there in order to avoid excessive strain in pores in the supporting mesoporous layer that are more than 10% of the membrane thickness, but the modeling results for the hypothetical membranes are still performed to understand the potential benefits of the thinner membranes. Results show that the thinner membranes do have a higher sensitivity to reductions in ϵ_{surf} . For a 1 μm Pd film, the flux reduces by half if the surface availability reduces to 15%. In general, as Pd membranes become thinner and thinner (below 5 μm), minimizing blockage of the Pd surface by the porous support becomes more and more important design consideration (particularly for lower temperature operation).

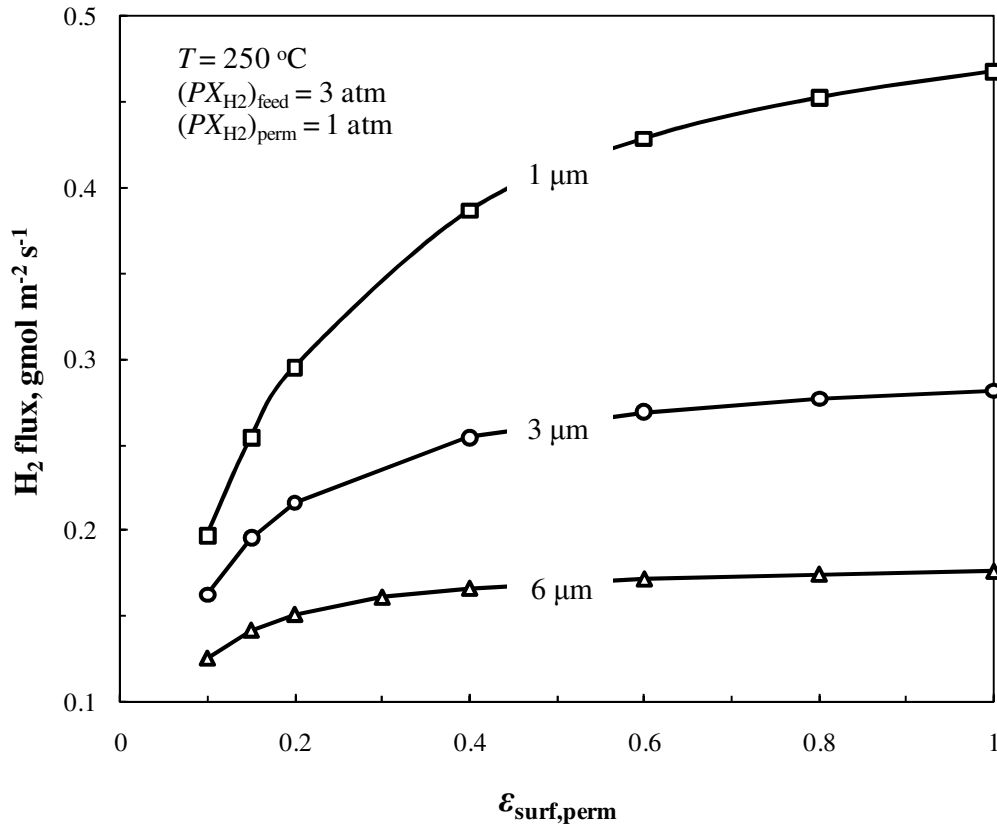


Figure 4.10: Effect of surface availability $\epsilon_{\text{surf,perm}}$ on performance of 1, 3 and 6 μm composite membranes at $T = 250\text{ }^{\circ}\text{C}$, typical operating conditions

4.5 Summary

The micro-kinetic model for disordered, dilute α -phase Pd-H₂ interaction that was presented in the previous chapter has been further validated for relatively thinner membranes (it had been previously validated against thicker membrane experimental data in the literature) and then has been combined with a porous media dusty-gas transport model to simulate supported Pd membranes for H₂ separation applications. To accurately model H₂ flux through metallic membranes, it is essential to capture the equilibrium solubility of H in the membrane bulk. To this end, both enthalpic and entropic components of metal-H₂ interaction must be quantified. The Pd-H bulk and

surface micro-kinetic model, coupled with the porous media transport model predicts well H_2 fluxes through a composite membrane constructed by depositing a 6 μm Pd film on an industrial porous ceramic substrate for temperatures above 200 $^\circ\text{C}$ and a wide range of H_2 partial pressures.

The model has been used to quantify the various rate-limiting processes for H_2 transport as a function of temperature across such a composite membrane. It has further been applied in a limited way to explore the benefits (in terms of increased H_2 flux) of various design improvements such as reduced membrane thickness or reduced porous support blockage. Parametric studies indicate that as membrane thickness is reduced to 3 μm or lower, ceramic substrate resistance becomes increasingly important and reductions in ceramic substrate resistance will improve H_2 flux as much if not more than reductions in membrane thickness. Furthermore, for such very thin membranes, a relatively free surface for H_2 desorption on the permeate side is critical to take full advantage of the reduced membrane or support resistance. This model provides the basis for expanding its capabilities to incorporate multiple species adsorption and desorption on Pd, , as well as transport through porous media. Future studies can use this work to explore the effects of competitive adsorption on both sides of the membrane on H_2 flux for critical applications like reformat-based H_2 purification for fuel cells.

Chapter 5: Competitive adsorption on Pd surface

5.1 Introduction

One of the most critical issues for Pd-based membranes in H₂ purification from reformat gases is the mitigation of poisoning (both reversible and irreversible) of the metal surface due to other gases such as CO and H₂S in the reformat stream. [57]. Some species, such as CO or H₂O can cover the surface with reversible poisoning in which the species can be removed with increasing temperatures or changes in flow composition. On the other hand, irreversible damage of the membrane can be caused by sulfur containing compounds, or by hydrocarbon species that can cause carbon deposition on the Pd alloy surface. Sulfur poisoning can be mitigated either through the use of sulfur adsorbers upstream of the purifier, or alternatively, to a limited extent through the use of Pd-based alloys with Cu or Au [44, 57, 119, 120]. Carbon deposition during long term operation can be avoided through the continuous or intermittent use of steam to clean the Pd surface. However, prolonged carbon deposition can lead to carbon dissolving in Pd and thereby irreversibly damage the membrane [57, 110]. These irreversible reactions that change membrane morphology are outside the scope of this research work. However, the current chapter will explore the effects of reversible adsorption on Pd membranes for key species (H₂O, CO, and CO₂) in hydrocarbon reformat feeds.

5.2 Thermo-kinetics of Pd surface chemistry

Reversible competitive adsorption of species on the Pd surface by species such as CO and H₂O, affects H₂ dissociative adsorption in two ways. First, it reduces the number of Pd sites available for H₂ adsorption. Second, some adsorbed species have repulsive interactions with adsorbed H atoms, thereby decreasing the activation energy barrier for desorption of H. In this chapter, experimental data in the literature are used to approximate critical parameters for the adsorption of CO and H₂O on to the Pd surface. These thermodynamics of CO and H₂O on Pd are then added to the microkinetic model for Pd-H₂ interactions developed in chapter 3, thereby enhancing the microkinetic model to include Pd interactions with reformat gases such as CO and H₂O. It has been established that the poisoning effect of CO and H₂O is reduced in the case of Pd alloys with Cu, Ag and Au [57]. This is mainly due to the reduction in binding energies of most species (including H) on alloy surfaces [57]. It will be challenging to develop these models for all the different alloy compositions that are being studied. However, a pure Pd model provides a good first step to building such models. Therefore, microkinetic models for CO and H₂O adsorption on Pd alloys is not considered in this thesis, and is a subject for future work.

Reihani et al. have published a microkinetic mechanism for H₂ combustion on Pd nanoparticles [121]. The same authors have developed microkinetic mechanisms for CH₄ combustion on Pd as well. This mechanism is adapted for Pd-H₂-H₂O-CO interactions with the help of other experiments in the literature [122]. All surface reactions considered for this microkinetic model are shown in Table 5.2. Other

species such as CH₄ and other light hydrocarbons are expected to be present in much lower concentrations, and are not considered in the mechanism presented here [15]. At this point, modeling CO and H₂O is assumed to be adequate for capturing the principal trends in Pd-membrane performance for typical fuel cell system applications. O₂ adsorption is considered in order to develop JANAF coefficients for O(s).

For CO and H₂O, the sticking probability, s^0 , in adsorption equation (3.1), and the desorption pre-exponential factor A_{des} and activation energy barrier $E_{\text{a,des}}(\theta_k)$ in equation (3.2) are estimated using experimental results in the literature by starting with values derived from DFT studies or fundamental experiments and fitting them to experimental CO/ H₂O poisoning data on free-standing Pd membranes. Temperature dependences of the sticking coefficient and the attempt frequency for desorption β_{ads} and β_{des} are both assumed to be 0 due to lack of sufficient experimental data to assess such temperature variation in reaction rates beyond the Arrhenius factor. For the Arrhenius term, the activation energy barrier is assumed to be a function of surface coverages due to interaction potentials between surface species. Thus, $E_{\text{a,des}}(\theta_k)$ for H(s) will include the effects of CO and H₂O on the H-Pd surface bond energy. Other species will also have adsorption enthalpies influenced by surface coverages, and these issues leading to the values and expressions in Table 5.1 are discussed further here.

Table 5.1: Relative enthalpies of surface specie on Pd surface (relative to standard gas phase enthalpies and a clean Pd surface at 298.15 K)

| <i>surface species</i> | h_k (kJ gmol ⁻¹) |
|------------------------|--|
| Pd(s) | 0.0 |
| O(s) | -115 + 57.5 θ_O + 29 θ_{OH} |
| H(s) | -42 + 8 θ_H + 8 θ_{CO} + 32 θ_{H_2O} |
| OH(s) | -214 + 29 θ_O + 14.5 θ_{OH} |
| H ₂ O(s) | -75.5+32 θ_{H_2} ($\theta_{H_2O} < 0.5$) -151 + 151 θ_{H_2O} +32 θ_{H_2} ($\theta_{H_2O} > 0.5$) |
| CO(s) | -136 + 45 θ_{CO} + 16 θ_{H_2} |

Table 5.2: Surface reactions on Pd (excludes surface-bulk interactions of H atom)

| Reactions | A or s^0 | E_{act} (kJ/mol) |
|--|------------------------------|--|
| <i>Adsorption/ desorption reactions</i> | | |
| 1f) O ₂ +2Pd(s) ⇒ 2O(s) | 0.8*T ^{0.5} | 0.0 |
| 1r) 2O(s) ⇒ O ₂ +2Pd(s) | 5.7*10 ²¹ | 230 - 115 θ_O |
| 2f) H ₂ +2Pd(s) ⇒ 2H(s) | 6.4*T ^{0.5} | 0.0 |
| 2r) 2H(s) ⇒ H ₂ +2Pd(s) | 5.7*10 ²¹ | 84 - 16 θ_H - 16 θ_{CO} -32 θ_{H_2O} |
| 3f) H ₂ O+Pd(s) ⇒ H ₂ O(s) | 1 | 0.0 |
| 3r) H ₂ O(s) ⇒ H ₂ O+Pd(s) | 1.0*10 ¹³ | 75.5-32 θ_{H_2} ($\theta_{H_2O} < 0.5$) 151 - 151 θ_{H_2O} -32 θ_{H_2} ($\theta_{H_2O} > 0.5$) |
| 4f) CO + Pd(s) ⇒ CO(s) | 0.5 | 0.0 |
| 4r) CO(s) ⇒ CO + Pd(s) | 10 ¹⁵ | 136 - 45 θ_{CO} -16 θ_{H_2} |
| 5f) CO ₂ +2Pd(s) ⇒ CO(s)+O(s) | 0.005 | 81.0 |
| 5r) CO(s)+O(s) ⇒ CO ₂ +2Pd(s) | 5.7*10 ²¹ | 185+57.5 θ_O +29 θ_{OH} +10.59 θ_{CO} |
| <i>Reversible reactions</i> | | |
| 6) H(s)+O(s) ⇌ OH(s)+Pd(s) | 5.7*10 ²¹ | 128 |
| 7) H(s)+OH(s) ⇌ H ₂ O(s)+Pd(s) | 5.7*10 ²¹ | 102 |
| 8) OH(s)+OH(s) ⇌ H ₂ O(s)+O(s) | 5.7*10 ²⁰ | 117 + 8 θ_H |

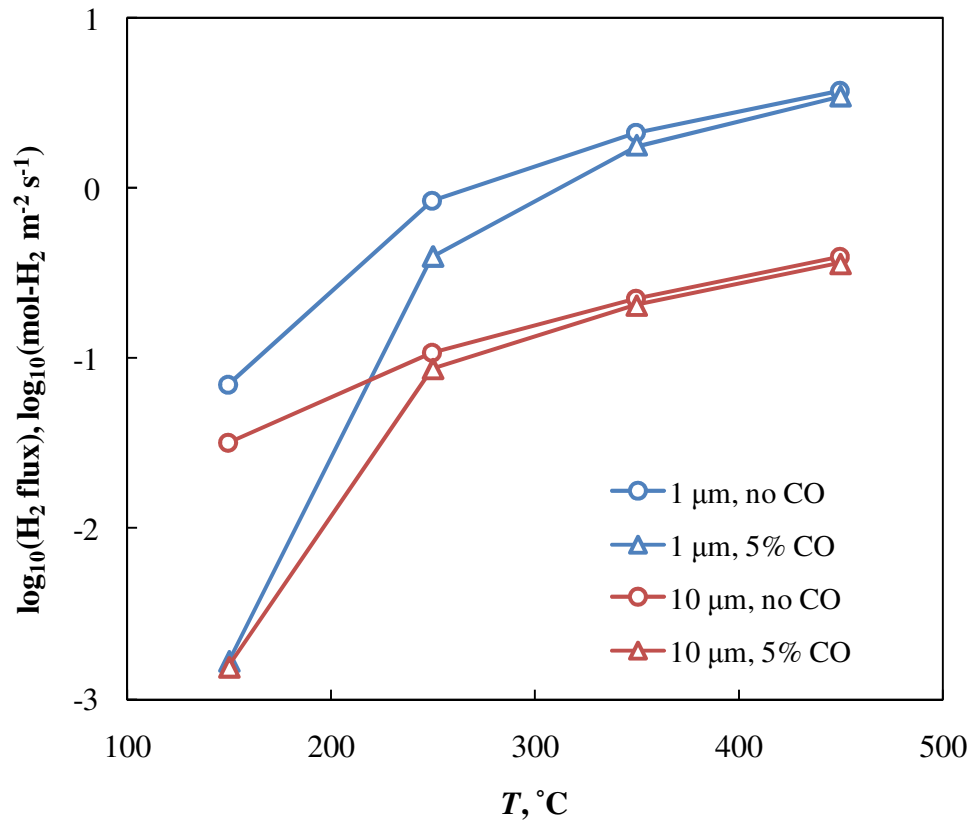
5.3 CO & CO₂ poisoning on Pd surfaces

Li et al have shown that CO has a mild poisoning effect on a 10 μm thick Pd/stainless steel composite membrane at 380 °C [88]. However, CO poisoning is more significant at lower temperatures; Wang et al have shown that H₂ flux through a 200 μm thick free-standing Pd foil is reduced by about 67% at 150 °C in the presence of 6 mol% CO in the feed gas [89]. Although poisoning due to the presence of CO₂ has also been reported [110], the effect has been shown to be due to CO₂ reduction to CO from dissociative adsorption and not due to direct molecular adsorption of CO₂ on the Pd surface. In the presence of significant amounts of CO on the Pd surface, reaction 5 is not expected to proceed in the forward direction. Moreover, because of the presence of H₂O, the overall chemical potential gradient favors the forward water-gas shift reaction, thereby further reducing the probability of CO₂ decomposition [123]. Hence, literature parameters are retained for that reaction [106] without further modification.

A number of fundamental experiments have been carried out for CO-Pd interactions, particularly in the context of Pd-catalyzed CO oxidation [124-127]. Since a range of values for heat of adsorption between 116 and 150 kJ*mol⁻¹ have been reported in these references, a median E_{des} of 136 kJ*mol⁻¹ on a clean polycrystalline Pd surface is used in this study. Similarly, A_{des} is taken as $\sim 10^{15}$ m*gmol⁻¹*s⁻¹ from Hoffman et al. [124]. Hoffman et al. assume constant $E_{\text{des}} = 110\text{-}136$ kJ*mol⁻¹ and a variable sticking coefficient $s^0(\theta_{\text{CO}}) \approx 1 - 2\theta_{\text{CO}}$, thereby limiting the maximum CO coverage to 0.50.

However, with these values for CO adsorption, results with the microkinetic model developed in this thesis indicate that the H₂ flux through a 10 μm thick free standing Pd membrane will not be significantly affected (<10% decrease) at $T = 150$ °C even in the presence of 10 mol% CO, which is contrary to experimental observations as discussed above. Lattice-gas studies using Monte Carlo simulations show that although there is a discontinuous change in the binding energy of CO on Pd (110) at $\theta_{\text{CO}} = 0.5$ by as much as 50%, the strong pair-wise CO-CO interactions lead to a decrease in the binding energy with θ_{CO} even at $\theta_{\text{CO}} < 0.5$ [128]. Because the Pd-CO binding energy does not decrease to 0 beyond $\theta_{\text{CO}} > 0.5$, it is reasonable to assume that $\theta_{\text{CO}} > 0.5$ is possible. It follows from the above discussion that E_{des} should also decrease with θ_{CO} . For the purposes of this model, a linear decrease with θ_{CO} is assumed for $0 < \theta_{\text{CO}} < 1$. Alfonso has also shown that the binding energy for H adsorbed on Pd decreased with CO coverage [129]. In the absence of more experimental or first principles data, it is assumed that the H-CO repulsive interactions are approximately equal to the H-H interactions. Therefore, a linear dependence $dE_{\text{des,H}}/d\theta_{\text{CO}} = -8.0 \text{ kJ}\cdot\text{mol}^{-1}$ is assumed. With $s_{\text{CO}}^0 = 0.5$, the slope $dE_{\text{des,CO}}/d\theta_{\text{CO}}$ is varied until the CO poisoning effect matches with the low temperature experimental data [89]; this value is $45 \text{ kJ}\cdot\text{mol}^{-1}$. The same parameter values are then used to check for CO poisoning effect at 380 °C, and is found to match experimental results [88]. Since the porosity and tortuosity of the stainless steel substrate used in this reference are not known, the substrate resistance is assumed to be equal to that of the industrial ceramic substrate used in this research work.

The CO surface reactions are added to the Pd-H₂ interaction model described in chapter 3. Model results for CO poisoning are shown in Figure (a). It is clear from the figure that CO poisoning is strongly dependent on temperature. Since it is a surface phenomenon, there is a larger relative decrease in H₂ flux through thinner membranes, as plotted in Figure (a) using a logarithmic scale on the flux axis to aid in visual comparison. With 5% CO by volume in the feed side, for very thin ~1 μm membrane, CO poisoning effect can be significant up to 350 °C, whereas for thicker 10 μm membrane, the effect is only mild above 250 °C. The competition for the Pd surface is further illustrated in Figure (b), where θ_H and θ_{CO} are plotted for the 1 μm membrane. Thus, in hydrocarbon-fueled PEMFC systems where H₂ purification is required, efforts to decrease Pd membrane thickness will not yield proportional gains in flux for membranes below ~5 μm in thickness.



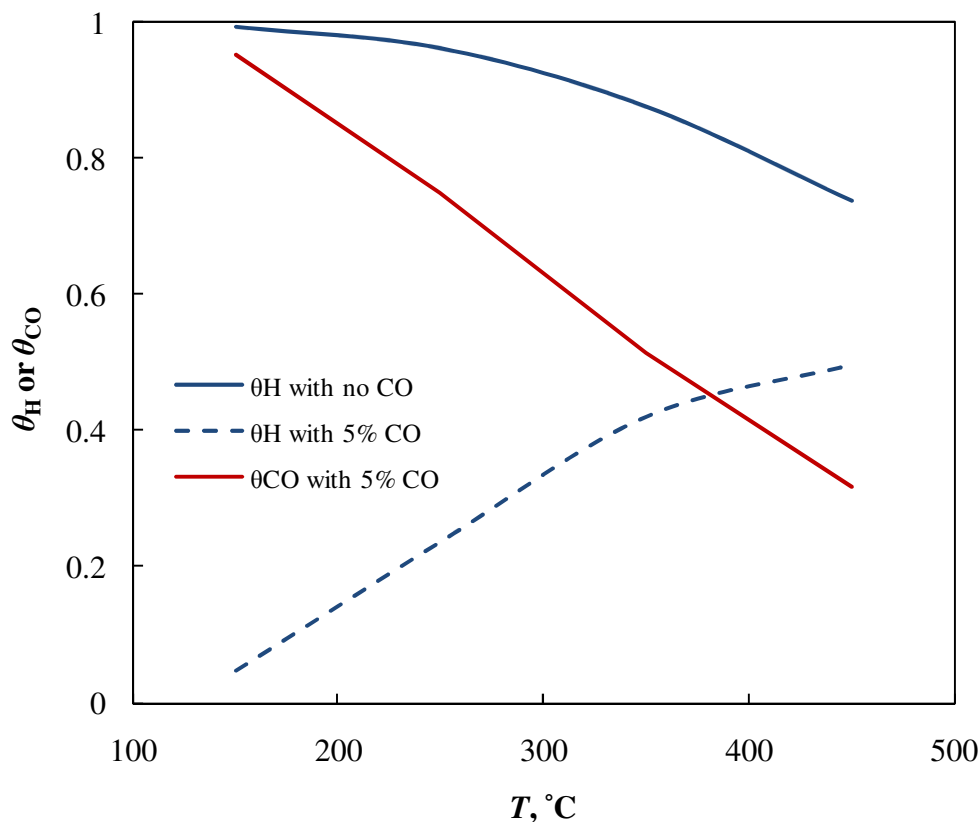


Figure 5.1: (a) Model results showing effect of CO on H₂ flux through free standing 1 μm and 10 μm Pd membranes. $(PX_{\text{H}_2})_{\text{feed}} = 100 \text{ kPa}$, $(PX_{\text{H}_2})_{\text{perm}} = 10 \text{ kPa}$. Feed side is 95% H₂ with balance N₂ or CO. (b) surface coverages θ_{H} and θ_{CO} for a 1 μm thick membrane at same conditions as in (a).

5.4 H₂O poisoning on Pd surfaces

Some experimental studies have suggested that H₂O has a stronger inhibitive effect on H₂ flux than CO [86, 88]. Alfonso has argued through DFT studies that the poisoning of Pd surfaces is due to the dissociation of the adsorbed H₂O to OH and H, and further decomposition of OH to O and H [129]. Alfonso calculated the binding energy for each of these surface species and argued that adsorbed O, due to its relatively high binding energy is responsible for destabilizing H adsorption as well as decreasing the number of sites available for dissociative adsorption. The microkinetic

model previously developed for Pd nano-particles is adapted to test this assertion [130]. The activation energy barriers and rate constants for reactions 6 and 7 are taken from Alfonso's DFT study. Model results show that there is virtually no O on the surface. This is due to high θ_{H} , which drives both the above reactions backwards, and any O on the surface is recombined to OH, and further to H₂O. Even considerable changes to the values proposed by Alfonso did not yield O coverage on the Pd surface above 10^{-6} . Therefore, site blocking or bond destabilization by O cannot be the chief reason for H₂O poisoning in the presence of H₂.

Henderson has shown that due to hydrogen bonding, H₂O molecules cluster on metal surfaces [50], and Gao et al have used these results to argue that H₂O molecules poison the surface through clustering [57, 131]. Since the microkinetic model in this research uses a mean-field approach that does not capture geometric variations on the surface, it is assumed that the surface poisoning mechanism of H₂O in the presence of H is due to the stronger adsorption of H₂O and the weakening of the H binding energy and the concomitant reduction of $E_{\text{a,des,H}}$.

Experiments on 1 μm thick free standing Pd membranes have shown that the H₂ flux is reduced by ~ 42%, 50% and 67% at $T = 450, 400$ and 350 °C respectively in the presence of 20 mol% H₂O [110]. When microkinetic model parameters in the literature are used to simulate this condition, the model does not predict any significant decrease in H₂ flux at any of these temperatures. Therefore, s^0 is increased to 1.0 and $E_{\text{des,H}_2\text{O}}$ is also raised to $75.5 \text{ kJ}\cdot\text{mol}^{-1}$,. Furthermore, $dE_{\text{a,des,H}}/d\theta_{\text{H}_2\text{O}}$ is set

to $-16 \text{ kJ}\cdot\text{mol}^{-1}$. However, when the model is run at low T ($< 300 \text{ }^\circ\text{C}$) with these modified parameters, the Pd surface is entirely covered with H_2O , and H_2 flux is reduced to 0. On the other hand, experiments on a composite Pd membrane (described in chapter 6 and similar to the one described in chapter 4) indicate that H_2 flux is not reduced to 0 even at $250 \text{ }^\circ\text{C}$. Therefore, the activation energy $E_{\text{des,H}_2\text{O}}$ is assumed to decrease linearly to 0 beyond a surface coverage of 0.5. This functional dependences of $E_{\text{des,H}_2\text{O}}$ is shown in Table 5.1 by the two expressions. The H_2O surface reactions are added to the Pd- H_2 interaction model described in chapter 3. A comparison between experimental and model results is shown in Figure . It is seen that in the presence of 20mol% H_2O , H_2 flux through a $1 \text{ }\mu\text{m}$ free-standing Pd membrane is reduced even at higher temperatures ($350 \text{ }^\circ\text{C}$).

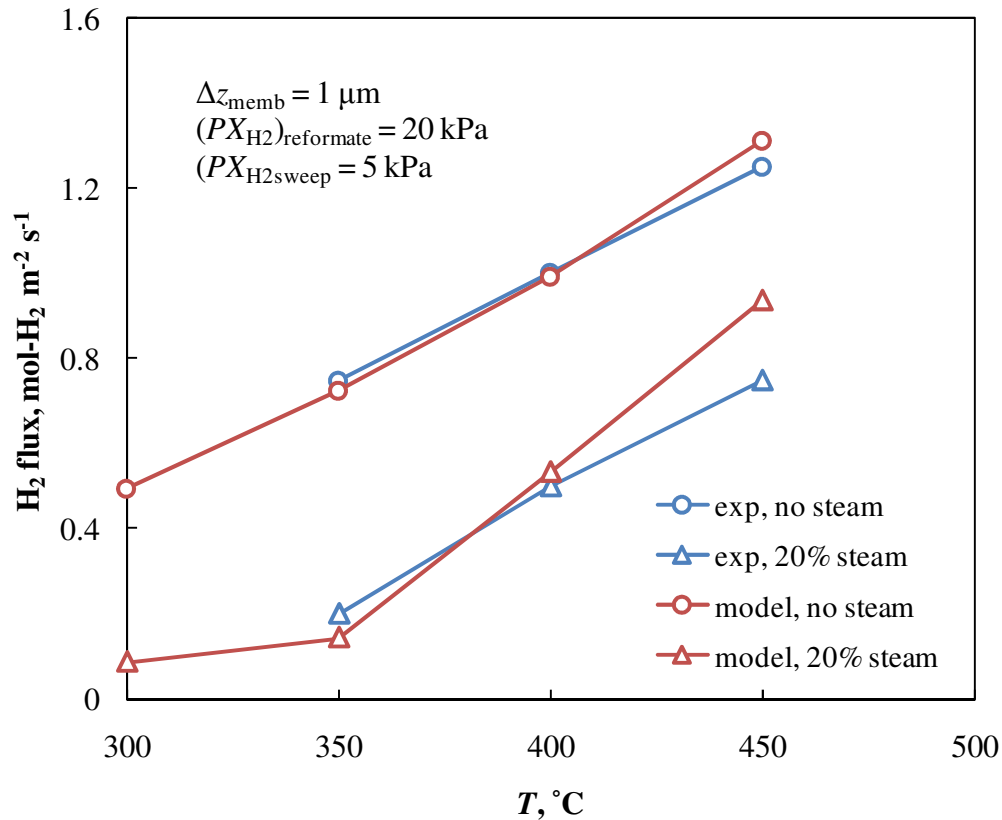
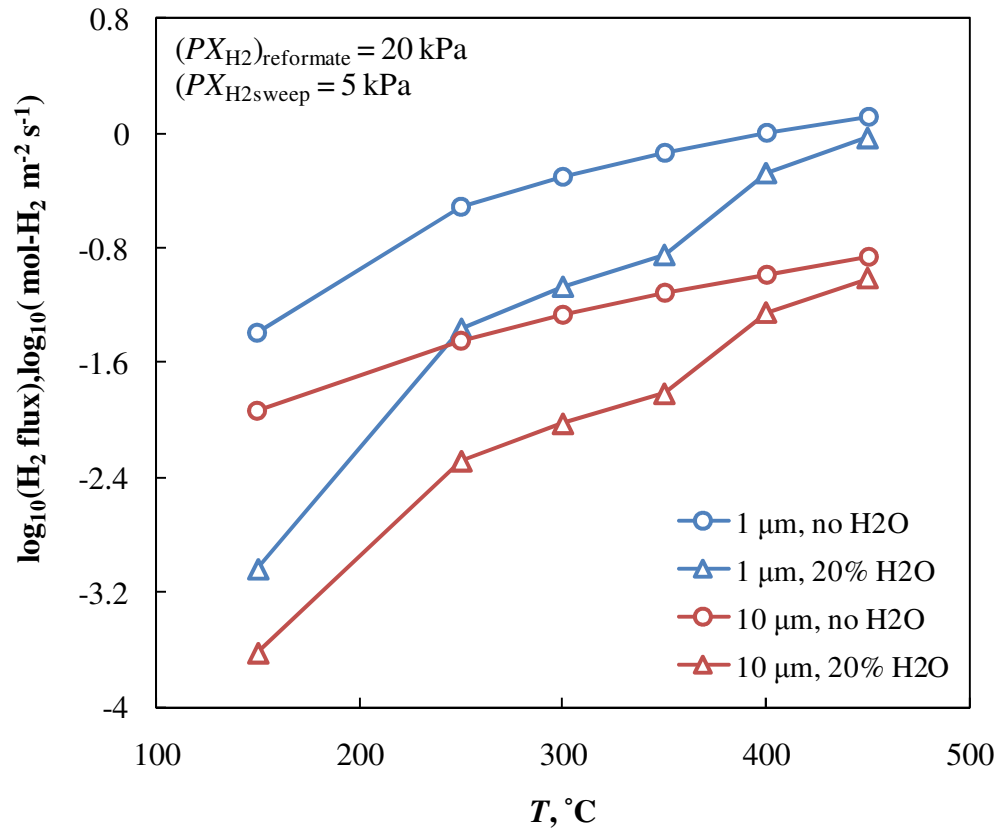


Figure 5.2: Poisoning effect of steam. Red lines indicate model results, blue lines are from experiments by Gielens et al. $\Delta z_{\text{memb}} = 1 \mu\text{m}$; $(PX_{\text{H}_2})_{\text{feed}} = 20 \text{ kPa}$, $(PX_{\text{H}_2})_{\text{perm}} = 5 \text{ kPa}$. Feed side is 20% H_2 and 20% N_2 or H_2O

Figure 5.3a shows the effect of temperature and membrane thickness on the significance of H_2O poisoning. It is clear that H_2O poisoning is also strongly influenced by temperatures, with the reduction being relatively large for thinner membranes. As seen from the Figure 5.3b, at lower temperatures H_2O covers a large portion of the Pd surface, thereby reducing the H-Pd surface reaction rates. However, at higher temperatures, H_2O only occupies a smaller fraction of the surface, and the reduction in surface rates has a relatively modest effect on overall H_2 flux.



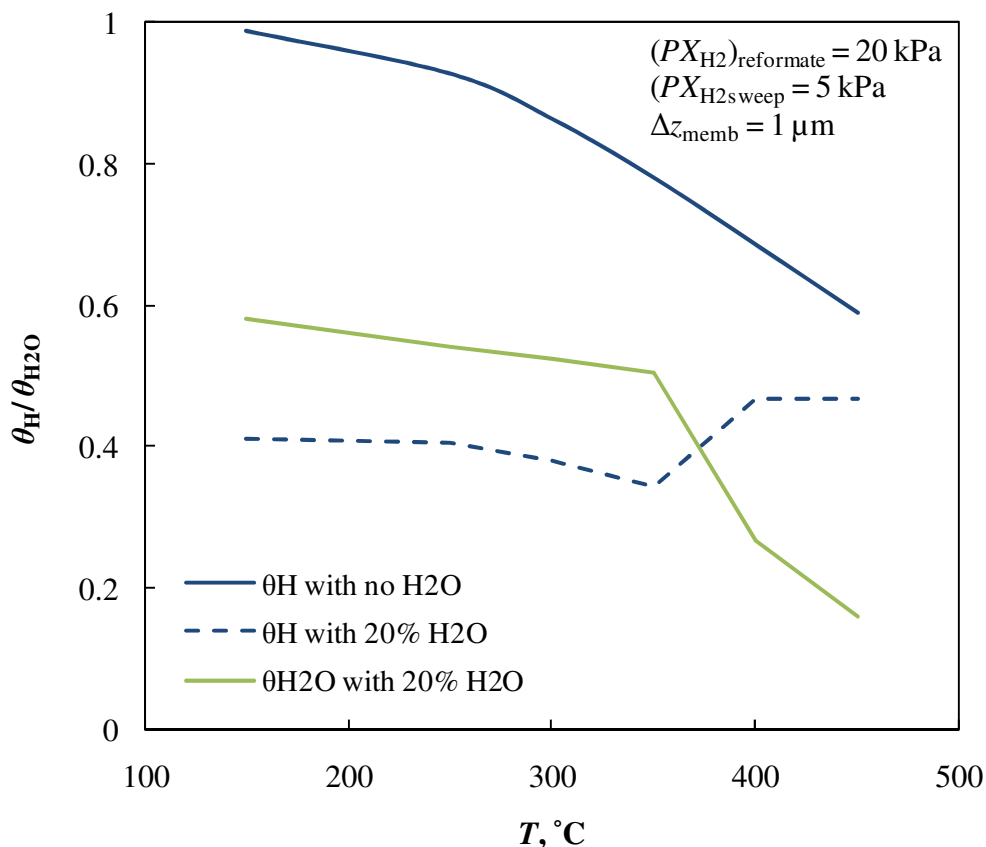
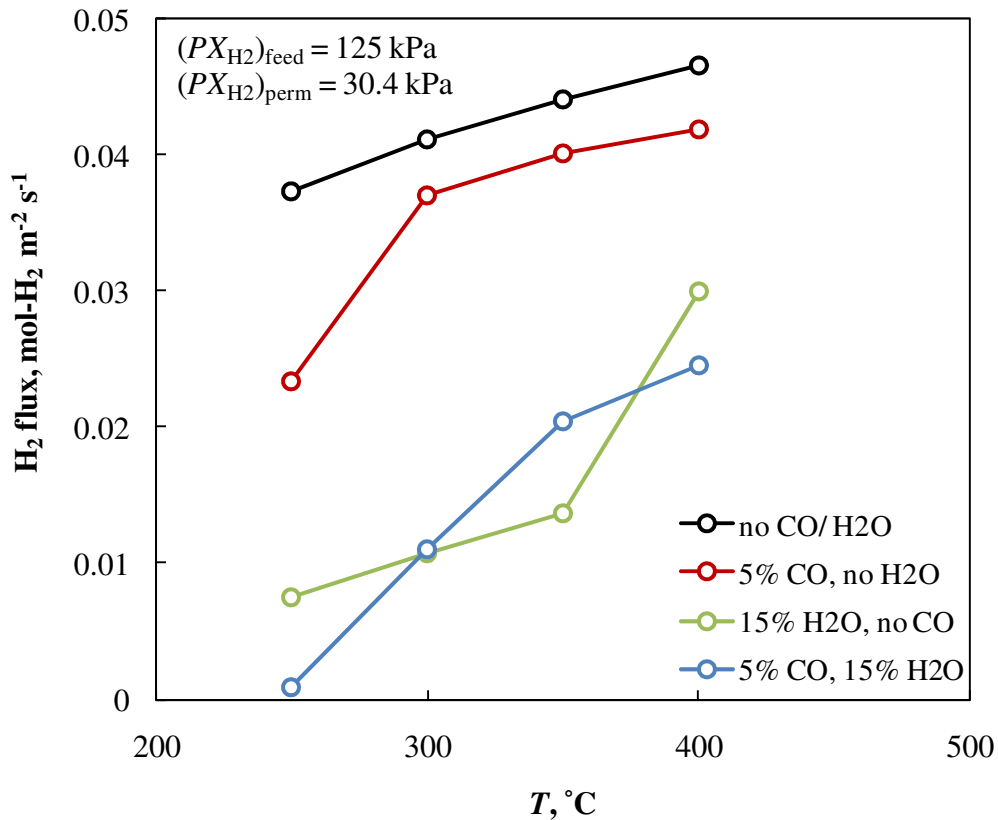


Figure 5.3: (a) Effect of H₂O poisoning on H₂ flux through 1 μm and 10 μm thick Pd membranes. Reformate side is 20% H₂/ balance N₂ for no H₂O cases and 20% H₂/ 20% H₂O balance N₂ for steam cases. (b) Surface coverages θ_H and θ_{H_2O} for the 1 μm thick membrane for the same conditions as in (a).

5.5 Combined effect of CO and H₂O

Gielens et al have shown that the Pd surface is not a very good promoter of the water-gas shift reaction [110]. Therefore, although WGS reactions are allowed through reactions 5, 6 and 7 (see 5.2), the combined poisoning effect of H₂O and CO are expected to be more significant than the effects of H₂ production due to water gas shift. The microkinetic model is used to study the effect of CO and H₂O in typical fuel cell conditions. Model results indicate that for a 6 μm thick Pd film deposited on an industrial ceramic substrate, CO+H₂O poisoning is significant at temperatures

below 300 °C. Figure also shows the reduction in H₂ flux for both the poisoning species if they were present in the absence of the other. At low temperatures (< 300 °C), both CO and H₂O strongly adsorb on the Pd surface and significantly reduce θ_H coverage as compared to conditions where no CO/ H₂O is present. At moderate temperatures (300-400 °C), the presence of CO on the surface reduces θ_{H_2O} , thereby reducing the strong H₂-H₂O interactions. This increases θ_H compared to the condition where only H₂O is present, and hence results in higher flux. These model results are also consistent with Li et al's observation that H₂ flux is reduced more when the CO : H₂O ratio is 1:2 than when it is 2:1 at $T = 380$ °C [88]. This trend is again reversed at high temperatures (> 400°C) when θ_H is limited by the H₂ sticking coefficient $s^0 T^{-\beta}$.



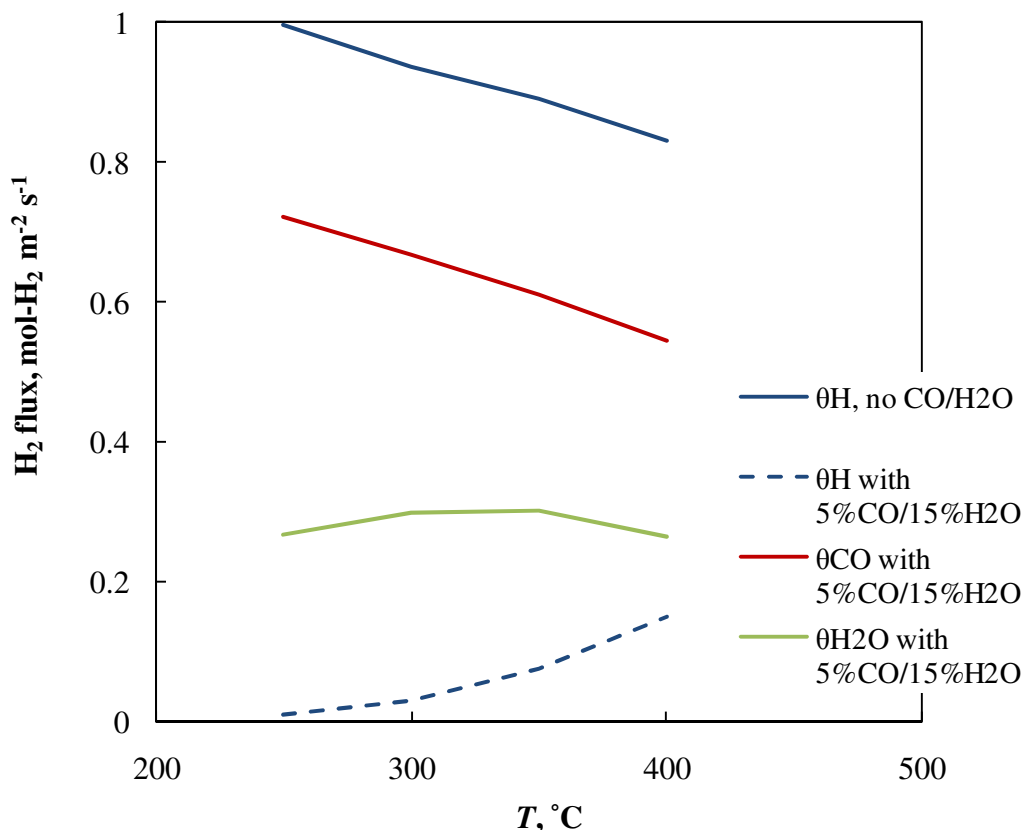


Figure 5.4: (a) Model results showing combined effect of CO + H₂O on H₂ flux through Pd ceramic composite membranes. $\Delta z_{\text{memb}} = 6 \mu\text{m}$; see Table 4.1 for ceramic substrate properties; $(PX_{\text{H}_2})_{\text{feed}} = 124 \text{ kPa}$, $(PX_{\text{H}_2})_{\text{perm}} = 30.9 \text{ kPa}$. Feed side is 35% H₂ with balance N₂ when no CO or H₂O is present. 35% H₂, 5% CO, 15% H₂O, balance N₂ for appropriate case as indicated in figure. Also shown for comparison in red and green are H₂ fluxes with only one poisoning species present (either 5% CO or 15% H₂O) ; (b) surface coverage for same conditions as in (a) when neither poisoning species are present and when both species are present

5.6 Summary

Parameters for competitive adsorption of CO and H₂O on a pure Pd surface are determined using experimental data in the literature. The poisoning effects of these species are strongly temperature dependent: there is considerably more poisoning at lower temperatures. It is shown that surface site blocking by these species is the

primary reason for the reduction in H_2 flux. This completes the Pd- H_2 / H_2O / CO interaction model, which can be used in flow models of the membrane purifier.

Chapter 6: Quasi 1-D “down-the-channel” membrane purifier model

6.1 Introduction

In this chapter, the “through-the-membrane” composite Pd-membrane-gas interaction model developed in chapters 3-6 is combined with channel flow equations to build a “down-the-channel” membrane reactor model. Development of the channel model provides insight regarding the various rate-limiting processes associated with H₂ transfer in the context of changing gas composition along the channel. This quasi-1D model can then be used to carry out design improvements and optimization studies.

For the “down-the-channel model, conservation equations for the channel flow are presented and added to the membrane model. Solution strategies for the 2-D model are also provided. Model results are compared with counter-current gas flow experiments on a single-tube Pd ceramic composite membrane. These experiments (and model runs) are carried out at conditions that are typical for a membrane-based purifier in a 5 kW liquid hydrocarbon fueled PEMFC system as outlined in chapter 1.

6.2 Conservation equations

The membrane setup which is being modeled follows that of Figure 6.1, with counter-current reformat and feed streams. In the particular PEMFC system configuration that is modeled in chapter 1, the H₂-rich ATR exhaust is fed to the high pressure side

of the membrane purifier, while the H₂-depleted PEMFC anode exhaust is recirculated back to the low pressure side of the purifier to sweep H₂ from the membrane. Therefore, for model conditions here, the high pressure feed from the ATR is referred to as “reformat”, while the low pressure permeate side flow is referred to as “sweep”.

The length of the purifier is discretized into 30 segments. For each channel flow, the state space variables at each discretization consist of average temperatures T_{ch} , pressures P_{ch} and composition $Y_{k,ch}$ of the gas in the reformat and sweep sides of the composite membrane, the surface coverages θ_k on the two Pd surfaces, bulk H-fractions $X_{H,bulk}$ just inside the two surfaces, the average membrane temperature T_{memb} , and the average temperature T_{pm} , density ρ_{pm} and composition $Y_{k,pm}$ of the gas-phase in each of the discretized cells of the porous support. In addition to these, the temperature T_{int} , P_{int} and $Y_{k,int}$ of reformat and sweep gases immediately next to the surface on each side of the composite membrane are also part of the state space, but handled in a different manner as explained subsequently. For each segment, the total mass flow rates \dot{m} are stored at the exit boundaries of that segment (\dot{m} are part of the state space variables).

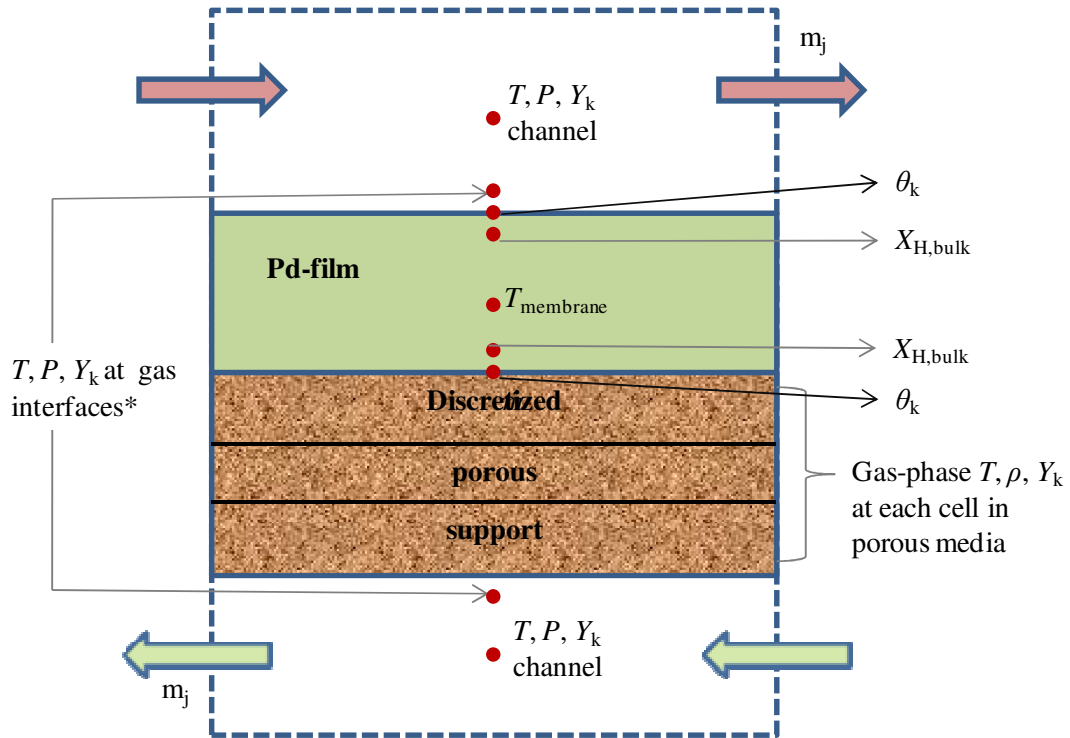


Figure 6.1: State space variables in each segment of the membrane purifier. Note that only exit mass flow rates are stored. *Interface variables are ‘algebraic’, and are handled separately, as discussed subsequently

In this work, model development and experimental validation are done at isothermal conditions. Hence, equations for the T 's are not presented; these are included in the state-space to enable further expansion to non-isothermal models in the future. In this chapter, equations for \dot{m} at the segment boundary, and P and Y_k at the channel and interface locations are presented. Equations for the other variables in the state space have been presented in chapters 3, 4 and 5 (see equations (3.6), (3.7) and (4.1)). The channel flow model provides a local boundary condition for the 1-D “through-the-membrane” model at each segment through the length of the composite membrane purifier.

The development and experimental validation of the 2-D “down-the-channel” model of the Pd-membrane purifier is done in the context of 100-tube purifier unit that was in the process of being developed in conjunction with a larger study to demonstrate a 5 kWe PEMFC generator for portable applications. Henceforth, experiments and model results are referred to as “full power” or “half power” corresponding to a net electric demand of 5 kWe and 2.5 kWe respectively. Although flows into the purifier are expected to vary considerably depending on other operating conditions and performance of other components in the system, it is taken as given for model development and membrane characterization purposes. These incoming flow properties for the 100-tube purifier are shown in Table 6.1.

Table 6.1: Composition and flow rate of gases entering 100-tube purifier unit in 5 kWe system (active length of each tube = 0.762 m)

| <i>parameter</i> | <i>reformat</i> | | <i>sweep</i> | | <i>units</i> |
|--|-------------------|------------|------------------|------------|--------------------------|
| | full power | half power | full power | half power | |
| \dot{m} | 4.2 (250) | 2.4 (140) | 0.57 (40) | 0.28 (20) | g s^{-1} (slpm) |
| Inlet P_{eH_2} | 1270 | 635 | 900 | 450 | - |
| Re | 97 | 48 | 88 | 44 | - |
| $\text{H}_2/\text{H}_2\text{O}/\text{CO}/\text{CO}_2/\text{N}_2$ | 30/ 15/ 5/ 10/ 40 | | 25/ 25/ 0/ 0/ 50 | | mol% |

The 100-tube purifier unit was built using the same composite membrane described in chapter 4 but with longer tube lengths (~30”, or 0.762 m).

Since the H₂-based inlet Peclet numbers ($Pe_{H_2} = \frac{v \cdot d_{hyd}}{D_{mix,H_2}} = \frac{\dot{m}_{in} \cdot d_{hyd}}{\rho_{in} A_{flow} D_{mix,H_2}}$) are sufficiently high (> 100) at all operating conditions, axial diffusion can be neglected, and a plug flow model is assumed. With this assumption, the species conservation equation for $Y_{k,ch}$ can be written as shown below:

$$\frac{d(\rho_{ch} Y_{k,ch})}{dt} = - \frac{d(\rho_{ch} Y_{k,ch} v_{ch})}{dx} + \frac{A_{int}}{A_{flow}} j_{k,int}$$

$$\Rightarrow \rho_{ch} \frac{dY_{k,ch}}{dt} + Y_{k,ch} \frac{d\rho_{ch}}{dt} = - \frac{d(\rho_{ch} Y_{k,ch})}{dx} + \frac{A_{int}}{A_{flow}} j_{k,int}$$

A_{flow} is the flow area, and is equivalent to $\frac{\pi d_{hyd}^2}{4}$, where d_{hyd} represents the hydraulic diameter. For a finite length Δx of each segment along the length of the purifier, with incoming convective flow labeled “in” and outgoing convective flow labeled “out”, the above equation can be written in terms of flow velocity v as below:

$$\rho_{ch} \frac{dY_{k,ch}}{dt} + Y_{k,ch} \frac{\rho_{in} v_{in} - \rho_{out} v_{out}}{\Delta x} + Y_{k,ch} \frac{A_{int}}{A_{flow}} \frac{\sum j_{k,int}}{\Delta x}$$

$$= \frac{Y_{k,in} \rho_{in} v_{in} - Y_{k,out} \rho_{out} v_{out}}{\Delta x} + \frac{A_{int}}{A_{flow}} \frac{j_{k,int}}{\Delta x}$$

Assuming plug flow as discussed above with “up”-wind differencing, $Y_{k,out} \approx Y_{k,ch}$, and $Y_{k,in} \approx Y_{k,up}$. The expression can then be written in terms of state space variables as equation (6.1).

$$\rho_{ch} \frac{dY_{k,ch}}{dt} = \frac{1}{\Delta x} \left[\underbrace{\frac{\dot{m}_{ch,up}}{A_{flow}} (Y_{k,ch,up} - Y_{k,ch})}_{\text{convective term}} - \underbrace{\frac{A_{int}}{A_{flow}} \left(j_{k,int} - Y_{k,ch} \sum_{l=1}^K j_{l,int} \right)}_{\text{chemical production term}} \right] \quad (6.1)$$

The “interface” in equation (6.1) can be either the Pd membrane on the reformate side, or the porous support on the sweep side. The gas properties very near this interface differ from those of the channel average, mainly due to mass transfer resistance of the gas layer. This boundary layer effect can be approximated in a quasi-1D model by using a Sherwood number in equation (6.2).

$$j_{k,int} = \frac{Sh_k D_{k,mix}}{d_{hyd}} (\rho_{ch} Y_{k,ch} - \rho_{int} Y_{k,int}) \quad (6.2)$$

The species-specific Sherwood number for internal laminar flow can be approximated using the correlation as a function of distance from flow entrance x as shown in equation (6.3).

$$\text{Sh}_k \approx 2.845 + 37.64[1000x^*]^{-0.35} \cdot \exp(-21.57x^*)$$

$$x^* = \frac{x}{d_{hyd} \text{Pe}_k} \quad (6.3)$$

$$\text{Pe}_k = \frac{\dot{m} \cdot d_{hyd}}{\rho A_{flow} D_{k,mix}}$$

When the interface is a Pd membrane surface, the mass flux vector $j_{k,int}$ equals the gas production rate at the Pd surface (see equation (3.5)). When the interface is a porous support, $j_{k,int}$ is calculated from the dusty gas model (equation (6.2)).

$$\begin{aligned} j_{k,int} &= -\dot{s}_{k,gas} W t_k \quad (\text{for Pd surface}) \\ j_{k,int} &= j_{k,DGM} \quad (\text{for porous support}) \end{aligned} \quad (6.4)$$

Equations (6.2) and (6.4) form a system of algebraic equations that must be true at all times t . The overall mass continuity for a segment can be written as equation (6.5), where m_{ch} is the mass of gas in the channel segment. An incompressible flow assumption is implicit in this equation.

$$\dot{m}_{ch} = \dot{m}_{ch,up} - A_{int} \sum j_{k,int} - m_{ch} \frac{d(\ln \rho_{ch})}{dt} \quad (6.5)$$

Using ideal gas law $\rho_{ch} = P_{ch} W_{t_{ch}} / RT_{ch}$, ρ_{ch} is affected by changes in composition $Y_{k,ch}$, temperature T_{ch} and pressure P_{ch} . However, for an isothermal incompressible fluid (where pressure is equalized instantaneously, $dT/dt = dP/dt = 0$). Hence, $d(\ln \rho_{ch})/dt$ can be written as in equation (6.6).

$$\frac{d(\ln \rho_{ch})}{dt} = \frac{\sum_{k=1}^K \frac{dY_{k,ch}}{dt} \frac{1}{Wt_k}}{\sum_{k=1}^K Y_{k,ch} \frac{1}{Wt_k}} \quad (6.6)$$

The hydraulic pressure drop due to viscous drag at the walls of the tube is calculated by assuming a laminar fully developed boundary layer in the flow channels (equation (6.7)).

$$P_{ch} = P_{ch,up} - \frac{32\mu_{ch}(\Delta x)\dot{m}_{ch}}{\rho_{ch}^2 d_{hyd}^2 A_{flow}} \quad (6.7)$$

6.3 Numerical solution

In the system of equations formed by (3.6), (3.7), (4.1), (6.1), (6.2), (6.4), (6.5) and (6.7), equations (6.2), (6.4), (6.5) and (6.7) corresponding to variables $Y_{k,int}$, \dot{m}_{ch} and P_{ch} are algebraic, while the others are ordinary differential equations. Hence, a differential algebraic equation (DAE) solver is needed to solve this system of equations. In general, in a DAE system, the state space vector $\{y\}$ can be divided into two distinct groups: differential variables $\{y_1\}$ and algebraic variables $\{y_2\}$. The

system of equations can be written in the form shown in equation (6.8) (p are the set of physical parameters needed for the governing equations).

$$\frac{d\{y_1\}}{dt} = f(t, \{y_1\}, \{y_2\}, p) \quad (6.8)$$

$$0 = g(t, \{y_1\}, \{y_2\}, p)$$

When the a DAE system is of index 1, the above equation can be simplified and written in matrix form as shown in equation (6.9) ([132]).

$$[M] \frac{d\{y\}}{dt} = f'(t, \{y\}, c) \quad (6.9)$$

Here, $[M]$ is called the mass matrix. $[M]$ is an identity matrix for a system of ordinary differential equations (ODE). For DAE systems, the 1s on the diagonal are replaced by 0s for rows corresponding to algebraic equations. Of the available DAE solvers in the Matlab *ode* suite, only stiff solver *ode15s* is suited for this system because of the disparity in time constants associated with surface reactions and channel flows, resulting in a very stiff system of equations.

However, there are significant challenges to solving this system of equations with *ode15s*, particularly pertaining to initial conditions and system stiffness. Although it is mathematically sufficient to define a set of consistent initial conditions for a DAE

problem (consistency at $t = 0$ implies $g(0, \{y_1(0)\}, \{y_2(0)\}, c) = \{0\}$), it is found that *ode15s* is unable to integrate with all sets of consistent initial conditions. After much trial and error, the following strategy is adopted. First, state space variables in the reformate and sweep channels are set to be uniform at the respective inlet conditions of that stream. The gases at the interface and in the porous support are assumed to be in equilibrium with the gas in the channels, and hence have the same properties as the channel gas. The Pd metallic membrane flux is cut off by temporarily setting $D_{H,\infty} = 0$. The Pd surface coverages are equilibrated with the fixed gas composition such that $d\theta_k/dt$ is minimized at the given gas conditions (using an equilibration function in Cantera). Since the H flux through the Pd metal is cut-off, $dX_{H,bulk}/dt = 0$ near both surfaces. The channel hydraulic pressure drop is also temporarily set to 0.

This initialization ensures that the Pd surface, Pd surface and bulk, porous support and the channel are in equilibrium on both sides of the Pd membrane, and that there is no net gain or loss of mass flux along either channel. This satisfies the algebraic equations $g(t, \{y_1\}, \{y_2\}) = \{0\}$ at $t = 0$. To further reduce transients near $t = 0$, the surface reaction rates are artificially slowed down by a factor of 10^3 . The interface variables $Y_{k,int}$ are removed from the set of variables directly solved for by *ode15s*. Instead, equations (6.2) and (6.4) are solved “locally” by the Matlab solver *fsolve*, each time the residual calculator function is called by the main function *ode15s*.

With these special conditions, *ode15s* is able to start integration. After integrating to “steady state” ($t = 1000$), the final solution is used as the initial condition for the next

run, in which the $D_{H,\infty}$ is restored to its original value. This process is repeated until all the special conditions above are relaxed, one after the other. The surface reaction rate is the last special condition to be relaxed, and is increased by a factor 5 each time, until the original rate is restored.

Although physical phenomena with very low time constants are captured well near $t = 0$ using the strategy outlined above, these phenomenon are “skipped” by the solver at higher t . This is mainly because the Matlab solver does not calculate the system Jacobian at every time step. This causes it to “jump” over some time intervals at which important surface changes are taking place because of convection-induced changes in the bulk gas composition. Ultimately, this leads to numerical failure at large t , when the solver must take time steps Δt smaller than $\text{eps}(t)$ to proceed (a computer can distinguish a number t from another number $t+\Delta t$ only if $\Delta t > \text{eps}(t)$). Since $\text{eps}(t)$ increases with t , the ability of the solver to take smaller time steps becomes more restricted at larger t . To solve this problem, the maximum allowable integration time step (*MaxStimeStep* in *ode15s* options) Δt_{\max} is adjusted to 10^{-4} .

With this constraint, although the solver runs reliably, the integration speed is severely reduced at higher t . To solve this problem, *ode15s* is modified as shown in Table 6.2. The maximum time step Δt_{\max} depends, in addition to the constraints imposed by *ode15s* $\Delta t_{\max\text{-ode15s}}$, on an absolute number $\Delta t_{\max,\text{abs}}$ and a relative number t/T_{factor} .

Other factors that influence the reliability and speed of integration include the initial time step ‘*InitialStep*’, relative and absolute tolerances ‘*AbsTol*’ and ‘*RelTol*’. User-specified Jacobian pattern “*JPattern*” greatly speeds the integration, and is faster by at least 10 times, as compared with allowing *ode15s* to calculate both the Jacobian pattern and the numerical Jacobian. Specifying a *tspan* vector allows storage of the solution vector only at times indicated in *tspan*, thereby saving memory. All the above options and modifications are summarized in Table 6.2.

Table 6.2: Modifications and selected options for *ode15s*

| <i>ode15s</i> <i>parameter</i> | <i>value</i> | <i>units</i> |
|-----------------------------------|---|--------------|
| $\Delta t_{\max}(t > 0)$ | $\max(\min(\Delta t_{\max\text{-ode15s}}, \Delta t_{\max\text{-abs}}, t/ T_{\text{factor}}), \text{eps}(t))$ | s |
| $\Delta t_{\max\text{-abs}}$ | 1 | s |
| T_{factor} | 10 | s |
| <i>RelTol</i> | 10^{-6} | - |
| <i>AbsTol</i> | 10^{-6} | - |
| <i>InitialStep</i> | 10^{-12} | s |
| <i>tspan</i> | [0; <i>logspace</i> (-12, 3, 30)] | s |
| <i>JPattern</i> | user specified; sparse matrix of 1s corresponding to non-zero Jacobian values | - |

6.4 Experiment

The experimental setup is similar to the one used for pure-H₂ composite membrane tests described in chapter 4 (see page 86). However, changes are required in order to include CO and H₂O on the reformate side and H₂ on the sweep side. The modified experimental setup is shown in Figure .

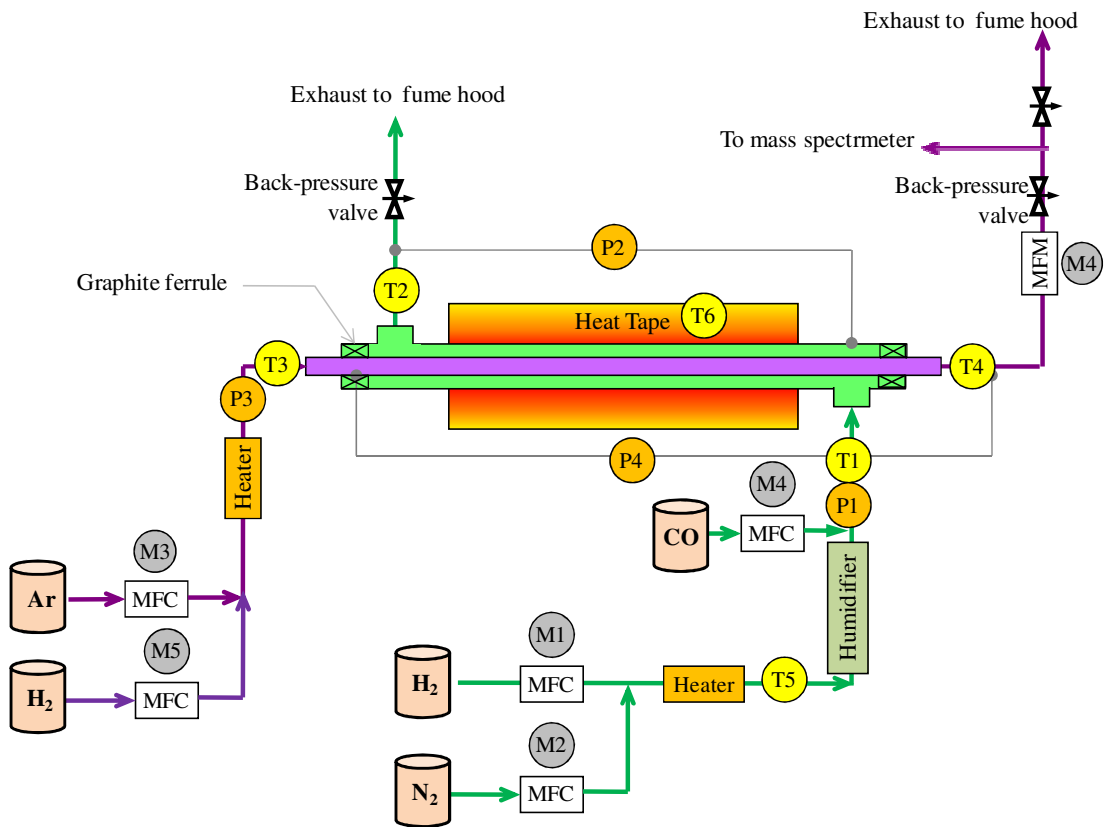


Figure 6.2: Experimental test setup for counter-current gas flow experiments on composite membrane assembly

Two additional mass flow controllers M4 and M5 are used to meter CO on the reformat side and H₂ on the sweep side respectively. A humidifier is used to introduce H₂O into the reformat stream. The humidifier saturates the flow at a preset temperature, which can be adjusted and monitored with the help of an embedded heater and a T-type thermocouple at the gas-exit. The amount of H₂O in the reformat stream can be controlled by adjusting the exit temperature of the humidifier. The CO is added downstream of the humidifier to avoid water-gas shift reactions on the red-hot heater filament and to avoid fouling of the Nafion membranes in the humidifier.

The sweep exhaust is analyzed using a magnetic sector mass spectrometer (Prima δ B, Thermo Fisher Scientific). Since the inlet compositions of both streams are known, the H₂ transfer efficiency can be calculated from the sweep exhaust composition. The mass spectrometer measurements are the chief source of uncertainty in measurements (+/- 2% point).

The same composite membrane described in chapter 4 is used for the counter-current gas flow experiments. As in the pure H₂ experiments, the high-temperature experiments are carried out first, and any temperature changes are introduced slowly in the absence of H₂. This ensures the integrity of the composite membrane. Pressure is regulated through two back-pressure valves located at the exit of each stream.

For each experimental run, the MFC commands are set and the flows are allowed to stabilize. The back-pressure valves are simultaneously adjusted to pre-determined pressure values. After stabilization of the pressures, sweep exhaust composition is measured with a magnetic sector mass spectrometer. Because the composition of gases entering the sweep side is known, the exhaust composition can be used to calculate the net H₂ transfer from reformat to sweep side.

To maintain similar Reynolds and Peclet numbers as the 100-tube purifier unit described earlier in this chapter, the flow rates for the single-tube experiments are set at $250/100 = 2.5$ slpm reformat flow and $40/100 = 0.40$ slpm (or 400 sccm) sweep flow at full power. The same length of the test section described in chapter 4 is used

(8.75”/ 0.223 m) to minimize non-uniformity in temperature along the tube. Properties of flows entering the single-tube membrane assembly are shown in Table 6.3. Ar is used instead of N₂ in the sweep stream so that the sweep exhaust can be monitored for N₂ leakage at all times.

Table 6.3: Composition and flow rate of gases entering single-tube membrane assembly in experimental test rig (active length of tube = 0.223 m)

| <i>parameter</i> | <i>reformat</i> | | <i>sweep</i> | | <i>units/ remarks</i> |
|---|---------------------|---------------|--------------------|---------------|---------------------------|
| | full power | half power | full power | half power | |
| <i>m</i> | 2500 | 1400 | 400 | 200 | sccm |
| Pe_{H2} | 1270 | 635 | 900 | 450 | at 350 °C |
| Re | 97 | 48 | 88 | 44 | at 350 °C |
| H ₂ /H ₂ O/CO/CO ₂ /N ₂ /Ar | 30/ 15/ 5/ 10/ 40/0 | | 25/ 0/ 0/ 0/ 0/ 75 | | mol% nominal |

6.5 Results and discussion

6.5.1 H₂ + N₂/ Ar gas tests

Experiments and model runs are carried out at ”full power” and “half power” conditions to determine the effect of H₂ partial pressure in the reformat and sweep streams on the H₂ recovery fraction. Figure shows the effect of entry H₂ partial pressure in the reformat stream; model results predict the trends in experiments well. At these conditions, the H₂ recovery fraction increases with H₂ partial pressure. This is mainly because the H₂ partial pressure driving force is higher near the exit of the reformat side, where the incoming sweep flow is maintained constant. This is further

illustrated by Figure where the H-chemical potential μ_{H} is plotted along the channel at various locations through the composite membrane for the full power condition. It can be seen from the figures that the chief resistance to H_2 permeation from the reformat to the sweep side is the porous support resistance. Under these conditions, flow effects become less important, and the H_2 flux at a given location depends mainly on the available H_2 driving force. Since this average driving force is higher for the 35% inlet reformat H_2 case, the recovery fraction is also higher. Also, since flow effects are less important, lower flow rates result in higher recovery fractions. However, this is expected to change when the residence time of gases in the purifier increases in longer tubes.

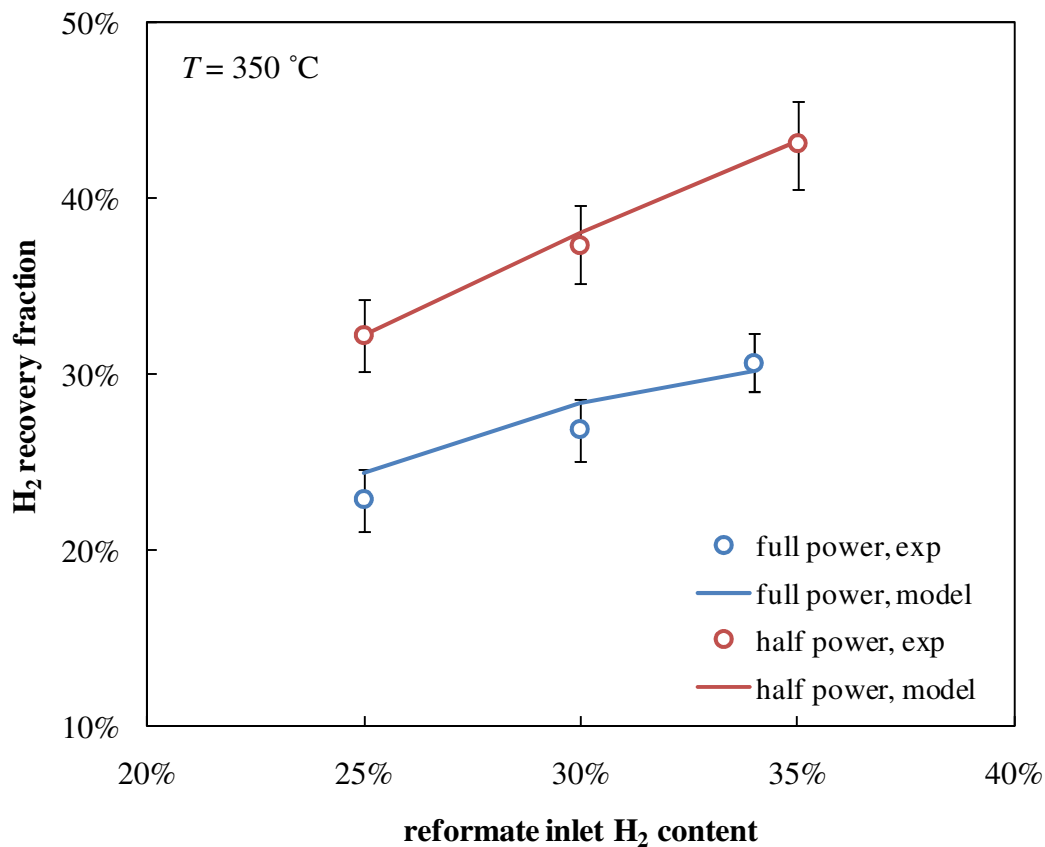


Figure 6.3: Effect of reformate H₂ partial pressure on H₂ recovery fraction. Reformate inlet conditions are $P = 379$ kPa, 2500 sccm 5 kWe/ 1400 sccm at 2.5 kWe, H₂ as shown/ N₂ balance. Sweep inlet conditions are $P = 137$ kPa, 400 sccm 5 kWe/ 200 sccm 2.5 kWe, H₂/ Ar = 25/75 mol%

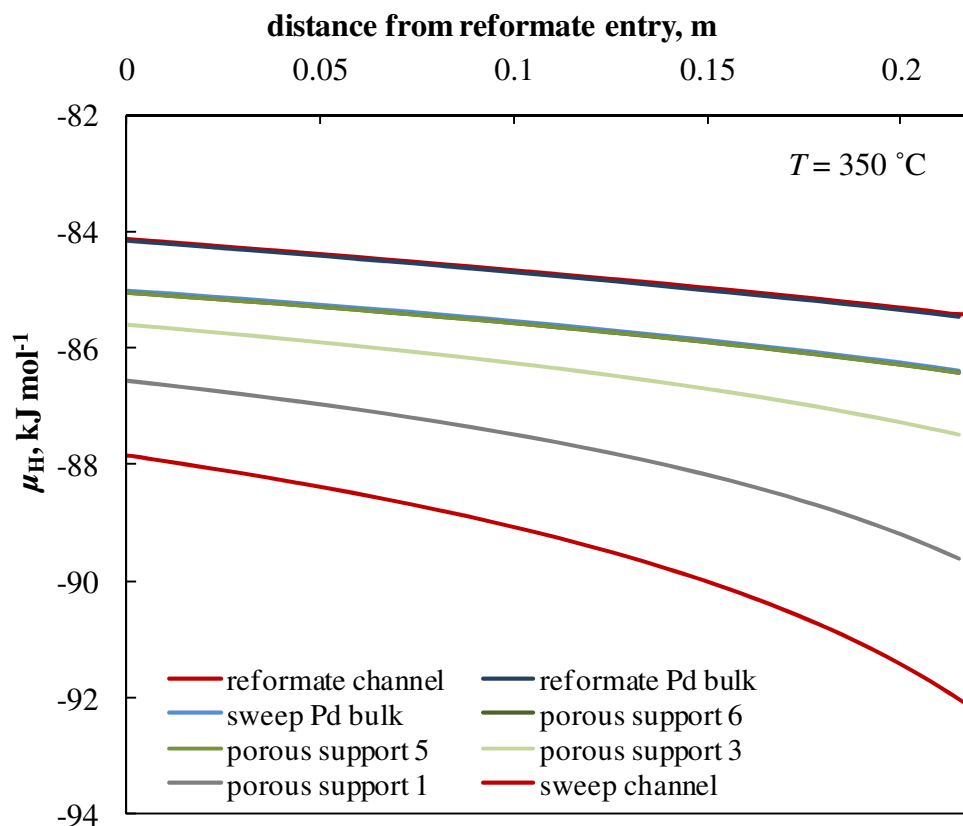


Figure 6.4: H-chemical potential at various locations along the length of the composite membrane purifier. $T = 350\text{ }^{\circ}\text{C}$; Reformate side: $P_{\text{reformate}} = 379\text{ kPa}$, total inlet flow = 2500 sccm, inlet $\text{H}_2/\text{N}_2 = 34/66\text{ mol}\%$; Sweep side: $P_{\text{sweep}} = 137\text{ kPa}$, total inlet flow = 400 sccm, inlet $\text{H}_2/\text{Ar} = 25/75\text{ mol}\%$

Similarly, the inlet H_2 partial pressure in the sweep is also varied. As expected, the H_2 recovery fraction variation decreases with changes in inlet H_2 partial pressure on the sweep side (shown in Figure). The model results track the trends in experiments well.

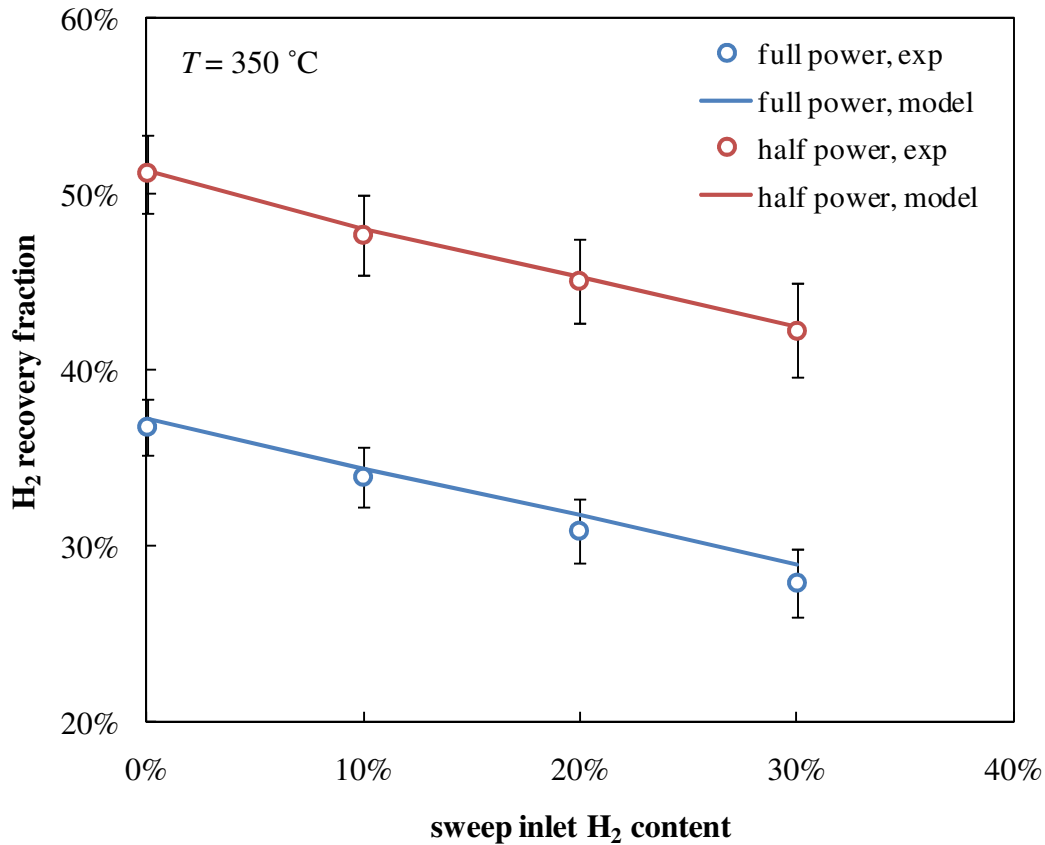


Figure 6.5: Effect of sweep H₂ partial pressure on H₂ recovery fraction. Reformate inlet conditions are $P = 379$ kPa, 2500 sccm 5 kWe/ 1400 sccm at 2.5 kWe, H₂ / N₂ = 34/66. Sweep inlet conditions are $P = 137$ kPa, 400 sccm at 5 kWe/ 200 sccm at 2.5 kWe, H₂ as shown/ Ar balance

Model results also compare well with experimental trends at 250 °C (Figure). The H-chemical potentials at various locations in the composite membrane purifier at this temperature are plotted in Figure 6.7. As can be seen from the two figures, the same arguments discussed for $T = 350$ °C condition hold at the lower temperature. Although bulk diffusion through the membrane contribute a larger fraction of the flow resistance than at 350 °C, the chief resistance is still the porous substrate.

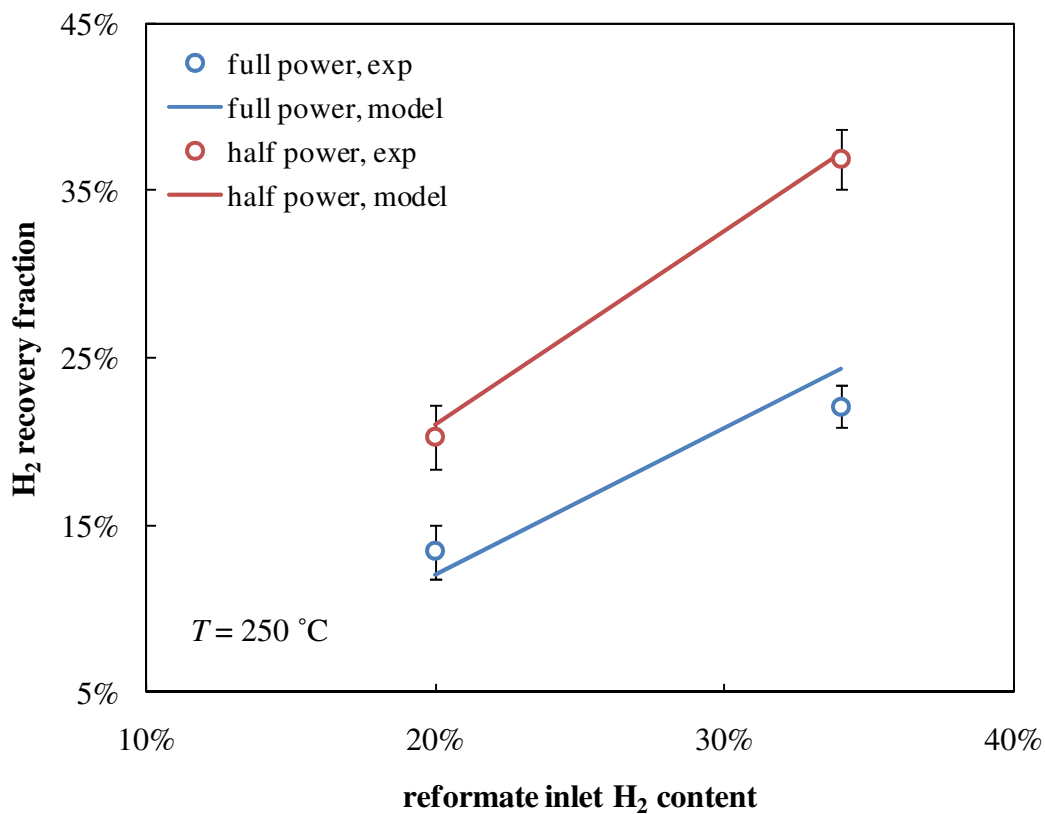


Figure 6.6: Effect of reformate H₂ partial pressure on H₂ recovery fraction. Reformate inlet conditions are $P = 379$ kPa, 2500 sccm at 5 kWe/ 1400 sccm at 2.5 kWe, H₂ as shown/ N₂ balance. Sweep inlet conditions are $P = 137$ kPa, 400 sccm 5 kWe/ 200 sccm 2.5 kWe, H₂/ Ar = 25/75 mol%

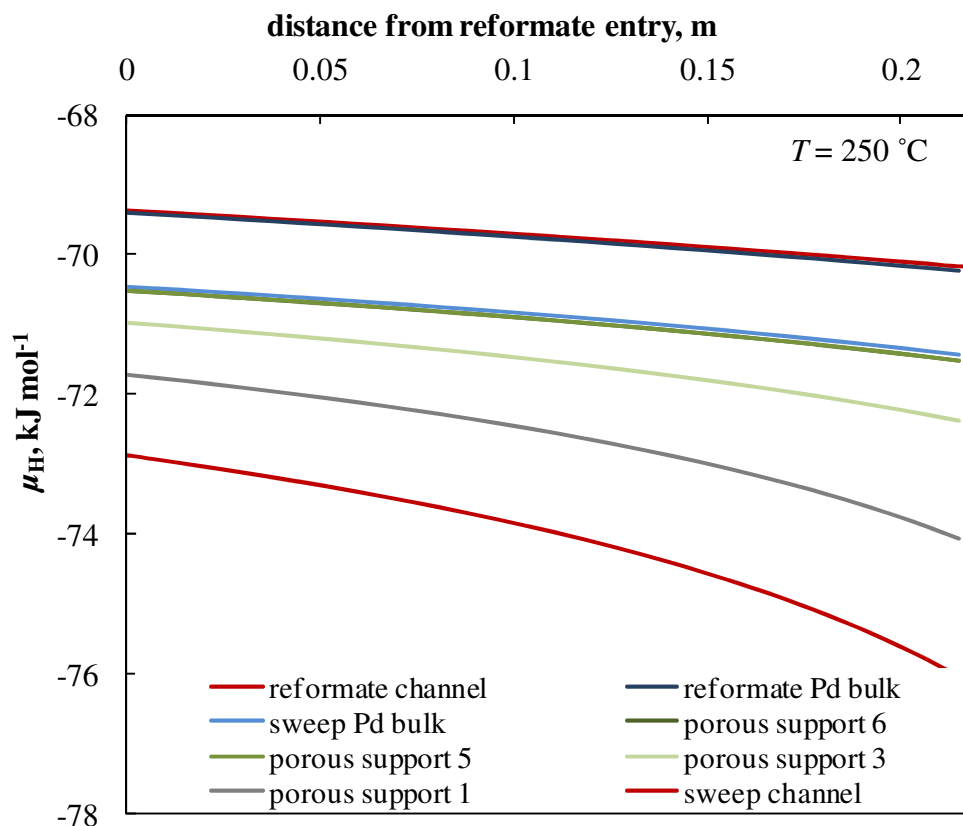


Figure 6.7: H-chemical potential at various locations along the length of the composite membrane purifier. $T = 250\text{ }^{\circ}\text{C}$; Reformat side: $P_{\text{reformat}} = 379\text{ kPa}$, total inlet flow = 2500 sccm, inlet $\text{H}_2/\text{N}_2 = 34/66\text{ mol}\%$; Sweep side: $P_{\text{sweep}} = 137\text{ kPa}$, total inlet flow = 400 sccm, inlet $\text{H}_2/\text{Ar} = 20/80\text{ mol}\%$

Since the model results track experimental results at both 250 and 350 °C implies that the rate limiting processes have been captured with sufficient accuracy at these T and P range.

6.5.2 CO poisoning studies

To check the efficacy of the CO-poisoning model, experiments are conducted at 250, 300 and 350 °C. It can be seen from Figure that CO poisoning effects are more pronounced at lower temperatures, and are mitigated at temperatures above 300 °C

Model results compare well with experimental results. This further proves that that the H₂/ CO competitive adsorption on the Pd surface has been captured with sufficient accuracy with the model.

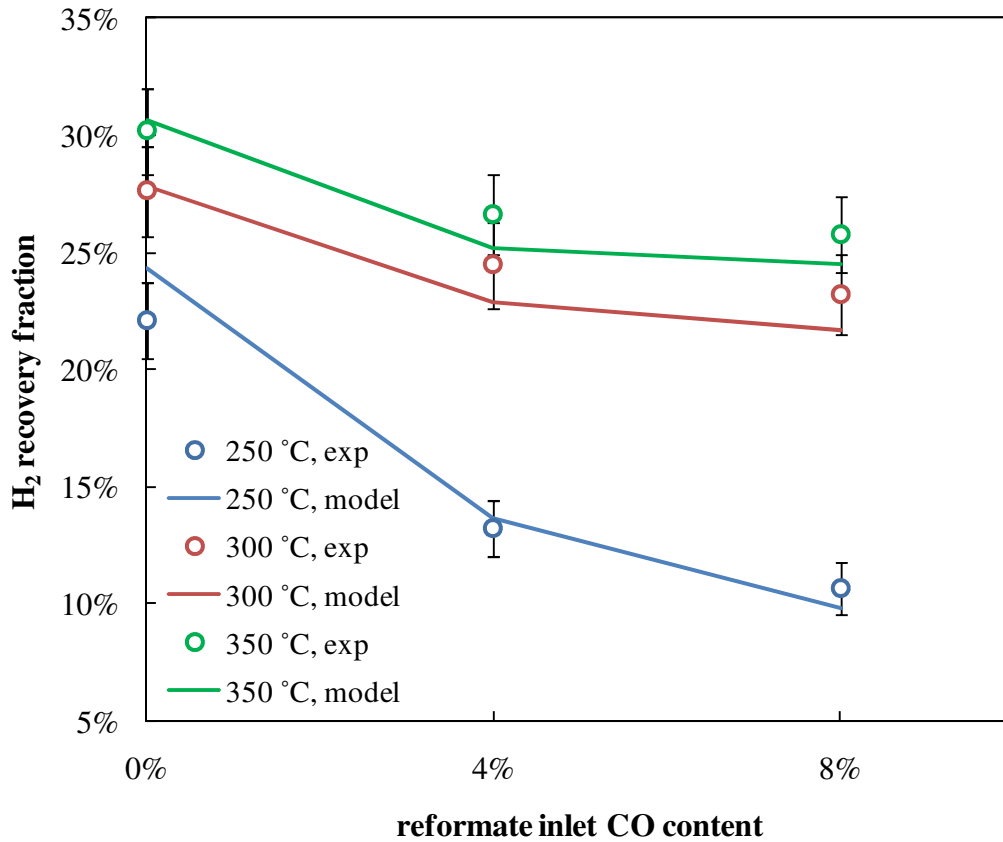


Figure 6.8: CO poisoning of Pd surfaces: comparison of 2-D model results with counter-current gas flow experiments on Pd composite membranes at various temperatures. Reformate conditions: $P_{\text{reformate}} = 379$ kPa, total inlet flow 2500 sccm (34% H₂, CO as indicated, N₂ balance). Sweep side: $P_{\text{sweep}} = 137$ kPa, total inlet flow 400 sccm (25% H₂, balance Ar).

A chemical potential plot (Figure) for the 8% inlet CO case at $T = 250$ °C further illustrates the relative importance of surface poisoning at lower temperatures.

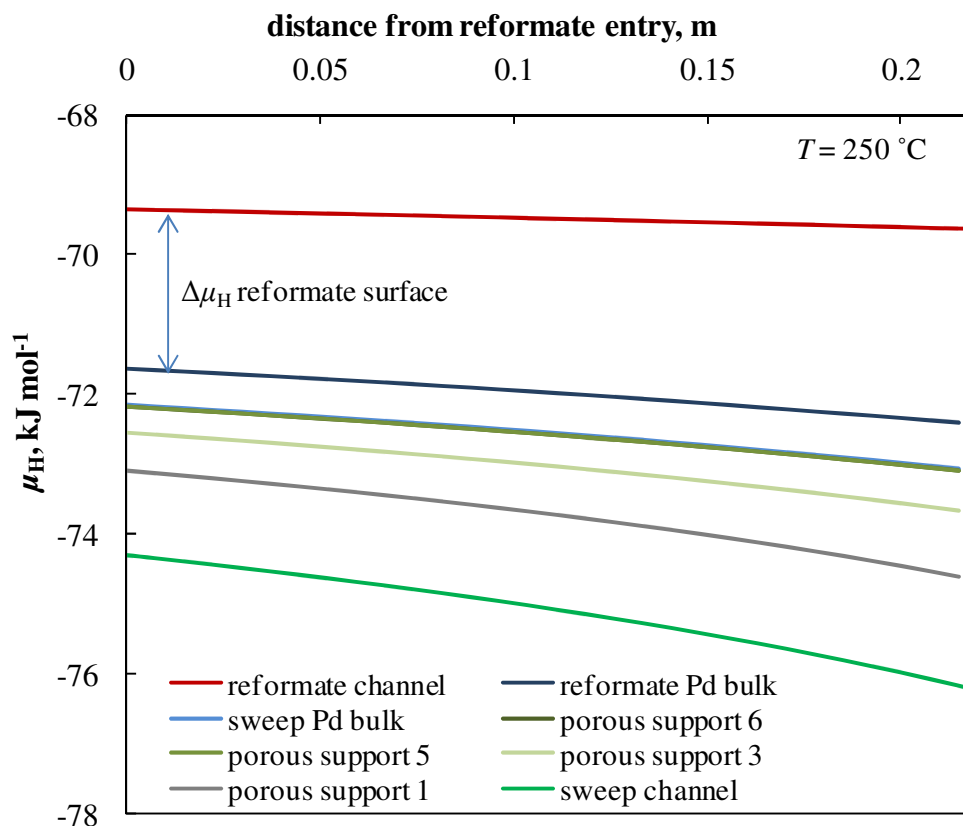


Figure 6.9: CO poisoning effect: Hydrogen chemical potential μ_{H} at various locations along the length of the purifier and through the composite membrane. Reformate conditions: $P_{\text{reformate}} = 379$ kPa, total flow 2500 sccm (34% H_2 , 8% CO, balance N_2). Sweep conditions: $P_{\text{sweep}} = 137$ kPa, total flow 400 sccm (25% H_2 , balance Ar).

6.5.3 H_2O poisoning studies

Experiments are carried out with humidified reformate streams to compare model results. Figure shows this comparison. The model over-predicts the poisoning effect of H_2O on Pd surfaces. However, some recent experiments carried out with the help of Gibbons et al suggest that the poisoning effect of steam is gradual. Over the course of approximately 20 minutes, the H_2 flux through a composite membrane similar in construction to the one used in the current study dropped by $\sim 35\%$ at 250°C (the membrane thickness of this composite membrane is not yet confirmed [133]).

Although these H₂O poisoning experiments remain inconclusive, the longer time scales involved suggest that the poisoning mechanism involves sub-surface species in addition to surface species, as suggested by previous studies on H₂ combustion on Pd nano-particles [121, 130]. Therefore, more detailed microkinetic models that allow reactions involving sub-surface species such as O(sb) and OH(sb) along with further experimental validation is needed to model the observed H₂O poisoning effects. For the present study, model results are only validated against experimental results in the literature, as shown in chapter 6. With the present model, the poisoning effect of H₂O (with the current model) is better visualized as a drop in chemical potential across the reformate side Pd-surface (shown in Figure).

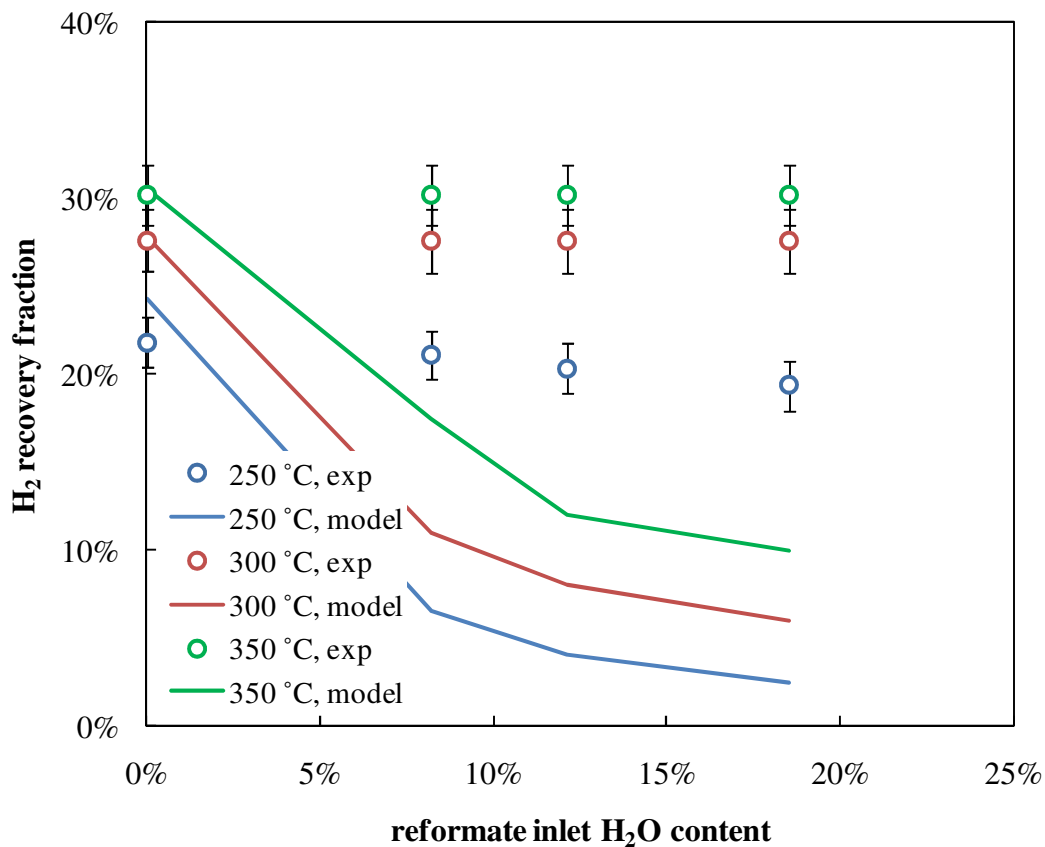


Figure 6.10: H₂O poisoning of Pd surfaces: comparison of 2-D model results with counter-current gas flow experiments on a Pd composite membrane at various temperatures. Reformate conditions: $P_{\text{reformate}} = 379$ kPa, total inlet flow 2500 sccm (34% H₂, H₂O as indicated, N₂ balance). Sweep side: $P_{\text{sweep}} = 137$ kPa, total inlet flow 400 sccm (25% H₂, balance Ar).

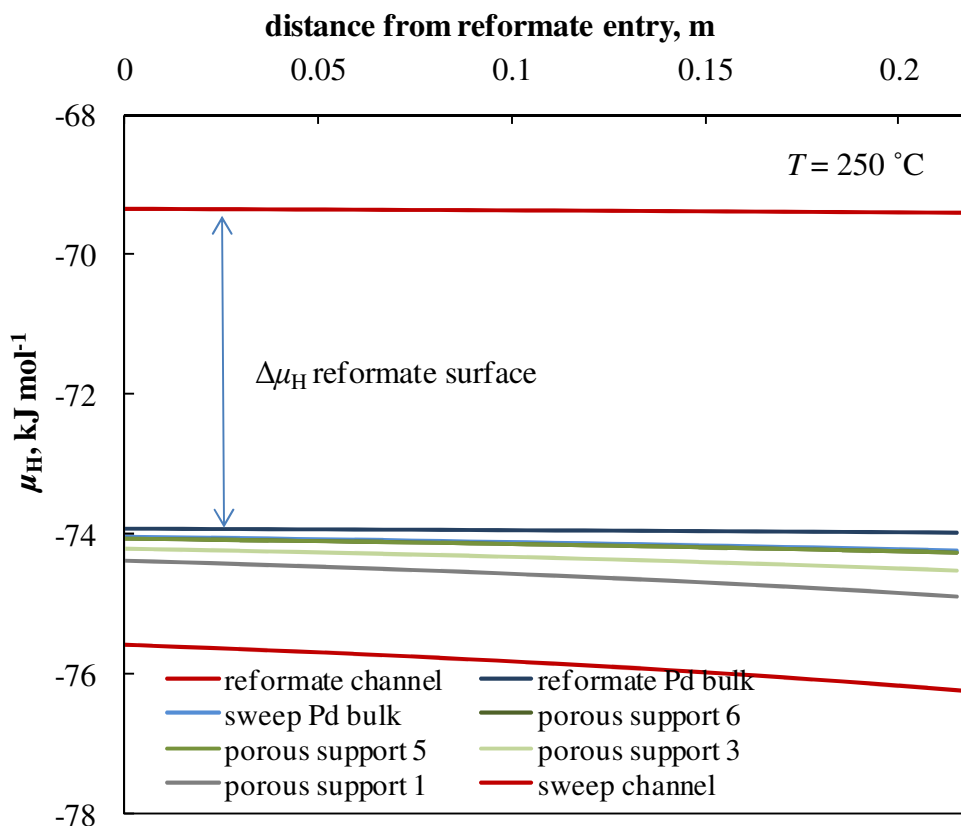


Figure 6.11: H₂O poisoning effect: Hydrogen chemical potential μ_{H} at various locations along the length of the purifier and through the composite membrane. Reformate conditions: $P_{\text{reformat}} = 379$ kPa, total flow 2500 sccm (34% H₂, 18% H₂O, balance N₂). Sweep conditions: $P_{\text{sweep}} = 137$ kPa, total flow 400 sccm (25% H₂, balance Ar)

6.6 Summary

The 1-D through-the-membrane Pd-H₂/CO/H₂O interaction model developed in chapters 3 through 5 is integrated into a down-the-channel membrane purifier flow model. Matlab DAE solver *ode15s* is critically modified to handle the additional stiffness due to the disparity among the time constants for various physical phenomena involved. This validated model can now be used to carry out design and optimization studies.

Chapter 7: Conclusions

7.1 Research Summary

Realizing trade-offs involved in the design and operation of a liquid-hydrocarbon fueled low-temperature PEMFC system shows the importance of effective H₂ purification. Model results have established that H₂ recovery fraction $\geq 75\%$ of a membrane based purifier in such a system is critical to achieve system efficiencies approaching 30% [15]. H₂ recovery fraction also strongly affects water balance and thermal management. Therefore, the careful design and operation of membrane purifiers is necessary.

To understand the performance of Pd membranes, a new microkinetic model for pure Pd and Pd-alloy-H₂ interactions is presented. This model is an improvement over existing Sievert's law based reactor design equations since it allows for non-ideal thermodynamics of H solutions in Pd alloys. Fundamental experiments and DFT studies in the literature are used to estimate critical parameters in this model. Pd and Pd_{0.77}Ag_{0.23} thermokinetics for H are validated with experiments on free-standing membranes in the literature. To accurately predict H₂ diffusion through a Pd alloy membrane, the model must predict the equilibrium solubility of H in the Pd alloy; and this necessarily involved the use of non-ideal thermodynamics as presented in the model.

The Pd-H₂ interaction model is combined with a porous media transport model to build a Pd composite membrane model. This composite membrane model is validated with experiments with pure H₂ on an industrial Pd-ceramic composite membrane. Surface reactions for CO and H₂O are adapted from the literature and added to the Pd-H₂ microkinetic model to allow for competitive adsorption by these other gases that are present in any hydrocarbon reformat gas on the Pd surface. This 1-D “through-the-membrane” model is validated with experiments in the literature.

The membrane model is integrated with a quasi-1-D channel flow model to build a comprehensive membrane purifier model, which is validated with counter-current gas flow experiments that are conducted on the same industrial composite membrane. This validated down-the-channel model can be used to carry out design optimization studies.

7.2 Contributions to the literature

The system level model results has quantified trade-offs associated with liquid hydrocarbon-fueled PEMFC system. The system model has underscored the need for modeling complex systems in order to establish bounds on component performance requirements. The results presented here are part of a research paper published [15], and presented at the Electrochemical Society Meeting [16]. This work aids the design and development of liquid-hydrocarbon fueled PEMFC systems.

An improved microkinetic model for Pd-alloy-H₂ interactions has been presented, and a systematic procedure to derive these parameters for Pd alloys has been described. This procedure can now be used to calculate parameters for other alloys that are being used, or are being developed for the future. As an example, these parameters have been calculated for the first time for the Pd_{0.77}Ag_{0.23} alloy, and published[115].

The validated Pd-H₂ composite membrane model has recently been published [134]. This model has quantified the contribution of the porous support to the overall resistance at various operating conditions for the first time. This is expected to stimulate design and manufacturing improvements that lead to higher permeance supports for Pd membrane applications.

The CO-H₂O competitive adsorption mechanism and the 2-D model results are also expected to be published in research journals in the near future. Matlab *ode15s* has been modified to handle more stiff DAE systems of equations, particularly reacting flow phenomena.

7.3 Recommendations for Future Research

As discussed in chapters 2 and 5, alloying Pd with Au is expected to improve the thermal cycling capability of the metallic film in the presence of H₂ by lowering the α - α + β transition temperature. This would help in minimizing the use of electric heaters that are needed start-up and shut down the current Pd purifier. Current challenges to depositing a Pd/ Au alloy include uncertainty in alloy composition

arising from uncertainties in Pd and Au thicknesses prior to annealing, and the alloying process itself.

Currently, the Pd-ceramic composite membrane is able to withstand pressure in one direction only. If the metallic foil is able to retain mechanical integrity when a higher pressure is applied on the ceramic support side, then the porous support can be used as an anchor for a water-gas shift catalyst. The reformat gases would then be introduced on the support side, and sweep gases would be on the Pd side. This is expected to reduce the total required membrane area by taking advantage of the shifting equilibrium as H_2 is selectively removed along the purifier.

Much trial and error and algorithm modifications were needed to solve this stiff DAE system using *ode15s*. in spite of these changes, the solver is unable to produce quick and reliable results, thereby making it challenging to be incorporated as part of a larger optimization study. Therefore, it is recommended to conduct a search for better DAE solvers. Although Matlab provides a convenient user interface and ease of programming, the use of a more efficient and/ or stiff solver would result in faster and more reliable results than the current *ode15s* solver used in this study. For this reason, it is recommended to carry out a speed and reliability analysis of the most popular stiff DAE solvers using the membrane model as a benchmark.

Bibliography

- [1] A.K. Avci, Z.I. Onsan, D.L. Trimm, On-board fuel conversion for hydrogen fuel cells: comparison of different fuels by computer simulations, *Applied Catalysis a-General* 216(1-2) (2001) 243-256.
- [2] R.L. Borup, M.A. Inbody, T.A. Semelsberger, J.I. Tafuya, D.R. Guidry, Fuel composition effects on transportation fuel cell reforming, *Catalysis Today* 99(3-4) (2005) 263-270.
- [3] T. Berning, N. Djilali, A 3D, multiphase, multicomponent model of the cathode and anode of a PEM fuel cell, *Journal of the Electrochemical Society* 150(12) (2003) A1589-A1598.
- [4] G.H. Guvelioglu, H.G. Stenger, Computational fluid dynamics modeling of polymer electrolyte membrane fuel cells, *Journal of Power Sources* 147(1-2) (2005) 95-106.
- [5] G.Y. Lin, W.S. He, T. Van Nguyen, Modeling liquid water effects in the gas diffusion and catalyst layers of the cathode of a PEM fuel cell, *Journal of the Electrochemical Society* 151(12) (2004) A1999-A2006.
- [6] B.R. Sivertsen, N. Djilali, CFD-based modelling of proton exchange membrane fuel cells, *Journal of Power Sources* 141(1) (2005) 65-78.
- [7] S. Um, C.Y. Wang, Computational study of water transport in proton exchange membrane fuel cells, *Journal of Power Sources* 156(2) (2006) 211-223.
- [8] S.R. Deshmukh, D.G. Vlachos, CFD simulations of coupled, countercurrent combustor/reformer microdevices for hydrogen production, *Industrial & Engineering Chemistry Research* 44(14) (2005) 4982-4992.
- [9] A.G. Norton, S.R. Deshmukh, E.D. Wetzel, D.G. Vlachos, Downsizing chemical processes for portable hydrogen production, in: Y. Wang, J.D. Holladay (Eds.), *Microreactor Technology and Process Intensification*, 2005. pp. 179-193.
- [10] D.G. Vlachos, D.G. Norton, S.R. Deshmukh, A.B. Mhadeshwar, Fuel processing at the microscale for portable fuel cells, *Abstracts of Papers of the American Chemical Society* 226 (2003) 038-CATL.

- [11] S. Tischer, O. Deutschmann, Recent advances in numerical modeling of catalytic monolith reactors, *Catalysis Today* 105(3-4) (2005) 407-413.
- [12] R.M. Biesheuvel, G.J. Kramer, Shortcut model for water-balanced operation in fuel processor fuel cell systems, *Journal of Power Sources* 138(1-2) (2004) 156-161.
- [13] S. Ahmed, J. Kopasz, R. Kumar, M. Krumpelt, Water balance in a polymer electrolyte fuel cell system, *Journal of Power Sources* 112(2) (2002) 519-530.
- [14] E.D. Doss, R. Kumar, R.K. Ahluwalia, M. Krumpelt, Fuel processors for automotive fuel cell systems: a parametric analysis, *Journal of Power Sources* 102(1-2) (2001) 1-15.
- [15] J.B. Pearlman, A. Bhargav, E.B. Shields, G.S. Jackson, P.L. Hearn, Modeling efficiency and water balance in PEM fuel cell systems with liquid fuel processing and hydrogen membranes, *Journal of Power Sources* 185(2) (2008) 1056-1065.
- [16] A. Bhargav, J.B. Pearlman, G.S. Palmer, E.B. Shields, S.-A.S. Reihani, G.S. Jackson, P.L. Hearn, **PEM fuel cell system modeling with liquid fuel processing and hydrogen membranes**, Proton Exchange Membrane Fuel Cells 6 - 210th Electrochemical Society Meeting, Cancun, Mexico, 2006. pp. 1139-1148.
- [17] G. Barbieri, A. Brunetti, T. Granato, P. Bernardo, E. Drioli, Engineering evaluations of a catalytic membrane reactor for the water gas shift reaction, *Industrial & Engineering Chemistry Research* 44(20) (2005) 7676-7683.
- [18] L. Barelli, G. Bidini, F. Gallorini, S. Servili, Hydrogen production through sorption-enhanced steam methane reforming and membrane technology: A review, *Energy* 33(4) (2008) 554-570.
- [19] A. Basile, F. Gallucci, L. Paturzo, A dense Pd/Ag membrane reactor for methanol steam reforming: Experimental study, *Journal of Power Sources* 104(2-4) (2005) 244-250.
- [20] A. Basile, F. Gallucci, L. Paturzo, Hydrogen production from methanol by oxidative steam reforming carried out in a membrane reactor, *Journal of Power Sources* 104(2-4) (2005) 251-259.
- [21] A. Brunetti, A. Caravella, G. Barbieri, E. Drioli, Simulation study of water gas shift reaction in a membrane reactor, *Journal of Membrane Science* 306(1-2) (2007) 329-340.

- [22] K.Y. Chang, W.H. Lin, H.F. Chang, Simulation of hydrogen production from dehydrogenation of ethanol in a palladium membrane reactor, *Journal Of The Chinese Institute Of Chemical Engineers* 33(3) (2002) 225-232.
- [23] Y.Z. Chen, H.Y. Xu, Y.Z. Wang, G.X. Xiong, Hydrogen production from the steam reforming of liquid hydrocarbons in membrane reactor, *Catalysis Today* 118(1-2) (2006) 136-143.
- [24] A.S. Damle, Hydrogen production by reforming of liquid hydrocarbons in a membrane reactor for portable power generation - Model simulations, *Journal of Power Sources* 180(1) (2008) 516-529.
- [25] C.M. Graciasalcedo, B.J. McBride, T.A. Brabbs, EXPERIMENTAL-VERIFICATION OF THE THERMODYNAMIC PROPERTIES FOR JET-A FUEL, *Abstracts of Papers of the American Chemical Society* 196 (1988) 108-FUEL.
- [26] P. Berg, K. Promislow, J. St Pierre, J. Stumper, B. Wetton, Water management in PEM fuel cells, *Journal of the Electrochemical Society* 151(3) (2004) A341-A353.
- [27] C. Tesluk, Water management in Ballard PEM fuel cell stacks: testing at University of Maryland, in: D.G. Jackson (Ed.), *College Park*, 2008.
- [28] J.E. Hu, J.B. Pearlman, A. Bhargava, G.S. Jackson, Impact of Increased Anode CO Tolerance on Performance of Hydrocarbon-Fueled PEM Fuel Cell Systems, *ASME 7th International Fuel Cell Science, Engineering & Technology Conference*, Newport Beach, CA, USA, 2008.
- [29] D.C. Calabro, R.D. Partridge, P.J. Berlowitz, B. Carstensen, H.W. Deckman, P.L. DaPrato, F. Hershkowitz, R.F. Socha, A dual functional staged hydrogen purifier for an integrated fuel processor-fuel cell power system, *Catalysis Today* 129(3-4) (2007) 380-390.
- [30] N.W. Ockwig, T.M. Nenoff, Membranes for hydrogen separation, *Chemical Reviews* 107(10) (2007) 4078-4110.
- [31] N. Itoh, Y. Kaneko, A. Igarashi, Efficient hydrogen production via methanol steam reforming by preventing back-permeation of hydrogen in a palladium membrane reactor, *Industrial & Engineering Chemistry Research* 41(19) (2002) 4702-4706.
- [32] M. Sjardin, K.J. Damen, A.P.C. Faaij, Techno-economic prospects of small-scale membrane reactors in a future hydrogen-fuelled transportation sector, *Energy* 31(14) (2006) 2523-2555.

- [33] W. Yu, T. Ohmori, T. Yamamoto, A. Endo, M. Nakaiwa, T. Hayakawa, N. Itoh, Simulation of a porous ceramic membrane reactor for hydrogen production, 30(10) (2005) 1071-1079.
- [34] P.L. Hearn, C. Tesluk, G.S. Jackson, A. Bhargava, Combined Anode Recirculation and Purifier Sweep Loop, in: I.d.f.w.U.o.M.O.o.T. Commercialization (Ed.), 2009.
- [35] Y.H. Ma, F. Guazzone, Metallic membranes for the separation of hydrogen at high temperatures, *Annales De Chimie-Science Des Materiaux* 32(2) (2007) 179-195.
- [36] A.A. Shah, P.C. Sui, G.S. Kim, S. Ye, A transient PEMFC model with CO poisoning and mitigation by O₂ bleeding and Ru-containing catalyst, *Journal of Power Sources* 166(1) (2007) 1-21.
- [37] A. Kulprathipanja, G.O. Alptekin, J.L. Falconer, J.D. Way, Pd and Pd-Cu membranes: inhibition of H₂ permeation by H₂S, *Journal of Membrane Science* 254(1-2) (2005) 49-62.
- [38] C.J. Smithells, C.E. Ransley, *The Diffusion of Gases Through Metals*, Proceedings of the Royal Society of London, The Royal Society, 1935. pp. 172-197.
- [39] G.L. Holleck, Diffusion And Solubility Of Hydrogen In Palladium And Palladium-Silver Alloys, *Journal Of Physical Chemistry* 74(3) (1970) 503-&.
- [40] C. Picard, O.J. Kleppa, G. Boureau, High-Temperature Thermodynamics Of The Solutions Of Hydrogen In Palladium-Silver Alloys, *Journal Of Chemical Physics* 70(6) (1979) 2710-2719.
- [41] T.L. Ward, T. Dao, Model of hydrogen permeation behavior in palladium membranes, *Journal of Membrane Science* 153(2) (1999) 211-231.
- [42] T.B. Flanagan, W.A. Oates, The Palladium-Hydrogen System, *Annual Review Of Materials Science* 21 (1991) 269-304.
- [43] A. Kulprathipanja, G.O. Alptekin, J.L. Falconer, J.D. Way, Effects of water gas shift gases on Pd-Cu alloy membrane surface morphology and separation properties, *Industrial & Engineering Chemistry Research* 43(15) (2004) 4188-4198.
- [44] A. Kulprathipanja, G.O. Alptekin, J.L. Falconer, J.D. Way, Pd and Pd-Cu membranes: inhibition of H₂ permeation by H₂S, 254(1-2) (2005) 49-62.

- [45] A.L. Mejdell, H. Klette, A. Ramachandran, A. Borg, R. Bredesen, Hydrogen permeation of thin, free-standing Pd/Ag_{23%} membranes before and after heat treatment in air, *Journal of Membrane Science* 307(1) (2008) 96-104.
- [46] A. Unemoto, A. Kaimai, K. Sato, T. Otake, K. Yashiro, J. Mizusaki, T. Kawada, T. Tsuneki, Y. Shirasaki, I. Yasuda, Surface reaction of hydrogen on a palladium alloy membrane under co-existence of H₂O, CO, CO₂ or CH₄, *International Journal Of Hydrogen Energy* 32(16) (2007) 4023-4029.
- [47] J. Okazaki, D.A.P. Tanaka, M.A.L. Tanco, Y. Wakui, T. Ikeda, F. Mizukami, T.M. Suzuki, Preparation and hydrogen permeation properties of thin Pd-Au alloy membranes supported on porous alpha-alumina tube, *Materials Transactions* 49(3) (2008) 449-452.
- [48] S.I. Pyun, W.J. Lee, T.H. Yang, Hydrogen diffusion through palladium-gold alloy coatings electrodeposited on palladium substrate under permeable boundary condition, *Thin Solid Films* 311(1-2) (1997) 183-189.
- [49] S. Uemiya, T. Endo, R. Yoshiie, W. Katoh, T. Kojima, Fabrication of thin palladium-silver alloy film by using electroplating technique, *Materials Transactions* 48(5) (2007) 1119-1123.
- [50] H.D. Tong, A. Berg, J.G.E. Gardeniers, H.V. Jansen, F.C. Gielens, M.C. Elwenspoek, Preparation of palladium-silver alloy films by a dual-sputtering technique and its application in hydrogen separation membrane, *Thin Solid Films* 479(1-2) (2005) 89-94.
- [51] L.S. McLeod, F.L. Degertekin, A.G. Fedorova, Effect of microstructure on hydrogen permeation through thermally stable, sputtered palladium-silver alloy membranes, *Applied Physics Letters* 90(26) (2007).
- [52] M. Katoh, A. Sondoh, T. Horikawa, T. Tomida, Characterization of palladium and palladium-silver alloy layers on stainless steel support, *International Journal Of Modern Physics B* 20(25-27) (2006) 3866-3871.
- [53] D.A.P. Tanaka, M.A.L. Tanco, S. Niwa, Y. Wakui, F. Mizukami, T. Namba, T.M. Suzuki, Preparation of palladium and silver alloy membrane on a porous alpha-alumina tube via simultaneous electroless plating, *Journal Of Membrane Science* 247(1-2) (2005) 21-27.
- [54] H.D. Tong, F.C. Gielens, J.G.E. Gardeniers, H.V. Jansen, J.W. Berenschot, M.J. de Boer, J.H. de Boer, C.J.M. van Rijn, M.C. Elwenspoek, Microsieve supporting palladium-silver alloy membrane and application to hydrogen separation, *Journal Of Microelectromechanical Systems* 14(1) (2005) 113-124.

- [55] A.L. Lvov, Malyshev.La, Petrovsk.Oi, HYDROGEN DIFFUSION THROUGH MEMBRANES FROM PALLADIUM AND ITS ALLOY WITH SILVER, *Zhurnal Fizicheskoi Khimii* 47(7) (1973) 1698-1701.
- [56] T.A. Peters, M. Stange, H. Klette, R. Bredesen, High pressure performance of thin Pd-23%Ag/stainless steel composite membranes in water gas shift gas mixtures; influence of dilution, mass transfer and surface effects on the hydrogen flux, *Journal of Membrane Science* 316(1-2) (2008) 119-127.
- [57] H.Y. Gao, Y.S. Lin, Y.D. Li, B.Q. Zhang, Chemical stability and its improvement of palladium-based metallic membranes, *Industrial & Engineering Chemistry Research* 43(22) (2004) 6920-6930.
- [58] S.K. Gade, E.A. Payzant, H.J. Park, P.M. Thoen, J.D. Way, The effects of fabrication and annealing on the structure and hydrogen permeation of Pd-Au binary alloy membranes, *Journal Of Membrane Science* 340(1-2) (2009) 227-233.
- [59] K. Zhang, X.T. Wei, Z.B. Rui, Y.D. Li, Y.S. Lin, Effect of Metal-Support Interface on Hydrogen Permeation through Palladium Membranes, *Aiche Journal* 55(3) (2009) 630-639.
- [60] K.S. Rothenberger, A.V. Cugini, B.H. Howard, R.P. Killmeyer, M.V. Ciocco, B.D. Morreale, R.M. Enick, F. Bustamante, I.P. Mardilovich, Y.H. Ma, High pressure hydrogen permeance of porous stainless steel coated with a thin palladium film via electroless plating, *Journal Of Membrane Science* 244(1-2) (2004) 55-68.
- [61] F. Guazzone, E.E. Engwall, Y.H. Ma, Effects of surface activity, defects and mass transfer on hydrogen permeance and n-value in composite palladium-porous stainless steel membranes, *Catalysis Today* 118(1-2) (2006) 24-31.
- [62] S.N. Paglieri, J.D. Way, Innovations in palladium membrane research, *Separation and Purification Methods* 31(1) (2002) 1-169.
- [63] S. Uemiya, State-of-the-art of supported metal membranes for gas separation, *Separation and Purification Methods* 28(1) (1999) 51-85.
- [64] D.J. Edlund, J. McCarthy, The Relationship Between Intermetallic Diffusion and Flux Decline in Ccomposite-Metal Membranes - Implications for Achieving Long Membrane Lifetime, *Journal of Membrane Science* 107(1-2) (1995) 147-153.
- [65] F.J. Kong, J.G. Du, G. Jiang, The structure and potential energy function of PdCO molecule, *Acta Physica Sinica* 57(1) (2008) 149-154.

- [66] N. Ozawa, N.B. Arboleda, H. Nakanishi, H. Kasai, First principles study of hydrogen atom adsorption and diffusion on Pd₃Ag(111) surface and in its subsurface, *Surface Science* 602(4) (2008) 859-863.
- [67] L. Semidey-Flecha, D.S. Sholl, Combining density functional theory and cluster expansion methods to predict H₂ permeance through Pd-based binary alloy membranes, *Journal of Chemical Physics* 128(14) (2008).
- [68] M.P. Hyman, B.T. Loveless, J.W. Medlin, A density functional theory study of H₂S decomposition on the (111) surfaces of model Pd-alloys, *Surface Science* 601(23) (2007) 5382-5393.
- [69] C.G. Sonwane, J. Wilcox, Y.H. Ma, Achieving optimum hydrogen permeability in PdAg and PdAu alloys, *Journal Of Chemical Physics* 125(18) (2006).
- [70] C.G. Sonwane, J. Wilcox, Y.H. Ma, Solubility of hydrogen in PdAg and PdAu binary alloys using density functional theory, *Journal Of Physical Chemistry B* 110(48) (2006) 24549-24558.
- [71] D.R. Alfonso, A.V. Cugini, D.S. Sholl, Density functional theory studies of sulfur binding on Pd, Cu and Ag and their alloys, *Surface Science* 546(1) (2003) 12-26.
- [72] O.M. Lovvik, R.A. Olsen, Density functional calculations on hydrogen in palladium-silver alloys, 2002. pp. 332-337.
- [73] G.W. Watson, R.P.K. Wells, D.J. Willock, G.J. Hutchings, A comparison of the adsorption and diffusion of hydrogen on the {111} surfaces of Ni, Pd, and Pt from density functional theory calculations, *Journal of Physical Chemistry B* 105(21) (2001) 4889-4894.
- [74] G.W. Watson, R.P.K. Wells, D.J. Willock, G.J. Hutchings, Ab initio simulation of the interaction of hydrogen with the {111} surfaces of platinum, palladium and nickel. A possible explanation for their difference in hydrogenation activity, *Chemical Communications*(8) (2000) 705-706.
- [75] V. Pallassana, M. Neurock, L.B. Hansen, B. Hammer, J.K. Norskov, Theoretical analysis of hydrogen chemisorption on Pd(111), Re(0001) and Pd-ML/Re(0001), Re-ML/Pd(111) pseudomorphic overlayers, *Physical Review B* 60(8) (1999) 6146-6154.
- [76] E. Broclawik, Quantum chemical description of catalytic activation of the C-H bond, *Polish Journal of Chemistry* 72(7) (1998) 1551-1564.

- [77] V. Ledentu, W. Dong, P. Sautet, Ab initio study of the dissociative adsorption of H₂ on the Pd(110) surface, *Surface Science* 413 (1998) 518-526.
- [78] O.M. Lovvik, R.A. Olsen, Adsorption energies and ordered structures of hydrogen on Pd(111) from density-functional periodic calculations, *Physical Review B* 58(16) (1998) 10890-10898.
- [79] W. Dong, V. Ledentu, P. Saute, G. Kresse, J. Hafner, A theoretical study of the H-induced reconstructions of the Pd(110) surface, *Surface Science* 377(1-3) (1997) 56-61.
- [80] W. Dong, G. Kresse, J. Hafner, Dissociative adsorption of H₂ on the Pd(111) surface, *Journal Of Molecular Catalysis A-Chemical* 119(1-3) (1997) 69-76.
- [81] W. Dong, J. Hafner, H₂ dissociative adsorption on Pd(111), *Physical Review B* 56(23) (1997) 15396-15403.
- [82] R.A. Olsen, G.J. Kroes, O.M. Lovvik, E.J. Baerends, The influence of surface motion on the direct subsurface absorption of H₂ on Pd(111), *Journal of Chemical Physics* 107(24) (1997) 10652-10661.
- [83] W.Q. Liang, R. Hughes, The effect of diffusion direction on the permeation rate of hydrogen in palladium composite membranes, *Chemical Engineering Journal* 112(1-3) (2005) 81-86.
- [84] I.P. Mardilovich, E. Engwall, Y.H. Ma, Dependence of hydrogen flux on the pore size and plating surface topology of asymmetric Pd-porous stainless steel membranes, *Desalination* 144(1-3) (2002) 85-89.
- [85] H. Amandusson, L.G. Ekedahl, H. Dannelun, Hydrogen permeation through surface modified Pd and PdAg membranes, *Journal Of Membrane Science* 193(1) (2001) 35-47.
- [86] K. Hou, R. Hughes, The effect of external mass transfer, competitive adsorption and coking on hydrogen permeation through thin Pd/Ag membranes, *Journal of Membrane Science* 206(1-2) (2002) 119-130.
- [87] A. Unemoto, A. Kaimai, K. Sato, T. Otake, K. Yashiro, J. Mizusaki, T. Kawada, T. Tsuneki, Y. Shirasaki, I. Yasuda, The effect of co-existing gases from the process of steam reforming reaction on hydrogen permeability of palladium alloy membrane at high temperatures, *International Journal of Hydrogen Energy* 32(14) (2007) 2881-2887.

- [88] A. Li, W. Liang, R. Hughes, The effect of carbon monoxide and steam on the hydrogen permeability of a Pd/stainless steel membrane, *Journal of Membrane Science* 165(1) (2000) 135-141.
- [89] D. Wang, T.B. Flanagan, K.L. Shanahan, Hydrogen permeation measurements of partially internally oxidized Pd-Al alloys in the presence and absence of CO, *Annu. Rev. Mater. Sci.* 253(1-2) (2005) 165-173.
- [90] G. Barbieri, F. Scura, F. Lentini, G. De Luca, E. Drioli, A novel model equation for the permeation of hydrogen in mixture with carbon monoxide through Pd-Ag membranes, *Separation and Purification Technology* 61(2) (2008) 217-224.
- [91] T.B. Flanagan, D. Wang, S. Luo, Thermodynamics of H in disordered Pd-Ag alloys from calorimetric and equilibrium pressure-composition-temperature measurements, *Journal Of Physical Chemistry B* 111(36) (2007) 10723-10735.
- [92] D. Wang, T.B. Flanagan, K. Shanahan, Diffusion of H through Pd-Ag alloys (423-523 K), *Journal of Physical Chemistry B* 112(4) (2008) 1135-1148.
- [93] G.F. Zeng, A. Goldbach, H.Y. Xu, Impact of support mass flow resistance on low-temperature H₂ permeation characteristics of a Pd₉₅Ag₅/Al₂O₃ composite membrane, *Journal of Membrane Science* 326(2) (2009) 681-687.
- [94] H. Li, H.Y. Xu, W.Z. Li, Study of n value and alpha/beta palladium hydride phase transition within the ultra-thin palladium composite membrane, *Journal of Membrane Science* 324(1-2) (2008) 44-49.
- [95] M.E. Ayturk, E.E. Engwall, Y.H. Ma, Microstructure analysis of the intermetallic diffusion-induced alloy phases in composite Pd/Ag/porous stainless steel membranes, *Industrial & Engineering Chemistry Research* 46(12) (2007) 4295-4306.
- [96] A. Li, J.R. Grace, C.J. Lim, Preparation of thin Pd-based composite membrane on planar metallic substrate - Part 1: Pre-treatment of porous stainless steel substrate, *Journal Of Membrane Science* 298(1-2) (2007) 175-181.
- [97] W. Liu, B.Q. Zhang, X.F. Liu, Progress in palladium composite membranes, *Progress in Chemistry* 18(11) (2006) 1468-1481.
- [98] D. Yepes, L.M. Cornaglia, S. Irusta, E.A. Lombardo, Different oxides used as diffusion barriers in composite hydrogen permeable membranes, *Journal of Membrane Science* 274(1-2) (2006) 92-101.

- [99] Y. Zhang, R. Maeda, M. Komaki, C. Nishimura, Hydrogen permeation and diffusion of metallic composite membranes, *Journal Of Membrane Science* 269(1-2) (2006) 60-65.
- [100] Y.H. Ma, B.C. Akis, M.E. Ayturk, F. Guazzone, E.E. Engwall, I.P. Mardilovich, Characterization of intermetallic diffusion barrier and alloy formation for Pd/Cu and Pd/Ag porous stainless steel composite membranes, *Industrial & Engineering Chemistry Research* 43(12) (2004) 2936-2945.
- [101] Y.H. Ma, I.P. Mardilovich, E.E. Engwall, Thin composite palladium and palladium/alloy membranes for hydrogen separation, *Advanced Membrane Technology*, 2003. pp. 346-360.
- [102] A. Caravella, G. Barbieri, E. Drioli, Modelling and simulation of hydrogen permeation through supported Pd-alloy membranes with a multicomponent approach, *Chemical Engineering Science* 63(8) (2008) 2149-2160.
- [103] F.C. Gielens, H.D. Tong, M.A.G. Vorstman, J.T.F. Keurentjes, Measurement and modeling of hydrogen transport through high-flux Pd membranes, *Journal Of Membrane Science* 289(1-2) (2007) 15-25.
- [104] D.G. Goodwin, An Open-Source, Extensible Software Suite for CVD; Process Simulation, Chemical Vapor Deposition, in: M. Allendorf, F. Maury, F. Teyssandier (Eds.), 16th EUROCVT, The Electrochemical Society, 2003. pp. 155-162.
- [105] D.G. Goodwin, An Open-Source, Extensible Software Suite for CVD; Process Simulation, Chemical Vapor Deposition, in: M. Allendorf, F. Maury, F. Teyssandier (Eds.), 16th EUROCVT, The Electrochemical Society, 2003. pp. 155-162.
- [106] S.A. Seyed-Reihani, G.S. Jackson, Effectiveness in catalytic washcoats with multi-step mechanisms for catalytic combustion of hydrogen, *Chemical Engineering Science* 59(24) (2004) 5937-5948.
- [107] D. Wang, T.B. Flanagan, K.L. Shanahan, Permeation of hydrogen through pre-oxidized Pd membranes in the presence and absence of CO, *Journal of Alloys and Compounds* 372(1-2) (2004) 158-164.
- [108] T.B. Flanagan, D. Wang, K.L. Shanahan, The role of non-ideality in H permeation through membranes, *Scripta Materialia* 56(4) (2007) 261-263.

- [109] S. Hara, M. Ishitsuka, H. Suda, M. Mukaida, K. Haraya, Pressure-Dependent Hydrogen Permeability Extended for Metal Membranes Not Obeying the Square-Root Law, *Journal of Physical Chemistry B* 113(29) (2009) 9795-9801.
- [110] F.C. Gielens, R.J.J. Knibbeler, P.F.J. Duysinx, H.D. Tong, M.A.G. Vorstman, J.T.F. Keurentjes, Influence of steam and carbon dioxide on the hydrogen flux through thin Pd/Ag and Pd membranes, *Journal Of Membrane Science* 279(1-2) (2006) 176-185.
- [111] T.B. Flanagan, D. Wang, K.L. Shanahan, Diffusion of H through Pd membranes: Effects of non-ideality, *Journal of Membrane Science* 306(1-2) (2007) 66-74.
- [112] O.M. Lovvik, R.A. Olsen, Density functional calculations of hydrogen adsorption on palladium-silver alloy surfaces, *Journal of Chemical Physics* 118(7) (2003) 3268-3276.
- [113] H.H. Kart, M. Tomak, M. Uludogan, T. Cagin, Thermodynamical and mechanical properties of Pd-Ag alloys, *Computational Materials Science* 32(1) (2005) 107-117.
- [114] I.J. Iwuchukwu, A. Sheth, Mathematical modeling of high temperature and high-pressure dense membrane separation of hydrogen from gasification, *Chemical Engineering and Processing* 47(8) (2008) 1298-1310.
- [115] A. Bhargav, G.S. Jackson, Thermokinetic modeling and parameter estimation for hydrogen permeation through Pd_{0.77}Ag_{0.23} membranes, *International Journal of Hydrogen Energy* 34(12) (2009) 5164-5173.
- [116] S.C. DeCaluwe, H. Zhu, R.J. Kee, G.S. Jackson, Importance of anode microstructure in modeling solid oxide fuel cells, *Journal of the Electrochemical Society* 155(6) (2008) B538-B546.
- [117] H.Y. Zhu, R.J. Kee, V.M. Janardhanan, O. Deutschmann, D.G. Goodwin, Modeling elementary heterogeneous chemistry and electrochemistry in solid-oxide fuel cells, *Journal of the Electrochemical Society* 152(12) (2005) A2427-A2440.
- [118] J. Vanbrakel, S. Modry, M. Svata, MERCURY POROSIMETRY - STATE OF THE ART, *Powder Technology* 29(1) (1981) 1-12.
- [119] B.D. Morreale, M.V. Ciocco, B.H. Howard, R.P. Killmeyer, A. Cugini, R.M. Enick, Effect of hydrogen-sulfide on the hydrogen permeance of palladium-copper

alloys at elevated temperatures, *Journal Of Membrane Science* 241(2) (2004) 219-224.

[120] O. Iyoha, B. Howard, B. Morreale, R. Killmeyer, R. Enick, The effects of H₂O, CO and CO₂ on the H-2 permeance and surface characteristics of 1 mm thick Pd₈₀wt%Cu membranes, *Topics in Catalysis* 49(1-2) (2008) 97-107.

[121] S.A.S. Reihani, G.S. Jackson, Mechanism analysis with ILDMs for H-2 combustion on Pd catalysts, *Combustion Theory And Modelling* 10(1) (2006) 1-20.

[122] S.-A. Seyed-Reihani, Evaluating surface mechanisms for H₂ and CH₄ combustion on Pd catalysts, Mechanical Engineering, University of Maryland, College Park, 2005.

[123] H. Li, A. Goldbach, W.Z. Li, H.Y. Xu, CO₂ decomposition over Pd membrane surfaces, *Journal of Physical Chemistry B* 112(39) (2008) 12182-12184.

[124] J. Hoffmann, I. Meusel, J. Hartmann, J. Libuda, H.J. Freund, Reaction kinetics on heterogeneous model catalysts - The CO oxidation on alumina-supported Pd particles, *Journal of Catalysis* 204(2) (2001) 378-392.

[125] V. Bondzie, P. Kleban, D.A. Browne, MECHANISM FOR CO OXIDATION AND OSCILLATORY REACTIONS ON Pd(110), *Journal of Vacuum Science & Technology a-Vacuum Surfaces and Films* 11(4) (1993) 1946-1950.

[126] R. Imbihl, G. Ertl, OSCILLATORY KINETICS IN HETEROGENEOUS CATALYSIS, *Chemical Reviews* 95(3) (1995) 697-733.

[127] B. Brandt, T. Schalow, M. Laurin, S. Schauermann, J. Libuda, H.J. Freund, Oxidation, reduction, and reactivity of supported Pd nanoparticles: Mechanism and microkinetics, *Journal of Physical Chemistry C* 111(2) (2007) 938-949.

[128] D.J. Liu, Lattice-gas modeling of CO adlayers on Pd(100), *Journal of Chemical Physics* 121(9) (2004) 4352-4357.

[129] D.R. Alfonso, Comparative studies of CO and H₂O interactions with Pd(111) surface: A theoretical study of poisoning, *Applied Physics Letters* 88(5) (2006).

[130] J.F. Kramer, S.A.S. Reihani, G.S. Jackson, Low-temperature combustion of hydrogen on supported Pd catalysts, *Proceedings of the Combustion Institute* 29 (2003) 989-996.

- [131] M.A. Henderson, The interaction of water with solid surfaces: fundamental aspects revisited, *Surface Science Reports* 46(1-8) (2002) 5-308.
- [132] U.M. Ascher, L.R. Petzold, *Computer methods for ordinary differential equations and differential algebraic equations*, Society for Industrial and Applied Mathematics (SIAM), 1998.
- [133] W. Gibbons, A. Bhargav, I.R. Young, G.S. Jackson, Preliminary H₂O poisoning studies on Pd composite membranes: experiments conducted at the Fuel Cell Research Laboratory at the University of Maryland., 2010.
- [134] A. Bhargav, G.S. Jackson, R.J. Ciora, P. Liu, Model Development and Validation of Hydrogen Transport through Supported Palladium Membranes, accepted for publication in the *Journal of Membrane Science* (2010).